การประมวลผลภาพสำหรับการตรวจวัดทางธรณีเทคนิคในห้องปฏิบัติการ

นางสาวเอริกา อลิส ซาโลมา อุย

วิทยานิพนธ์นี้เป็นส่วนหนึ่งของการศึกษาตามหลักสูตรปริญญาวิศวกรรมศาสตรมหาบัณฑิต
สาขาวิชาวิศวกรรมโยธา ภาควิชาวิศวกรรมโยธา
คณะวิศวกรรมศาสตร์ จุฬาลงกรณ์มหาวิทยาลัย
ปีการศึกษา 2556

IMAGE PROCESSING FOR LABORATORY GEOTECHNICAL MEASUREMENTS

Miss Erica Elice Saloma Uy

A Thesis Submitted in Partial Fulfillment of the Requirements
for the Degree of Master of Engineering Program in Civil Engineering
Department of Civil Engineering
Faculty of Engineering
Chulalongkorn University
Academic Year 2013

Thesis Title	IMAGE PROCESSING FOR LABORATORY GEOTECHNICAL MEASUREMENTS
By	Miss Erica Elice Saloma Uy
Field of Study	Civil Engineering
Thesis Advisor	Associate Professor Tirawat Boonyatee, D.Eng.

Accepted by the Faculty of Engineering, Chulalongkorn University in Partial Fulfillment of the Requirements for the Master's Degree

.....Dean of the Faculty of Engineering

(Professor Bundhit Eua-arporn, Ph.D.)

THESIS COMMITTEE

.....Chairman

(Associate Professor Boonchai Ukritchon, Sc.D.)

.....Thesis Advisor

(Associate Professor Tirawat Boonyatee, D.Eng.)

.....External Examiner

(Assistant Professor Warat Kongkitkul, Ph.D.)

เอริกา อลิส ซาโลมา อุย : การประมวลผลภาพสำหรับการตรวจวัดทางธรณีเทคนิคในห้องปฏิบัติการ. (IMAGE PROCESSING FOR LABORATORY GEOTECHNICAL MEASUREMENTS) อ.ที่ปรึกษาวิทยานิพนธ์หลัก: รศ. ฐิรวัตร บุญญะฐี, 147 หน้า.

การวิจัยนี้เป็นการประยุกต์ใช้เทคนิคการประมวลผลภาพเพื่อตรวจวัดการเคลื่อนตัวของดินแบบไม่สัมผัส ผู้วิจัยได้ใช้ภาษา Labview เขียนโปรแกรมคอมพิวเตอร์สำหรับตรวจวัดการเคลื่อนตัวของแท่งตัวอย่างในเครื่องทดสอบสามแกนทั้งแบบสองมิติและสามมิติ สำหรับโปรแกรมสำหรับการตรวจวัดการเคลื่อนที่แบบสองมิตินั้นใช้การวิเคราะห์ภาพถ่ายจากกล้องถ่ายรูปสองตัวที่ติดตั้งให้หันขนานไปในทางเดียวกัน โดยได้มีการปรับแก้การบิดเบี้ยวของภาพถ่ายจากการสอบเทียบด้วย สำหรับการเคลื่อนที่นั้นได้คำนวณจากการเปรียบเทียบตำแหน่ง ณ เวลาต่างๆ ของจุดที่สนใจซึ่งทำได้โดยใช้ขั้นตอนวิธีการไหลเชิงแสงแบบพีรามิดซึ่งถูกเสนอโดย Lucas and Kanade (1981) ผลการคำนวณที่ได้ถูกนำไปเปรียบเทียบกับผลตรวจวัดโดยใช้เซนเซอร์วัดการเคลื่อนที่เชิงเส้นซึ่งพบว่ามีความสอดคล้องกันดี

สำหรับการตรวจวัดการเคลื่อนที่แบบสามมิตินั้นได้ใช้ขั้นตอนวิธีแบบสามมิติซึ่งประกอบด้วยการสอบเทียบ การปรับตรง การหาความสมนัย และการฉายกลับ ในการปรับแต่งภาพก่อนที่จะใช้ขั้นตอนวิธีเดียวกันกับการตรวจวัดแบบสองมิติในการหาการเคลื่อนที่ต่อไป ผลการคำนวณที่ได้ถูกนำไปเปรียบเทียบกับผลตรวจวัดการเคลื่อนที่และปริมาตรของน้ำที่ไหลออกจากแท่งตัวอย่างจำลองที่ทำด้วยฟองน้ำภายใต้การบีบอัดด้วยแรงกระทำแบบเท่ากันทุกทิศทางด้วยเครื่องทดสอบสามแกน ซึ่งพบว่ามีความสอดคล้องกันดี

หลังจากที่ได้พัฒนาและตรวจสอบความถูกต้องของโปรแกรมแล้ว ผู้วิจัยได้ทดลองตรวจวัดการเคลื่อนตัวของแท่งตัวอย่างดินจริงโดยการเฉือนแท่งตัวอย่างด้วยเครื่องทดสอบสามแกน ซึ่งพบว่าโปรแกรมที่ได้พัฒนาขึ้นสามารถตรวจวัดการเคลื่อนที่แบบสามมิติได้ โดยมีความเที่ยงตรงขั้นต่ำเท่ากับ 0.006 cm และมีความแม่นยำขั้นต่ำเท่ากับ 0.004 cm

เนื่องจากโปรแกรมที่พัฒนาขึ้นสามารถตรวจวัดการเคลื่อนตัวได้เฉพาะพื้นที่ที่กล้องถ่ายรูปสามารถมองเห็นได้เท่านั้น ระบบที่ได้พัฒนาขึ้นจึงยังมีข้อจำกัดจึงยังไม่สามารถคำนวณหาปริมาตรน้ำที่ไหลออกจากแท่งตัวอย่างได้ในกรณีที่เกิดการเสียรูปแบบไม่สมมาตร อย่างไรก็ตามข้อจำกัดดังกล่าวสามารถแก้ไขได้โดยง่ายในอนาคตด้วยการเพิ่มจำนวนกล้องถ่ายรูปให้ครอบคลุมมุมมองต่างๆ รอบแท่งตัวอย่างได้

ภาควิชา วิศวกรรมโยธา ลายมือชื่อนิสิต .....

สาขาวิชา วิศวกรรมโยธา ลายมือชื่อ อ.ที่ปรึกษาวิทยานิพนธ์หลัก .....

ปีการศึกษา 2556

5570531221 : MAJOR CIVIL ENGINEERING
KEYWORDS: IMAGE PROCESSING / OPTICAL FLOW

ERICA ELICE SALOMA UY: IMAGE PROCESSING FOR LABORATORY GEOTECHNICAL MEASUREMENTS. ADVISOR: ASSOC. PROF. TIRAWAT BOONYATEE, D.Eng., 147 pp.

This research is an effort to apply image processing techniques for the non-contact determination of soil movement. A programming language called Labview (Laboratory Virtual Instrumentation Engineering Workbench) was used to develop computer codes for measuring the displacement in 2D and 3D of specimens in a triaxial apparatus. The first program was developed for 2D measurement using two cameras that pointed in parallel to the specimens. In this stage, a calibration procedure was established for the correction of distort images. The pyramidal optical flow algorithm (Lucas and Kanade, 1981) was used to trace the positions of interest points, from which later derived displacements. The results were compared with the measurements obtained from LVDTs and were well agreed.

For the 3D measuring system, stereo vision processes consisted of stereo calibration, stereo rectification, stereo correspondence and 3D re-projection were performed before applying the optical flow algorithm. The 3D system was verified by an isotropic compression test of a cylindrical sponge in the triaxial apparatus. The estimated displacement and discharge of water were compared with the measured ones and were well agreed.

After programs had been developed and tested, a shearing test on a real soil was made by the triaxial apparatus. From the experiment it was found that the binocular stereo vision developed has a good potential in making measurements. The repeatability and the resolution of the developed system were in the order of 0.006 cm and 0.004 cm, respectively. Since the developed system could determine deformation from only the area where the cameras can view, the current hardware configuration was not allowed for determining the discharge of water from un-symmetrical deformation. However, the developed system can be extended readily by adding more cameras so that photos can be taken from the missing view directions.

Department: Civil Engineering Student's Signature .....

Field of Study: Civil Engineering Advisor's Signature .....

Academic Year: 2013

ACKNOWLEDGEMENTS

I would like to thank AUN/SEED-Net and JICA for their generosity in funding this research and giving me the opportunity to pursue graduate studies. Furthermore, I would like to thank and express my greatest gratitude to my family, friends and mentors who always gave me the unconditional support that I need in going through this journey. I am forever grateful to my adviser who helped me broaden my knowledge and skills in my field of specialization. More so, I am thankful to my seniors and juniors who helped me in developing my research. Lastly, I would like to thank God for giving me the courage, wisdom and humility to pursue higher studies.

CONTENTS

Page

Page

Page

LIST OF FIGURES

LIST OF TABLES

CHAPTER 1

1 Introduction

1.1 Statement of the Problem

Geotechnical measurements have provided the life and blood for advances in modern geotechnical engineering (Marr, 2000). Since the development of soil mechanics in 1930s, innovations have been made to achieve more precise, accurate and reliable measurements. Manual systems were upgraded to more efficient automatic systems. For instance, a position read manually from a theodolite is now determined instantly by the machine.

Over the years, several techniques in measuring the displacement of soil were developed. Full-field measurements, which can also be referred to as a non-contact measurement, began to flourish by providing better understanding compared to point-wise measurements. In contrast to conventional sensors such as linear variable differential transducers (LVDTs), deformation can be determined without any direct contact with the target of measurement (Viggiani & Hall, 2008).

Image processing is becoming a trend especially in the field of Geotechnical Engineering in determining measurements. The advent of digital image processing (DSP) resulted in powerful measuring techniques such as Digital photogrammetry, particle image velocimetry (PIV) and digital image correlation (DIC) (Xing, Wells, Yaping, & Shearer, 1997). Its great potential is supported by the advance in technologies and the reducing cost of production.

Image processing was recently incorporated in conventional triaxial tests for determining the displacement of soil. It can also be applied in assessing the stability, alignment and amount of settlement of structures, for instance, a case of the seven-story stone tower in Sinsedong Pagoda, Gyeongsangbuk-do, Korea (Han, Hong, & Kim, 2012).

This study is an effort to develop a system for determining the displacement of soil specimen in triaxial apparatus. Particular attention was paid for the displacement of soil in very small strain region. Non-contact measurement by the

image processing is more preferred in this region since non-local LVDT measurements are affected by seating problems and local LVDT techniques may disturbed the soil around the contact point.

1.2 Objectives and Outcome

The main objective of this study is to seek applications of image processing techniques to the measurement in geotechnical works. Specifically the study aims to:

1.2.1 Apply image processing for determining the movement of points in three dimensional space.

1.2.2 Apply image processing to determine the displacement in the specimen and the volume of water that circulate through the specimen in the triaxial apparatus.

1.2.3 Apply image processing for full-field measurement of the specimen in the triaxial apparatus.

1.3 Scope and Limitations

The study's main concern is to apply image processing in geotechnical measurements but is limited by the following factors:

1.3.1 Geotechnical properties of the soil tested are not determined.

1.3.2 Stress path, loading rate, confining pressure and constitutive model are not considered.

1.3.3 Digital single-lens reflex (DSLR) cameras are used to take pictures.

1.3.4 The measurement of deformations can only be done at the area where the cameras can view.

1.4 Significance of the Study

The purpose of this study is to develop an accurate, non-contact, full-field measuring system. The result of this study will benefit both experimental and practical works. The develop system can serve as a tool for monitoring the stability of slope, assessing the orientation of structure, etc. It requires less cost and set-up

time than conventional wired, point-wise sensors for the comparable amount of information.

The develop system is also significant for experimental works because the full-field measurement will provide a better understanding of soil behaviors under testing. For instance, the early detection of local yielding zones and the propagation pattern of them can be attained.

Since the measurement is done under non-contact condition the disturbance introduced by the installation of sensors or their target points can be avoided.

1.5 Assumptions

1.5.1 The resolution of cameras is sufficient for the analysis.

1.5.2 The movement of soil specimens in the triaxial apparatus is similar to the movement of rubber membranes.

CHAPTER 2

2 Literature Review

2.1 Image Processing

Vision makes human perceive, understand and discover the world surrounding them. On the other hand, computer vision aims to replicate the human's vision by understanding the image through electronic devices (Sonka, Hlavac, & Boyle, 2008). Image acquisition and image processing are some techniques which makes this possible.

2.1.1 Image Acquisition and Image Processing

Image acquisition transforms the visual image of a physical object into a set of digitalized data. A pixel is the basic element or the building block of a digital image (Xing et al., 1997). It is a matrix of N x M value that describes a photograph as shown in Figure 2.1.1. Each pixel is assigned with a number or a set of numbers corresponding to either of three image types namely color, gray scale and binary images.

The color image is useful for object recognition. For color images, zero represents a clear pixel and 255 stands for a fully opaque pixel. The color of each pixel is described by a set of three numbers according to Red-Green-Blue (RGB) or Hue-Saturation-Luminance (HSL) models. The gray scale image is useful in identifying the intensity of light in an image. Each pixel in a gray scale image is represented by a number. The number zero is used for total darkness while higher values represent brighter intensity. For binary image, the value of each pixel can be either zero or one. The number zero value is considered to be black and one as white with no intermediate shades of color. It can provide the boundary value of black and white color. Thus, it is the reason why it is frequently applied in image processing even if it is not a colored image.

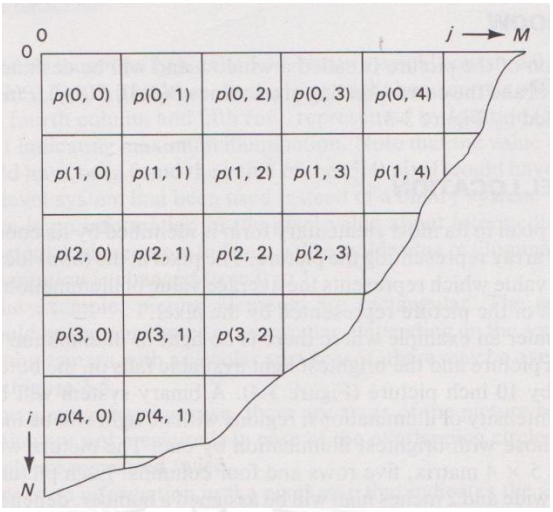

Figure 2.1.1 Pixel image matrix (Galbiati, 1990)

Image processing is the manipulation of images for some specific purposes such as image enhancement, image restoration or feature extraction, etc. The procedure of image processing involves thresholding process, histogram and line extraction, contour extraction and image noise removal (Han et al., 2012).

Thresholding is often an initial step in image processing which is used to identify the object of interest from the entire image. In this process, color or gray scale images are converted to binary image. Each pixel represents a range of intensities which will be useful for image processing. Histogram is used to show the contrast information of an image. It is represented in a bar chart were its abscissa represents the value of all possible pixels while the ordinate is the total image count. Line extraction describes object's features by showing characteristic lines in an image. Contour extraction is similar to line extraction but considers polygons instead of straight lines. Noise is the irregularities in brightness and pixel information of an image which should be removed to prevent some errors in further image processing steps. After analyses for its characteristic, the noise can be removed by filtering techniques.

Image processing can be grouped into five areas namely image enhancement, restoration, segmentation, object representation and description and image encoding. Each area has a particular role which is enumerated as follows (Johnson & Jennings, 2001):

a. Image enhancement adjusts the contrast and brightness.
b. Image restoration corrects blurs and geometric distortion.

c. Image segmentation divides an image into parts and extracts important features from the image.
d. Object representation and description describes the size, coordinates, shape factors and intensity distribution of objects in an image which were determined from image segmentation.
e. Image encoding reduces data to only amount needed by algorithms in the process.

2.1.2 Photographic Camera as a Measuring Instrument

A camera and lens are fundamental and necessary items for image processing. A digital camera uses some kind of opto-electric device to convert irradiated light into electrical charges and store them in an array of pixels, or, an image. For instance, the charged coupled device (CCD) is an opto-electric device invented by Boyle in 1970.

Cameras currently available in the market may be divided into two groups namely point and shoot cameras and single lens reflex (SLR) cameras. The point and shoot camera provides few options for adjusting photographing parameters such as the shutter speed, the aperture and focus. On the other hand, the SLR camera provides more controls over photographing parameters and also an option to change the lens. Therefore, the quality of images taken by the SLR camera tends to be superior to those taken by the point and shoot one.

Cameras are being used in image processing instead of video cameras due to their decreasing cost and increasing sophistication as well. In addition, some deteriorations such as line jitters and image noise can occur when an image is captured from a recorded video (White, Take, & Bolton, 2001). Cameras on the other hand, may experience image noise but of less magnitude than video cameras.

2.1.3 Distortion

2.1.3.1 Lens Distortion (Optical Aberrations)

Imperfections in manufacture and design of the lens can cause optical aberrations. A common optical aberration is lens distortion which shifts the location of pixels in the pixel array and results in the distorted image. It also affects the accuracy in obtaining the distance travelled, dimension and shape of an object.

Two common lens distortions are barrel distortion and pin cushion distortion (Neale, Hessel, & Terpstra, 2011). The barrel distortion causes the image to expand in a barrel like shape from the center (Figure 2.1.2.a). Straight lines appear bent in the distort image. The barrel distortion is normally associated with wide angle lenses which have short focal lengths. As illustrated in Figure 2.1.2.b, the pin cushion distortion causes the image to be pinched toward the center. The bent of a straight line is in opposite direction to the barrel distortion. The pin cushion distortion is normally associated with telephoto lenses which have long focal lengths.

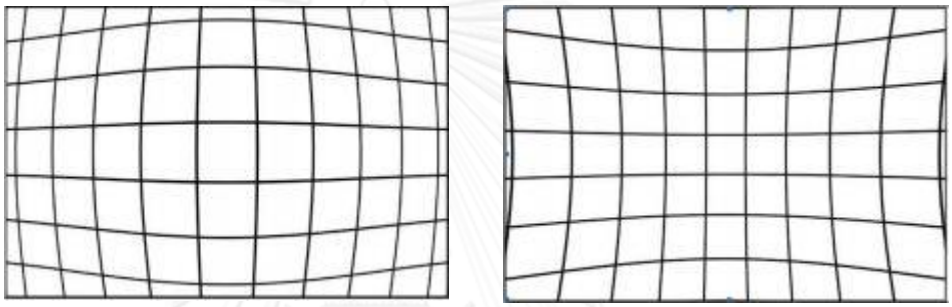

a) b)

Figure 2.1.2 a) Barrel distortion and b) Pin-cushion distortion (Neale et al., 2011)

2.1.3.2 Geometric Distortion

Besides lens distortion, geometric distortion can also affect the accuracy of measurements by the image processing. Two main geometric distortions are perspective distortion and refraction distortion. Perspective distortion is the improper scaling of nearby and distant features in an image. For extension prospective distortion, close objects appear disproportionally large while distant objects appear abnormally small. The reverse occurs for the compression perspective distortion.

Refraction distortion occurs when an image is taken through transparent objects, for instance, the plexiglass chamber of the triaxial apparatus. The degree of distortion depends on the thickness and refractive index of the transparent medium.

2.1.3.3 Camera Model and Calibration to Eliminate Distortion

A camera model is used to define the geometry of a camera and its lens. Accurate calibration of the camera model is crucial for quantitative measurement. The calibration process involves with the adjustment of internal and external parameters.

2.1.3.3.1 Camera Model

There are a number of models that describe the operation of the camera. Some of them are such as orthographic model, paraperspective projection model, perspective model, non-perspective projection model, etc. In this study, the pinhole camera model is used due to its simplicity. A pinhole camera is a sealed box with a tiny aperture, or the pinhole, on one side. The box blocks the rays of light except those passing through the pinhole, rendering the upside down image of the opposite side of the box.

The general geometry of the pinhole camera model is illustrated in Figure 2.1.3 b). On the contrary to the real camera, the model is working on a virtual image plane between the pinhole and objects seen by the camera. The pinhole camera model is composed of a camera coordinate system (F), optical center (C), principal point (c), image or retinal plane (R), effective focal length (f), optical axis, point of interest ($M = [X, Y, Z]^T$) and corresponding 2D projected point ($m = [x, y, z]^T$). The camera coordinate system is a three-dimensional orthonormal system of coordinates which is centered at C. It is denoted as $F = (C, X_C, Y_C, Z_C)$. It's X_C and Y_C axes are parallel to the image plane's axis. On the other hand, the Z_C axis is parallel to the optical axis. For the retinal plane, it is a two-dimensional orthonormal system. It can be represented as $R = (c, x_c, y_c)$. From this model, the point m can be related to point M from the following projection equations.

$$x_c = f * X_C/Z_C \quad (1)$$

$$y_c = f * Y_C/Z_C \quad (2)$$

where

x_c, y_c = coordinates of point m with respect to the virtual image plane

X_C, Y_C, Z_C = coordinates of point M with respect to the camera coordinate system

f = effective focal length

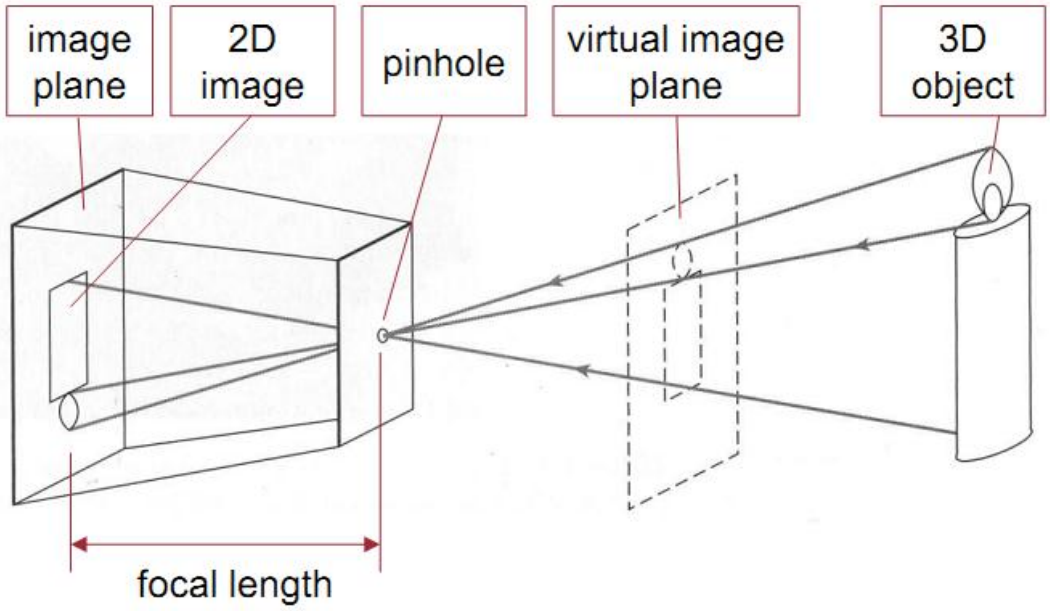

a) The pinhole camera model

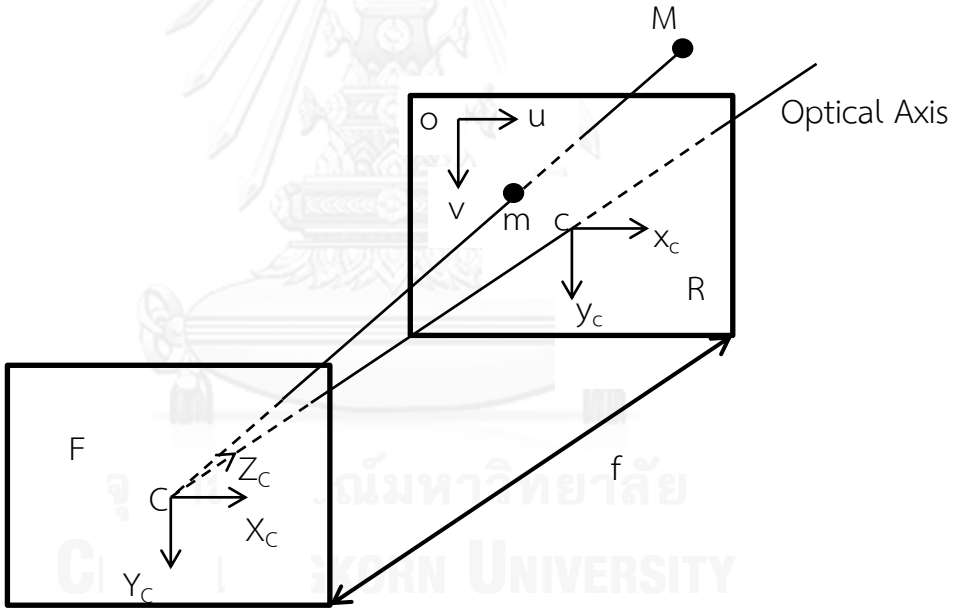

b) Relationship among model parameters on the virtual image plane

Figure 2.1.3 The general pinhole camera model (Kheng, 2012) (Faugeras & Luong, 2001)

Equation 1 and 2 are not convenient for most of image processing algorithms because of their nonlinear form. Therefore, the homogenous coordinate system is used for the point in the virtual image plane instead of the original coordinate system. With this adaptation, the point m can be related to point M from the following projection equations;

$$\begin{bmatrix} Z_C x_c \\ Z_C y_c \\ Z_C \end{bmatrix} = P_c \begin{bmatrix} X_C \\ Y_C \\ Z_C \\ 1 \end{bmatrix} \quad (3)$$

where

P_c = perspective projection matrix

$$P_c = \begin{bmatrix} f & 0 & 0 & 0 \\ 0 & f & 0 & 0 \\ 0 & 0 & 1 & 0 \end{bmatrix}$$

$Z_C x_c$, $Z_C x_c$, Z_C = homogenous coordinates of m with respect to the virtual image plane

X_C , Y_C, Z_C = coordinates of M with respect to the camera coordinate system

2.1.3.3.2 Intrinsic Parameters

Internal or intrinsic parameters of a camera are used to determine the coordinate in the image plane of a point considered. The intrinsic parameters are normally presented by the camera matrix, M as shown in Equation 4.

$$M = \begin{bmatrix} f_x & 0 & c_x \\ 0 & f_y & c_y \\ 0 & 0 & 1 \end{bmatrix} \quad (4)$$

where

$f_x = \frac{f}{s_x}$ = derivative focal length in x direction

$f_y = \frac{f}{s_y}$ = derivative focal length in y direction

s_x = horizontal size of a pixel in the camera sensor, in pixels per millimeter

s_y = vertical size of a pixel in the camera sensor, in pixels per millimeter

f = focal length or the distance between the principal point (u_o, v_o) and the optical center

c_x = horizontal distance from the principal point to the optical center on the image plane

c_y = vertical distance from the principal point to the optical center on the image plane

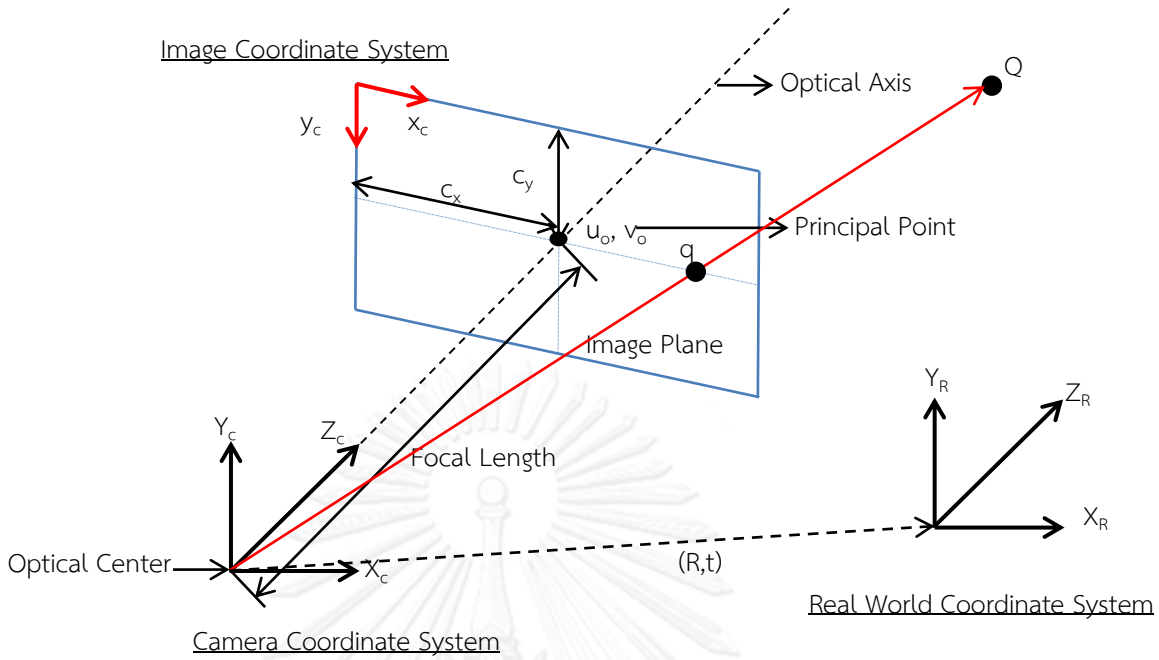

Figure 2.1.4 Illustration of the camera parameters (Frank, Stachniss, Grisetti, Arras, & Burgard, 2009)

The point q on the image plane in Figure 2.1.4 relates to the point Q by:

$$q = \begin{bmatrix} x \\ y \\ w \end{bmatrix}; Q = \begin{bmatrix} X \\ Y \\ Z \end{bmatrix}$$

$$q = MQ \tag{5}$$

where

M = camera matrix

For the distortion coefficients, there are two common types namely radial (k_1, k_2, k_3) and tangential distortion (p_1, p_2) coefficients. The radial distortion comes from the shape of the lens while the tangential distortion is due to the assembly process of the camera as a whole (Bradski & Kaehler, 2008). The coefficients are defined by a polynomial model and it is represented in the following equations:

$$x_{corrected} = x(1 + k_1 r^2 + k_2 r^4 + k_3 r^6) \tag{6}$$

$$y_{corrected} = y(1 + k_1 r^2 + k_2 r^4 + k_3 r^6) \tag{7}$$

$$x_{corrected} = x + [2p_1 xy + p_2(r^2 + 2x^2)] \tag{8}$$

$$y_{corrected} = y + [2p_2 xy + p_1(r^2 + 2y^2)] \tag{9}$$

where
(x, y) = coordinates on the image plane that corresponds to the point (X, Y, Z,) with respect to the world coordinate system
r = radial distance from the principal point of the image plane
$r = \sqrt{x^2 + y^2}$

2.1.3.3.3 Extrinsic Parameters

External or Extrinsic parameters characterizes the location and orientation of a camera with respect to the world frame. These parameters are essential since it estimates the geometrical relation between the camera and the object of concern. The external parameters are defined by two parameters; the rotation matrix and translation vector.

The general process of a two dimensional rotation as a matrix multiplication is shown in Equation 10 and in Figure 2.1.5. When three axes of rotation are considered, the rotation matrix (R) is modified into a product of three matrix multiplication having ψ, φ, and θ as the rotation angles of x, y and z axis respectively. Thus the rotation matrix can be written as R=$[R_z(\theta)]\,[R_y(\varphi)]\,[R_x(\psi)]$.

The translation vector is a parameter that represents the shift or offset of the first coordinate system to the second coordinate system (Bradski & Kaehler, 2008). For an object centered at a certain coordinate system it can be shifted to the camera coordinate system by applying the translation vector as shown in Equation 14.

$$\begin{bmatrix} x' \\ y' \end{bmatrix} = \begin{bmatrix} \cos\theta & \sin\theta \\ -\sin\theta & \cos\theta \end{bmatrix} \begin{bmatrix} x \\ y \end{bmatrix} = [R] \begin{bmatrix} x \\ y \end{bmatrix} \quad (10)$$

$$R_x(\psi) = \begin{bmatrix} 1 & 0 & 0 \\ 0 & \cos\psi & \sin\psi \\ 0 & -\sin\psi & \cos\psi \end{bmatrix} \quad (11)$$

$$R_y(\varphi) = \begin{bmatrix} \cos\varphi & 0 & -\sin\varphi \\ 0 & 1 & 0 \\ \sin\varphi & 0 & \cos\varphi \end{bmatrix} \quad (12)$$

$$R_z(\theta) = \begin{bmatrix} \cos\theta & \sin\theta & 0 \\ -\sin\theta & \cos\theta & 0 \\ 0 & 0 & 1 \end{bmatrix} \quad (13)$$

$$\begin{bmatrix} x' \\ y' \end{bmatrix} = \begin{bmatrix} x \\ y \end{bmatrix} - T \quad (14)$$

T= $\text{origin}_{\text{object}} - \text{origin}_{\text{camera}}$

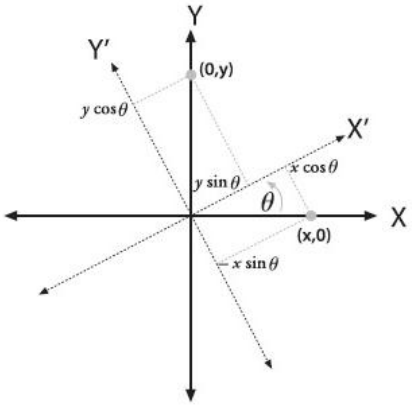

Figure 2.1.5 Representation of a two-dimensional rotation (Bradski & Kaehler, 2008)

2.1.3.3.4 Calibration Technique

Calibration can be divided into two stages namely, the camera modeling and the estimation of the parameters (Salvi, Armangue, & Batlle, 2002). The first stage is where the physical and optical behavior of the sensor was mathematically approximated. The second stage on the other hand deals with the application of direct or iterative methods in estimating the values of the internal and external parameters. Camera calibration is performed by allowing the camera to target an object that consists of distinct and identifiable points (Bradski & Kaehler, 2008). The target must be viewed in a variety of angles to determine the internal and external parameters of a camera as seen in Figure 2.1.7. The target can be a 3D object or a planar object such as a calibration panel. In order to extract the parameters of a camera, an analytical solution can be applied followed by a nonlinear optimization technique which is based on the maximum likelihood criterion (Zhang, 1998).

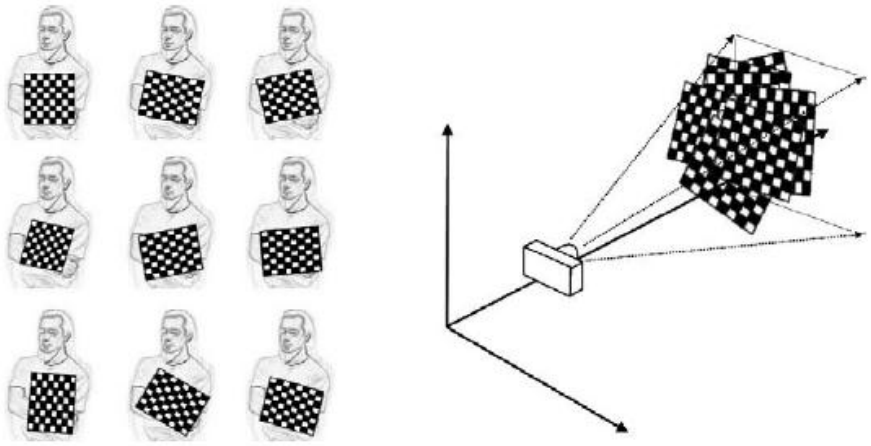

Figure 2.1.6 Illustration of calibrating a camera using a target (Bradski & Kaehler, 2008).

In order to perform the analytical method or the closed form solution a homography matrix (H) is needed. The homography matrix is used in the projective mapping from one plane to another (Bradski & Kaehler, 2008). It has two parts, the physical transformation and the projection. Physical transformation part is composed of the rotation matrix (R) and translation vector (t). Projection part is the camera matrix (M).

For instance, the point of interest, Q, can be mapped to its corresponding point, q. on the image plane by (Bradski & Kaehler, 2008):

$$q = HQ \tag{15}$$

$$\begin{bmatrix} x \\ y \\ 1 \end{bmatrix} = sM[r_1 \quad r_2 \quad r_3 \quad t] \begin{bmatrix} X \\ Y \\ Z \\ 1 \end{bmatrix}$$

where

$q = [x \quad y \quad 1]$

$H = sM[r_1 \quad r_2 \quad r_3 \quad t]$

$Q = [X \quad Y \quad Z \quad 1]$

s = arbitrary scale factor

In this study a planar calibration panel was used so Z = 0 and homography matrix (H) was modified to:

$$H = sM[r_1 \quad r_2 \quad t] \tag{16}$$

The homography matrix also serves as a constraint for determining the internal parameters. Rewriting Equation 16 to $\mathrm{H} = [\mathrm{h_1} \quad \mathrm{h_2} \quad \mathrm{h_3}]$, and changing the scale factor to an arbitrary scalar $\left(\frac{1}{\lambda}\right)$ we arrive at the following equation (Medioni & Kang, 2004):

$$\mathrm{H} = [\mathrm{h_1} \quad \mathrm{h_2} \quad \mathrm{h_3}] = \frac{1}{\lambda}\mathrm{M}[\mathrm{r_1} \quad \mathrm{r_2} \quad \mathrm{t}] \tag{17}$$

where

$\mathrm{s} = \frac{1}{\lambda}$

$\mathrm{h_1} = \mathrm{sMr_1}$ or $\mathrm{r_1} = \frac{1}{\mathrm{s}}\mathrm{M^{-1}h_1}$

$\mathrm{h_2} = \mathrm{sMr_2}$ or $\mathrm{r_2} = \frac{1}{\mathrm{s}}\mathrm{M^{-1}h_2}$

$\mathrm{h_3} = \mathrm{sMt}$ or $\mathrm{t} = \frac{1}{\mathrm{s}}\mathrm{M^{-1}h_3}$

Since the rotation vectors are orthogonal to each other, the dot product between them is equal to zero.

$$\mathrm{r_1^T r_2} = 0 \tag{18}$$

From $(\mathrm{ab})^{\mathrm{T}} = \mathrm{b^T a^T}$ and substituting $\mathrm{r_1} = \lambda\mathrm{M^{-1}h_1}$ and $\mathrm{r_2} = \lambda\mathrm{M^{-1}h_2}$, the first constraint equation can be obtained (Medioni & Kang, 2004).

$$(\mathrm{r_1 r_2})^{\mathrm{T}} = 0$$
$$\mathrm{h_1^T M^{-T} M^{-1} h_2} = 0 \tag{19}$$

The second constraint is obtained by equating the magnitudes of the rotation vectors. Rewriting Equation 20, the second constraint can be represented as Equation 21 (Medioni & Kang, 2004).

$$\|\mathrm{r_1}\| = \|\mathrm{r_2}\| \text{ or } \mathrm{r_1^T r_1} = \mathrm{r_2^T r_2} \tag{20}$$
$$\mathrm{h_1^T M^{-T} M^{-1} h_1} = \mathrm{h_2^T M^{-T} M^{-1} h_2} \tag{21}$$

These constraints will be used in the camera modeling stage were the closed-form solution is applied. The analytical method or the closed-form solution is presented in the following equations (Bradski & Kaehler, 2008):

Let

$$B = M^{-T}M^{-1} = \begin{bmatrix} B_{11} & B_{12} & B_{13} \\ B_{21} & B_{22} & B_{23} \\ B_{31} & B_{32} & B_{33} \end{bmatrix} \quad (22)$$

where

$$B = \begin{bmatrix} \frac{1}{f_x^2} & 0 & -\frac{c_x}{f_x^2} \\ 0 & \frac{1}{f_y^2} & -\frac{c_y}{f_y^2} \\ -\frac{c_x}{f_x^2} & -\frac{c_y}{f_y^2} & \frac{c_x^2}{f_x^2} + \frac{c_y^2}{f_y^2} + 1 \end{bmatrix}$$

When B matrix was applied to the two constraints, a general expression can be derived (Zhang, 1998),

$$h_i^T B h_j = v_{ij}^T b \quad (23)$$

where

$$b = [B_{11}, B_{12}, B_{22}, B_{13}, B_{23}, B_{33}]^T$$

$$v_{ij}^T = \left[h_{i1}h_{j1}, h_{i1}h_{j2} + h_{i2}h_{j1}, h_{i2}h_{j2}, h_{i3}h_{j1} + h_{i1}h_{j3}, h_{i3}h_{j2} + h_{i2}h_{j3}, h_{i3}h_{j3}\right]^T$$

Therefore, the two constraints presented previously can be written as 2 homogeneous equations (Zhang, 1998),

$$\begin{bmatrix} v_{12}^T \\ (v_{11} - v_{22})^T \end{bmatrix} b = 0 \text{ or } Vb = 0 \quad (24)$$

When n images of the target are taken, these images can be stacked together thus, arriving at Equation 24 where V is a 2nx6 matrix. When n $\geq$ 2 Equation 24 can be computed to estimate matrix b and from this the internal parameters can be obtained. Once the camera matrix and homography matrix is known the external parameters can be computed as well. Presented are the equations used to estimate the internal parameters (Xue, Wu, Zhu, & Ye, 2007):

$$\lambda = B_{33} - \frac{B_{13}^2 + v_0(B_{12}B_{13} - B_{11}B_{23})}{B_{11}} \quad (25)$$

$$f_x = \sqrt{\frac{\lambda}{B_{11}}} \quad (26)$$

$$f_y = \sqrt{\frac{\lambda B_{11}}{B_{11}B_{22} - B_{12}^2}} \quad (27)$$

$$c_x = -\frac{B_{13} f_x^2}{\lambda} \quad (28)$$

$$c_y = \frac{B_{12}B_{13} - B_{11}B_{23}}{B_{11}B_{22} - B_{12}^2} \quad (29)$$

The external camera parameters can be obtained from the following equations (Xue et al., 2007):

$$r_1 = \lambda M^{-1} h_1 \quad (30)$$

$$r_2 = \lambda M^{-1} h_2 \quad (31)$$

$$r_3 = r_1 x\, r_2 \quad (32)$$

$$t = \lambda M^{-1} h_3 \quad (33)$$

$$R = [r_1\ r_2\ r_3] \quad (34)$$

With the arbitrary scalar is computed as follows:

$$\lambda = \frac{1}{||M^{-1} h_1||} \quad (35)$$

The second stage of the calibration is where the maximum likelihood estimation is applied. This refines the data obtained from the first stage of the calibration. From the n images obtained, there will be m points within it. Assuming that the image points considered are corrupted by an independent and identically distributed noise, the maximum likelihood estimate can be obtained by minimizing (Zhang, 1998):

$$\sum_{i=1}^{n} \sum_{j=1}^{m} \left\| m_{ij} - \hat{m}(M, R_i, t_i, Q_j) \right\|^2 \quad (36)$$

where

$\hat{m}(M, R_i, t_i, Q_j)$ = projection of point Q_j

$R = [r_1\ r_2\ r_3]$

2.2 Optical Flow

2.2.1 Basic principle of Optical Flow

Optical flow can be defined as the changes through successive images of grayscale values (Fernando, Udawatta, & Pathirana, 2007). It has the dimensions of velocity and denoted as $\vec{v} = (u, v)$ where u and v is the x and y components of the

optical flow vector of a point. The algorithm works under an assumption that the brightness is constant among the images (Mahalingam et al., 2010). In other words, the object can move while the reflectivity and illumination stays constant. This can be represented in a mathematical expression as follows (O'Donovan, 2005):

$$f(x + \Delta x, y + \Delta y, t + \Delta t) \approx f(x, y, t) \quad (37)$$

where
$f(x, y, t)$ = intensity of the image at position (x, y) and at time t
$\Delta x, \Delta y, \Delta z$ = change in position
Δt = change in time

Optical flow algorithm can be divided into two approaches namely, gradient based approach and feature based approach.

2.2.1.1 Gradient Based Approach

The extraction of optical flow in this approach relies on the spatiotemporal variation of image brightness. The simple image intensity conservation equation is the basis of this approach which can be expressed by (Fernando et al., 2007)

$$I(x, y, t) = I(x + \delta x, y + \delta y, t + \delta t) \quad (38)$$

where
$\delta x, \delta y, \delta t$ = inter frame displacement and time interval respectively
Equation 38 can be rewritten in the first order differential equation as follows (Fernando et al., 2007):

$$\frac{\partial I}{\partial x}\frac{dx}{dt} + \frac{\partial I}{\partial y}\frac{dy}{dt} + \frac{\partial I}{\partial t} = 0 \quad (39)$$

where
$\frac{dx}{dt} = u$, $\frac{dy}{dt} = v$

Equation 39 approximates the velocity with respect to the direction of the spatial gradient. This method produces a dense optical flow field for a significant amount of pixels.

2.2.1.2 Feature Based Approach

Feature based approach establishes correspondence of feature points between the varying images at a certain time interval (Wedel & Cremers, 2011). Points having high intensity variation and gray level corners are matched to determine movements within the scene. For this approach the optical flow displacement for each pixel is obtained independently.

2.2.1.2.1 Lucas and Kanade Pyramidal Algorithm

Lucas and Kanade pyramidal optical flow algorithm is a feature based approach. It uses image patches together with windowing methods and incorporating least squares technique (Thota, Vemulapalli, Chintalapati, & Srinivas, 2013). It analyzes two grayscale images, I and J, having $\vec{x} = (x, y)$ as the pixel location within the image plane. Thus, $I(\vec{x}) = I(x, y)$ and $J(\vec{x}) = J(x, y)$. Let image $I(\vec{x})$ be the first image while image $J(\vec{x})$ be the second image. When a point of concern, $\vec{u} = (u_x, u_y)$, is established in the first image the algorithm will track its location $\vec{v} = \vec{u} + \vec{d}$ in the second image. $I(\vec{u})$ and $J(\vec{v})$ must be almost equal and have a similar brightness in the two dimensional neighborhood. Equation 40 is used to determine the displacement $\vec{d}$ which minimizes the residual function $\varepsilon(\vec{d})$ (Fernando et al., 2007).

$$\varepsilon(\vec{d}) = \varepsilon(d_x, d_y) = \sum_{x=u_x-\omega_x}^{u_x+\omega_x} \sum_{y=u_y-\omega_y}^{u_y+\omega_y} \left[I(x, y) - J(x + d_x, y + d_y)\right]^2 \quad (40)$$

where

ω_x, ω_y = arbitrary numbers that ranges from 1, 2, 3 or more pixels

The similarity of a point is searched through an integration window $(2\omega_x + 1)x(2\omega_y + 1)$. A small integration window is preferred since it does not smoothen out the important details contained within the image. A larger integration window can be used if a larger movement is being measured. The appropriate size for the integration window is determined by the pyramidal algorithm. Since the calculation is done in an iterative manner, it can be adapted to a required level of accuracy (Fernando et al., 2007).

The pyramidal algorithm is formulated by recursively computing a motion in I^1 from I_o image and then computes I^2 from I^1 and so on. The image I_o or the 0th level image is the raw image which has the highest resolution. Its image size is represented as $n_x^o = n_x$ and $n_y^o = n_y$ for its width and height respectively. The generic pyramid level is L (L = 0,1,2,...n) where n is the maximum number. In order to represent a pyramid level of an image I, it can be written as I^L where L denotes the level. The image size can also be rewritten as $n_x^L \, x \, n_y^L$ for this particular level. The pyramidal tracking works by computing the optical flow at the deepest pyramid level, L_n. Then the result in a form of an initial guess is transferred to the upper level, L_{n-1}. From this the result is transferred once again to the next level, L_{n-2}, until it reaches level 0 (Fernando et al., 2007). To track a point $\vec{u}$ in image I, Equation 40 will be used to determine the corresponding location $\vec{v} = \vec{u} + \vec{d}$ in image J. Point $\vec{u}$ on the pyramidal images I^L is defined as $\vec{u}^L = (u_x^L, u_y^L)$. Equation 41 will be used to compute its corresponding coordinates having a pyramid level of $L(L = (0,1,2, \dots, L_n)$.

$$\vec{u}^{L_{n-1}} = \frac{\vec{u}^{Ln}}{2^L} \tag{41}$$

2.3 Binocular Stereo Vision

2.3.1 Basic principle of Stereo Vision

The basic geometry of a stereo vision is presented in Figure 2.3.1. A frontal parallel arrangement is the simplest and the most ideal orientation for a binocular stereo vision. For this arrangement, it is assumed that the optical centers (O_l and O_r) are coincident with the x-axis of the left camera. The focal length (f), which is the distance between the principal point and the optical center, is maintained to be equal in the two cameras. The parameters c_{xleft} and c_{xright} are the principal points. It is the point of intersection between the image plane and optical axis. T or the baseline is the separation of the two cameras. As seen in Figure 2.3.1, x^l and x^r is the location of the object of concern with respect to the x-axis of each image planes. From this geometry the depth of a point P can be determined by (Saidon, Desa, Murugesa, & Rosbi, 2009):

$$Z = \frac{fT}{d} \tag{42}$$
$$d = x^l - x^r$$

where
d = disparity or the difference between the corresponding horizontal coordinate in each image plane (Saidon et al., 2009)

It can be observed from Equation 42 that the disparity is directly proportional to the focal length and baseline and inversely proportional to the depth. When the focal length and the baseline are kept constant the disparity value increases as the depth decreases as shown in Figure 2.3.2 (Scharstein, 1997).

A stereo vision system starts from the stereo calibration which eliminates distortion within images. It is followed by the stereo rectification to ensure that left and right images lie in the same plane. From this, stereo correspondence or matching between points is performed to obtain the disparity map. Then the re-projection for the depth values is done and followed by the reconstruction process. The processes presented will be discussed in depth in the succeeding sections.

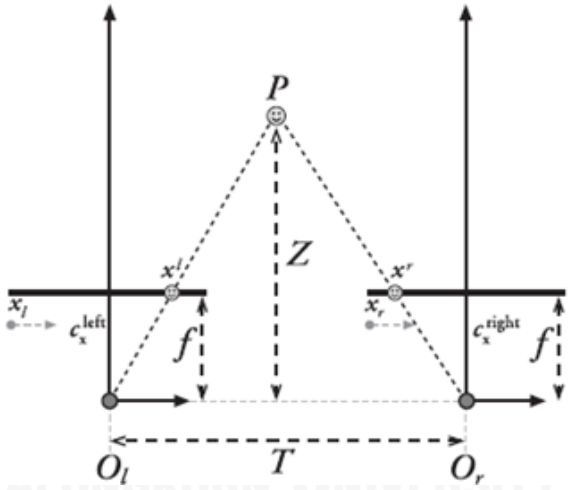

Figure 2.3.1 Typical configuration for a binocular stereo vision (Bradski & Kaehler, 2008)

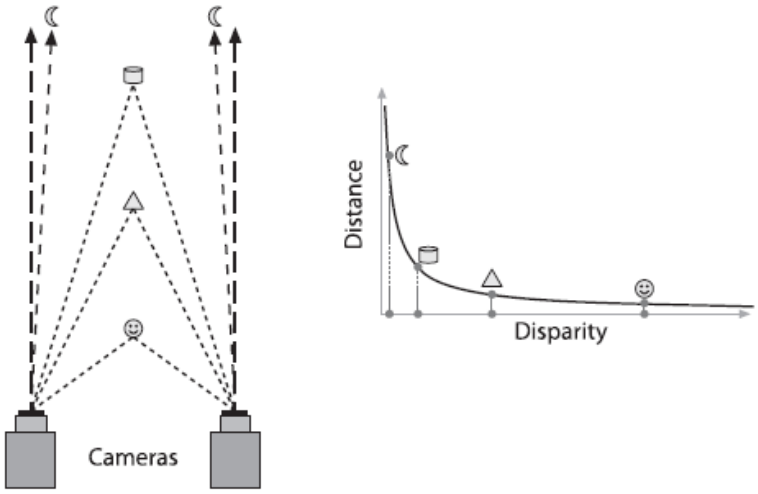

Figure 2.3.2 Relationship between disparity and depth (Bradski & Kaehler, 2008)

2.3.2 Stereo Calibration

In order for a stereo vision system to determine the 3D position of a point, there is a need to establish the relationship between coordinate systems of the two cameras. This relationship involves with two matrices namely the essential matrix and fundamental matrix. The essential matrix relates the projection point, p_l, in the left image with the one, p_r, in the right image. Setting the left camera as reference, the relationship as shown in Equation 43 is established.

$$\mathrm{P_r} = \mathrm{R}(\mathrm{P_l} - \mathrm{T}) \quad (43)$$

$$\mathrm{R} = \mathrm{R_r}(\mathrm{R_l})^{\mathrm{T}} \quad (44)$$

$$\mathrm{T} = \mathrm{T_r} + \mathrm{RT_l} \quad (45)$$

The rotation matrix (R) and translation matrix (T) can be obtained from Equations 44 and 45 (Bradski & Kaehler, 2008).

where

$\mathrm{P_r}, \mathrm{P_l}$ = projections of point P on the image planes of the right and left cameras

$\mathrm{R_l}, \mathrm{R_r}$ = Rotation matrix of the left and right cameras

$\mathrm{T_l}, \mathrm{T_r}$ = Translation matrix of the left and right cameras

Based on Equation 43, 44, and 45 the relationship between the projection points p_l and p_r and the essential matrix, E as shown in Equation 46 can be derived.

$$p_r^T \cdot R \cdot S \cdot p_l = 0$$
$$E = R \cdot S$$
$$S = \begin{bmatrix} 0 & -T_z & T_y \\ T_z & 0 & -T_x \\ -T_y & T_x & 0 \end{bmatrix}$$
$$p_r^T \cdot E \cdot p_l = 0 \quad (46)$$

where
E = product of the rotation matrix and S matrix which contains translation parameters

Since the essential matrix only involves with the external parameters, the fundamental matrix is introduced to correlate the coordinates of conjugate points within the image (Bradski & Kaehler, 2008). The projection point, q, relates to the real world point, p, by the camera matrix, M, as shown in Equation 46. This equation can be rewritten to Equation 48, and substituted in Equation 46 which gives to Equation 49. Rearranging the equation yields the equation for the fundamental matrix, Equation 50, and the equation relating the projection points of the left and right images, Equation 51.

$$q = Mp \quad (47)$$
$$p = M^{-1}q \quad (48)$$
$$q_r^T (M_r^{-1})^T E M_l^{-1} q_l = 0 \quad (49)$$
$$F = (M_r^{-1})^T E M_l^{-1} \quad (50)$$
$$q_r^T F q_l = 0 \quad (51)$$

2.3.3 Stereo Image Rectification

Stereo image rectification is the process of re-projecting the images of the left and right camera on an image plane which is parallel to the baseline (Scharstein, 1997). It makes the search of the corresponding points reliable and computationally tractable (Bagga, 2013). The search is performed within the epipolar geometry as shown in Figure 2.3.3. Specifically, it is executed along the epipolar lines which are the intersection of the epipolar plane and the image planes. The epipole is the intersection of the image plane and baseline O_lO_r. It is defined as the projection of the optical center of a camera on the image plane of the other camera. The epipolar plane is bounded by the optical center of the left, O_l, and right, O_r, camera and point

P. For a frontal parallel configuration, the image plane is parallel to the baseline as seen in Figure 2.3.4. This makes the epipolar line horizontal and the epipole approaches infinity.

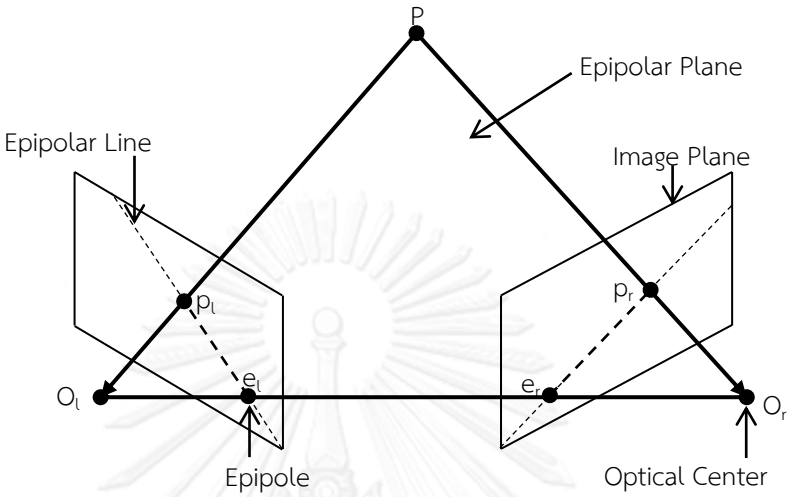

Figure 2.3.3 General configuration of a stereo vision system (Bradski & Kaehler, 2008)

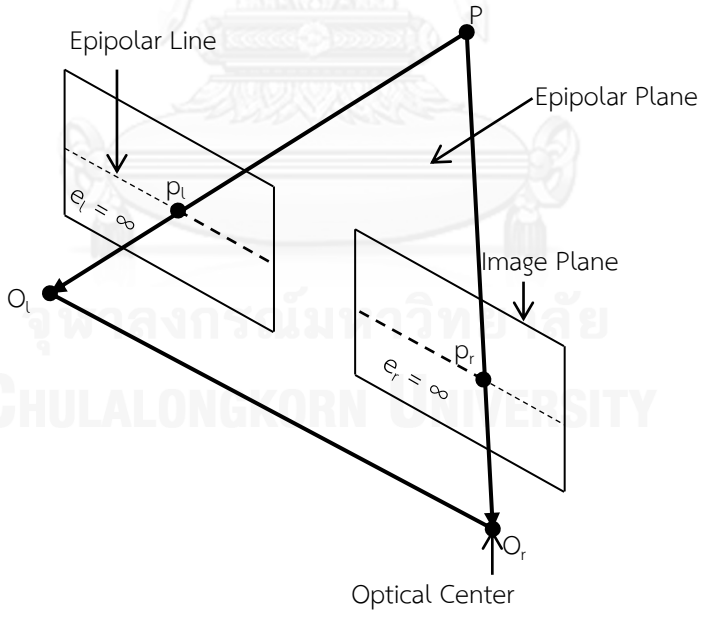

Figure 2.3.4 Frontal parallel configuration of a stereo vision system (Bradski & Kaehler, 2008)

The Bouguet's algorithm for stereo image rectification is an algorithm that minimizes the amount of change in re-projection for both images in order to reduce

the rep-projection distortion while maximizing common viewing area (Bradski & Kaehler, 2008). The re-projection distortion is minimized by dividing the rotation matrix R by half resulting in two rotation matrixes for the left and right image, $\mathbf{r_l}$ and $\mathbf{r_r}$. This process creates a coplanar alignment between two images. In the process of stereo rectification, the left image is set as the origin of the stereo vision system. The rotation matrix $\mathbf{R_{rect}}$ is determined to adjust the orientation of the epipole towards infinity and align the epipolar lines with the horizontal axis in the rectified images. The rotation matrix $\mathbf{R_{rect}}$ consists of three vectors as shown in Equation 52.

$$\mathbf{R_{rect}} = [\mathbf{e_1} \quad \mathbf{e_2} \quad \mathbf{e_3}]^T \tag{52}$$

Vector $\mathbf{e_1}$ is the direction of the epipole that is coincident along the translation vector between the two camera's optical centers.

$$\mathbf{e_1} = \frac{T}{\|T\|} \tag{53}$$

where
$T = [T_X \quad T_Y \quad T_Z]^T$

The matrix must be orthogonal, $\mathbf{e_2}$ and $\mathbf{e_3}$ can be computed as:

$$\mathbf{e_2} = \frac{[-T_y \quad T_x \quad 0]}{\sqrt{T_x^2 + T_y^2}} \tag{54}$$

$$\mathbf{e_3} = \mathbf{e_1} x \, \mathbf{e_2} \tag{55}$$

In order to align the row of the two images the rotation matrix $\mathbf{R_{rect}}$ is multiplied to the rotation matrix that adjusts both images into coplanar alignment. The whole process of stereo image rectification is shown in Figure 2.3.5.

$$\mathbf{R_l} = \mathbf{R_{epi}} \mathbf{r_l} \tag{56}$$

$$\mathbf{R_r} = \mathbf{R_{epi}} \mathbf{r_r} \tag{57}$$

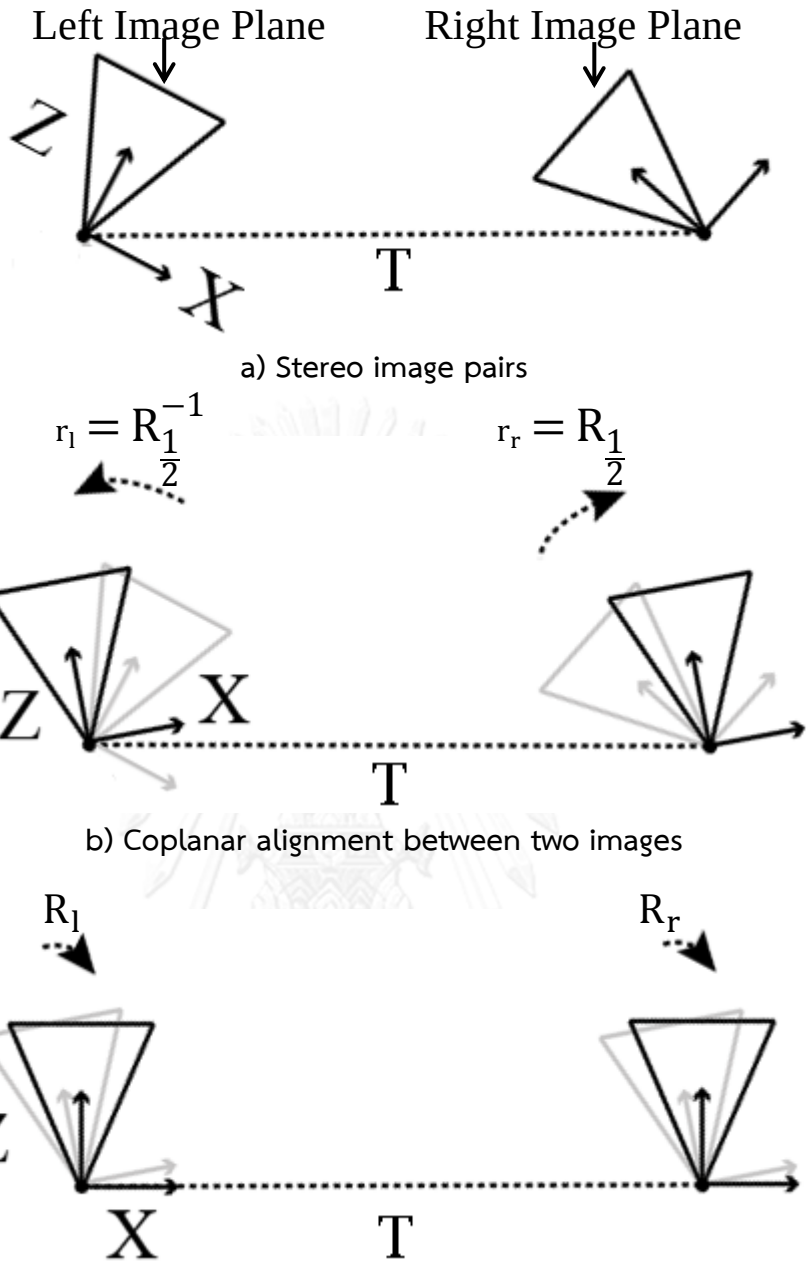

Figure 2.3.5 Process of Bouguet's Algorithm for Stereo Image Rectification (Hornáček, 2013)

2.3.4 Stereo Correspondence

Stereo correspondence is the stage when the match between the field of view of the left and right image is established (Saidon et al., 2009). Specifically block-matching stereo correspondence algorithm is applied in determining correspondence. This

process is divided into three stages namely, pre-filtering, correspondence search and post-filtering.

The pre-filtering enhances the texture and normalizes the image brightness. Sobel filter performs the convolution between the horizontal sobel kernel and the stereo image's RGB component (Sach, Atsuta, Hamamoto, & Kondo, 2009).

Stereo correspondence search is performed by the sum of absolute difference (SAD) algorithm. The SAD algorithm computes the intensity differences for each center pixel (x, y) in a $\mathbf{v_x}$ by $\mathbf{v_y}$ window, W, (Kuhl, 2005). The SAD value of a center pixel (x, y) is computed from:

$$\mathrm{SAD_v}(x, y) = \sum_{(i,j)\in W} |I_l(i, j) - I_r(x + i, y + j)| \quad (58)$$

where
I_l = array of pixel intensity of the left image
I_r = array of pixel intensity of the right image

Through Equation 58, the disparity is the (i, j) that minimize the SAD value. As seen in Figure 2.3.6, as the window size for correspondence is being increased a better depth map can be obtained. Since, a greater neighborhood is considered during matching which increases the assurance in determining the correct corresponding pixel. Furthermore, correspondence must be performed with sub-pixel accuracy under bilinear interpolation. This refines the result of the depth map by removing erroneous values and replacing it with values predicted from interpolation.

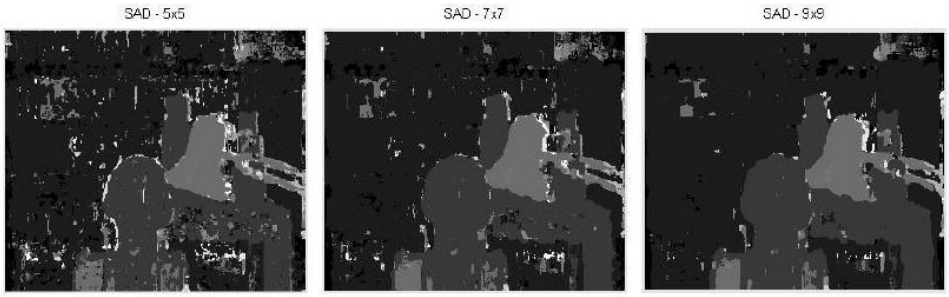

Figure 2.3.6 Effects of varying the window size during SAD computation (Kuhl, 2005)

In this study, post-filtering is performed after the correspondence search to eliminate bad matches. The speckle filter is used to mask invalid results and replace them by interpolated values. The filter has two parameters namely, speckle window size and speckle range.

2.3.4.1 Re-projection of 3D Coordinates

Re-projection is a process of recovering the depth map of an object. The re-projection matrix (Q) is used to re-project the 2D coordinates in the rectified images into its 3D position with an aid of the disparity values (Bradski & Kaehler, 2008).

$$\begin{bmatrix} X \\ Y \\ Z \\ W \end{bmatrix} = Q \begin{bmatrix} x \\ y \\ d \\ 1 \end{bmatrix} \tag{59}$$

where

$$Q = \begin{bmatrix} 1 & 0 & 0 & -c_x \\ 0 & 1 & 0 & -c_y \\ 0 & 0 & 0 & f \\ 0 & 0 & -\frac{1}{T_x} & \frac{c_x - c'_x}{T_x} \end{bmatrix}$$

c_x = horizontal distance from the principal point to the optical center on the image plane of the left image

c_y = vertical distance from the principal point to the optical center on the image plane of the left image

f = focal length

T_x = baseline

c'_x = horizontal distance from the principal point to the optical center on the image plane of the right image

$$\begin{aligned} X_{realworld} &= \frac{X}{W} \\ Y_{realworld} &= \frac{Y}{W} \\ Z_{realworld} &= \frac{Z}{W} \end{aligned} \tag{60}$$

2.3.5 Range of Depth, Depth Resolution and Fractional Overlap

Range of depth is defined as the minimum and maximum depth that the stereo vision system can capture. It is defined as the maximum and minimum disparity values obtained from the stereo correspondence (Bradski & Kaehler, 2008). On the other hand, depth resolution is the accuracy that the binocular stereo vision can estimate the changes of depth of the object of interest. It is represented by the following equation (Fanto, 2012):

$$\Delta z = \frac{Z^2}{fT}\Delta d \tag{61}$$

where
Z = depth
f = focal length
T = baseline
Δd = smallest disparity value $\approx \frac{1}{5}$ pixel size
= where the pixel size is the physical size of pixels of the sensor

Depth resolution is inversely proportional to baseline. Thus, having a large baseline can increase the accuracy of the depth resolution. As seen in Figure 2.3.7, having a large baseline would result to a smaller area for the overlapping field of view. This would affect the stereo correspondence since searching for a match will be difficult. The smallest disparity value can be estimated from the one fifth of the pixel size. Another way to assure that the baseline used is optimum is to compute the fractional overlap defined by Equation 62. This equation is applicable for the binocular stereo vision under frontal parallel (Fanto, 2012). A value close to one means the arrangement provided a good overlap between the two cameras and is desirable. A smaller value on the other hand is still acceptable when the object lies near to the middle of the cameras.

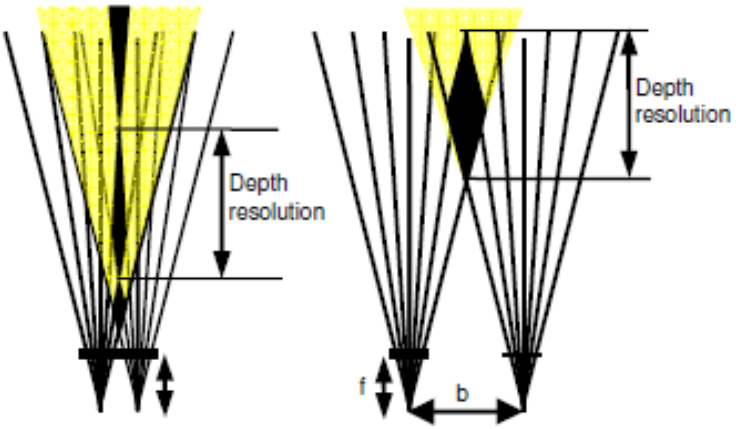

a) b)

Figure 2.3.7 Variation of depth resolution a) small baseline b) large baseline (Fanto, 2012)

$$\text{fractional overlap} = \frac{2Z\tan\frac{\theta}{2} - T}{2Z\tan\frac{\theta}{2}} \tag{62}$$

where

Z = depth

T = baseline

θ = field of view

The field of view is the angular extent the camera can capture in a given scene. It can be computed using the following equation (Sutton, Orteu, & Schreier, 2009):

$$\theta = 2\tan^{-1}\frac{D}{2f} \tag{63}$$

where

f = focal length

D = sensor size of the camera

2.4 Sensor-Lens Combination

A digital SLR camera has electronic light-gathering sensors in which images are impressed (Rojas, Gallipoli, & Wheeler, 2012). The full frame sensor (FF) and advanced photo system type-C (APS-C) are the typical sensors installed. The FF

sensor has a size that mimics a 35mm film while the APS-C is smaller but still maintains an aspect ratio of 3:2. Sensor size greatly affects photographic parameters such as resolution, pixel density, radial distortion, angle of view and depth of field. The parameters that are crucial in image processing are resolution, pixel density and radial distortion.

Resolution refers to the total number of pixels over the entire sensor area whereas pixel density refers to the number of pixels per unit area of the sensor. Lower pixel density implies a bigger pixel size. This reduces image noise and improves the artistic quality of pictures but this can be a problem when dealing with measurements. Accuracy is greatly influenced by the number of pixels over the point of the sensor area occupied by the specimen's image. From this, pixel density dictates the size and type of sensor to be used. In choosing the type of sensor it should be determined if the specimen fits the entire sensor area or not. If it fits, then a sensor with higher resolution is advantageous. When only a portion of the sensor area is covered then a sensor with higher pixel density should be considered. Since, a large number of pixels are occupied by the image over that portion of the sensor.

The combination of the sensor and the lens can greatly affect the quality of the image. Lenses can be either zoom or fix. Zoom lenses have the ability to change its focal length in order to have a better view of the object of concern. Fixed focal length lenses or prime lenses on the other hand can be classified into wide angle lens or telephoto lens. Wide angle lenses have focal distances smaller than 50mm while telephoto lenses have focal distances larger than 50mm. The telephoto lens is suitable in taking small details of objects at a long distance. The macro lens has a capability of focusing an object at much shorter distances than the telephoto lens. Among all types of prime lenses, the macro lenses produce the smallest distortion.

2.5 Advantages and Disadvantages of Image Processing

In recent years, the image processing measurements have been used in many researches. Advantages and disadvantages on its use were observed enumerated as follows (Islam, 2008; Viggiani & Hall, 2008):

2.5.1 Advantages of Image Processing

a. The measurement is not affected by the loading response of the specimen.
b. The deformation of the soil can be determined by on-line and off-line analyses.
c. Various properties of materials can be identified. Defects such as cracks, formation of shear bands and areas that localized deformation first appeared can be observed precisely. This can be a powerful means in interpreting results.
d. The development of deformation pattern and strain localization can be observed through tracking the specimen's response during the test.
e. Some errors associated with external measuring devices in the triaxial apparatus can be avoided. Such errors are enumerated in Table 2.5.1.

Table 2.5.1 Errors in Conventional Triaxial Test (Ibrahim, Orense, Pender, & Kikkawa, 2009; Ratananikom, Likitlersuang, & Yimsiri, 2007)

Types of Error	
Bedding Error This type of error is from the surface irregularities between the specimen, porous stone and top cap. It is also caused by the lack of fit at the ends of the specimen.	Seating Error This error is due to the closing of the gaps between the internal load cell, ram, top cap or base pedestal and porous stone.
Compliance Error The deflection of the internal load cell, extension of the tie bars that can cause a relative displacement of the top part of the cell with respect to the piston and the compression of the filter paper placed at the perimeter of the specimen causes the compliance error.	Alignment Error It is the result when the end faces of the specimen are non-perpendicular to the vertical axis of symmetry. The non-uniformity of the porous stone's thickness can also cause this error. Thus, the sample tends to tilt while it is being loaded.

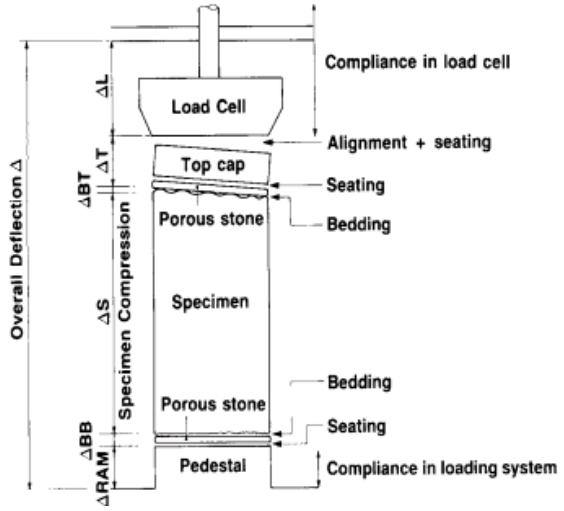

Figure 2.5.1 Illustration of locations of the errors

2.5.2 Disadvantages of Image Processing

The major disadvantage of image processing is the distortion. As previously discussed, it should be corrected by the proper combination of sensor-lens and

calibration. Since the accuracy of the measurements is affected by the camera, one should be careful in choosing the cameras.

2.6 Applications of Image Processing

Through the technology advancement the image processing is being used commonly in the field of geotechnical engineering and civil engineering.

H. Yamamoto applied the image processing technique to determine the displacement of sand in a direct shear apparatus (Yamamoto, 2008). In his experiments, one face of the shear box was replaced by a glass plate to provide a viewable area for a camera as shown in Figure 2.6.1. The shear bands formed during the experiments were observed. The technique was also used to relate the degree of rotation to the dilation characteristics of the soil particles during shear.

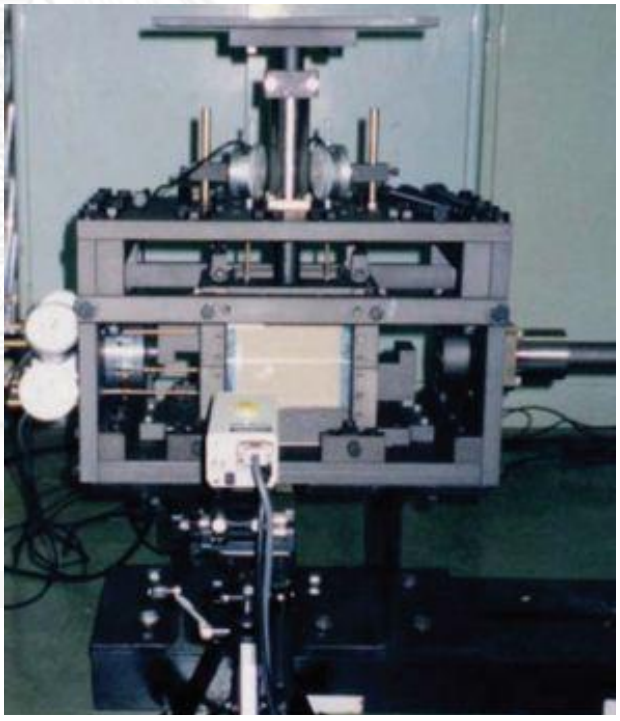

Figure 2.6.1 Experiment setup in determining the displacement of sand (Yamamoto, 2008)

H. Qiao, Y. Nakata and M. Hyodo applied image processing in testing unsaturated sandy soil in a triaxial apparatus (Qiao, Nakata, Hyodo, & Kikkawa, 2008). The global and local displacements and the volume change of the specimen were determined under a consolidated drained test. An observation window was made for the camera as shown in Figure 2.6.2. The camera was calibrated to remove the distortion due to the triaxial cell.

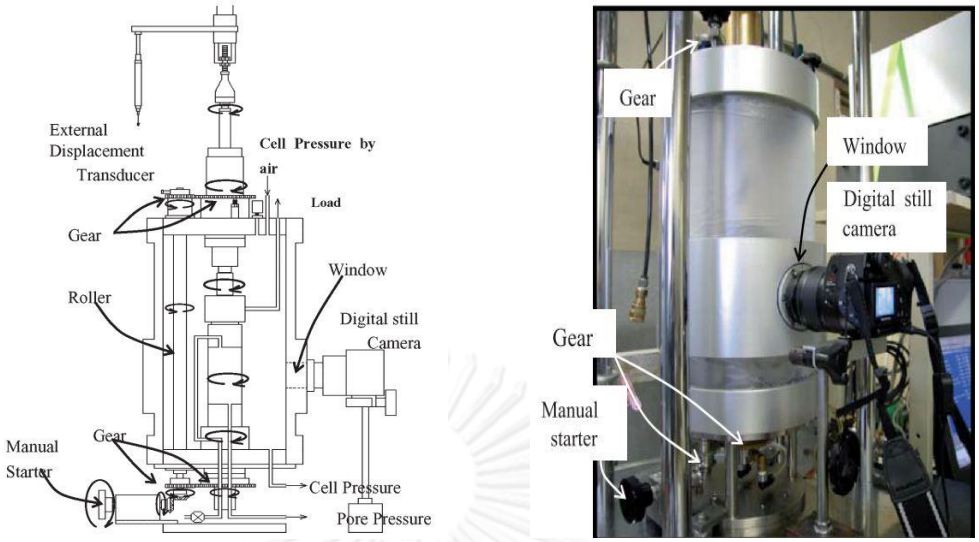

a) b)

Figure 2.6.2 a) Schematic diagram b) Actual experimental set-up (Qiao et al., 2008)

Gioacchino Viggiani and Stephen A. Hall did a research on different types of non-contact or full-field measurements such as false-relief stereophotography (FRS) and digital image correlation (DIC) (Viggiani & Hall, 2008). FRS was superseded by DIC due to the major developments in digital photography. DIC makes use digital rather than analogue photographs. It assesses the spatial transformation between two digital images which underwent image processing first. In this research, DIC was used to determine the strain localization of a soft clay specimen. The evolution of the strain localization is presented in Figure 2.6.3.

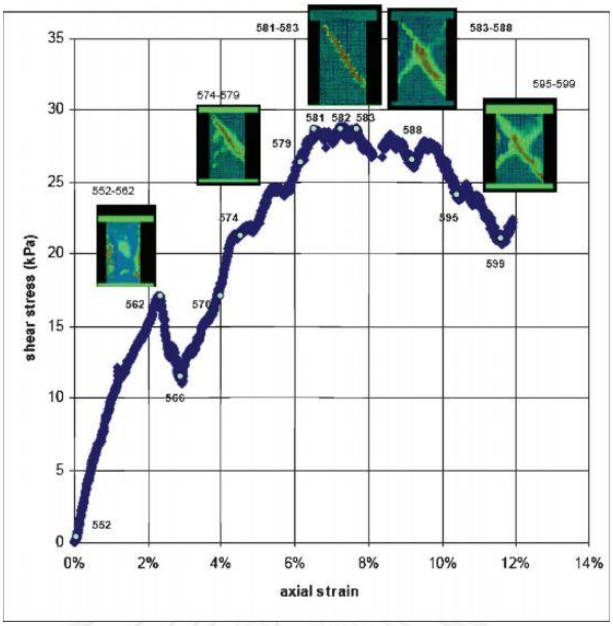

Figure 2.6.3 Strain localization and shear stress versus axial strain plot of soft clay (Viggiani & Hall, 2008)

J.M Rodriguez, J. M. A. Johansson and T. Edeskär applied image processing to quantitatively classify the shape of soil particles (Rodriguez, Johansson, & Edeskär, 2012). Figure 2.6.4 shows how the particle shape was being obtained.

Figure 2.6.4 An SLR camera was used to take the images of the soil sample (Rodriguez et al., 2012)

Mohammad Khosravi, Lin Tang, Thirapong Pipatpongsa et al investigated the performance of a counterweight in an undercut slope (Khosravi, Tang, Pipatpongsa, Takemura, & Doncommul, 2012). Figure 2.6.5 illustrates an experimental set-up in this research. It was proven from the research that the counterweight was an effective way to increase the stability of the undercut slope. A software following the particle image velocimetry (PIV) method called GeoPIV was used to determine the displacement of the slope.

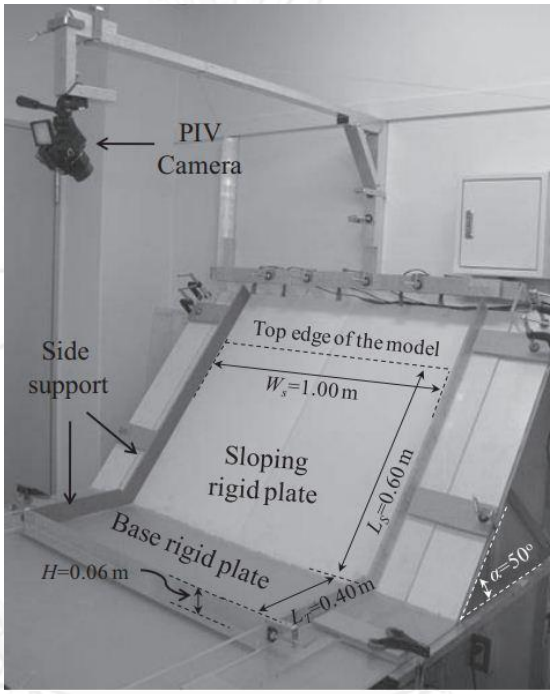

Figure 2.6.5 Experimental set-up for an undercut slope (Khosravi et al., 2012)

Mee-Seub Lim and Joonhong Lim used high speed cameras to monitor the rebound and penetration of piles during driving (Lim & Lim, 2008). As shown in Figure 2.6.6 a specially designed mark was attached to the pile for facilitating the image analysis.

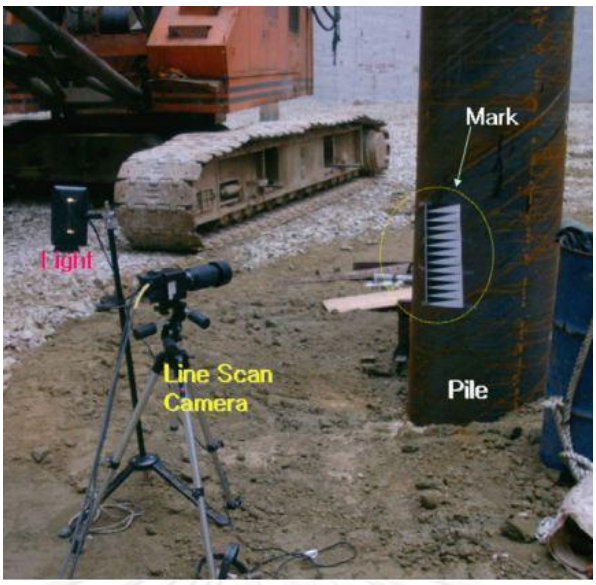

Figure 2.6.6 On site set-up for the visual measurement of pile movements (Lim & Lim, 2008)

Junggeun Han, Kikwon Hong and Sanghun Kim applied image processing and photogrammetry in assessing the current condition of an ancient structure (Han et al., 2012). The height and inclination of a seven story pagoda (Sinsedong Pagoda, Gyeongsangbuk-do, Korea) were monitored by CCD cameras installed along the perimeter.

Figure 2.6.7 Seven-story stone tower in Sinsedong Pagoda, Gyeongsangbuk-do, Korea. (Han et al., 2012)

2.7 Deformation Theory

2.7.1 Displacement and strain

The presence of external loads causes the deformation in soil. Displacements of soil particles can be represented by arrows known as displacement vectors. Undeformed and deformed configurations are shown in Figure 2.7.1. Po and P are connected by a relative position vector r. When it is deformed, a displacement vector u and u° at P and Po respectively can be defined. The deformation can be quantified from the change of the relative position vector, r, as shown in Equation 64.

$$\Delta r = r' - r = u - u^0 \tag{64}$$

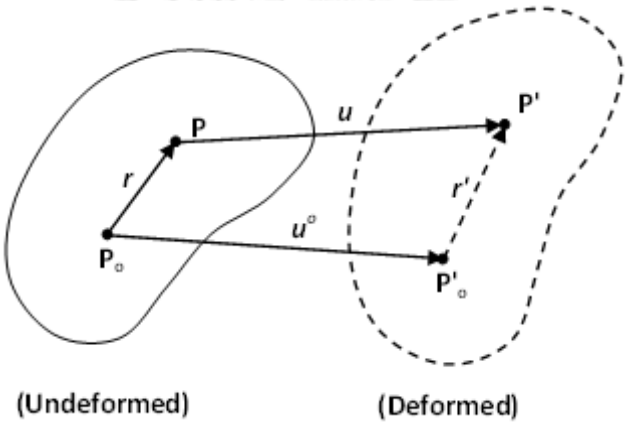

Figure 2.7.1 Deformation between two points (Sadd, 2005)

To express the components of displacement vector u, Taylor series expansion was applied around point Po and the following was obtained:

$$u = u^0 + \frac{\partial u}{\partial x} r_x + \frac{\partial u}{\partial y} r_y + \frac{\partial u}{\partial z} r_z \tag{65}$$

$$v = v^0 + \frac{\partial v}{\partial x} r_x + \frac{\partial v}{\partial y} r_y + \frac{\partial v}{\partial z} r_z \tag{66}$$

$$w = w^0 + \frac{\partial w}{\partial x} r_x + \frac{\partial w}{\partial y} r_y + \frac{\partial w}{\partial z} r_z \tag{67}$$

The components of the change of the relative position vector, r, can be determined through Equation 65, 66, and 67. It results to the following equations:

$$\Delta r_x = r_x - r_x^0 = \frac{\partial u}{\partial x} r_x + \frac{\partial u}{\partial y} r_y + \frac{\partial u}{\partial z} r_z \tag{68}$$

$$\Delta r_y = r_y - r_y^0 = \frac{\partial v}{\partial x} r_x + \frac{\partial v}{\partial y} r_y + \frac{\partial v}{\partial z} r_z \quad (69)$$

$$\Delta r_z = r_z - r_z^0 = \frac{\partial w}{\partial x} r_x + \frac{\partial w}{\partial y} r_y + \frac{\partial w}{\partial z} r_z \quad (70)$$

Equation 68, 69, and 70 can be rewritten in index notation as shown:

$$\Delta r_i = u_{i,j} r_j \quad (71)$$

where

$u_{i,j}$ = displacement gradient tensor

$$u_{i,j} = \begin{bmatrix} \frac{\partial u}{\partial x} & \frac{\partial u}{\partial y} & \frac{\partial u}{\partial z} \\ \frac{\partial v}{\partial x} & \frac{\partial v}{\partial y} & \frac{\partial v}{\partial z} \\ \frac{\partial w}{\partial x} & \frac{\partial w}{\partial y} & \frac{\partial w}{\partial z} \end{bmatrix}$$

The displacement gradient tensor can be written as having a symmetric and anti-symmetric variable as shown:

$$u_{i,j} = e_{ij} + w_{ij} \quad (72)$$

where

e_{ij} = strain tensor

$$e_{ij} = \frac{1}{2}\left(u_{i,j} + u_{j,i}\right) \quad (73)$$

w_{ij} = rotation tensor

$$w_{ij} = \frac{1}{2}\left(u_{i,j} - u_{j,i}\right) \quad (74)$$

2.8 Strain Field

A field is a space where each point is associated with a quantity of some kind (Means, 1976). The quantity may be a scalar, a vector or a tensor. Strain fields, a find of tensor field can be derived from the displacement field. For instance, Lagrangian strain tensor can be obtained from the displacement field as shown below (Tung & Sui, 2010).

$$\varepsilon_{xx} = \frac{\partial u}{\partial x} + \frac{1}{2}\left[\left(\frac{\partial u}{\partial x}\right)^2 + \left(\frac{\partial v}{\partial x}\right)^2\right] \quad (75)$$

$$\varepsilon_{yy} = \frac{\partial \mathrm{v}}{\partial \mathrm{y}} + \frac{1}{2}\left[\left(\frac{\partial \mathrm{u}}{\partial \mathrm{y}}\right)^2 + \left(\frac{\partial \mathrm{v}}{\partial \mathrm{y}}\right)^2\right] \quad (76)$$

$$\varepsilon_{xy} = \frac{1}{2}\left[\frac{\partial \mathrm{u}}{\partial \mathrm{y}} + \frac{\partial \mathrm{v}}{\partial \mathrm{x}}\right] + \frac{1}{2}\left[\frac{\partial \mathrm{u}}{\partial \mathrm{x}}\frac{\partial \mathrm{u}}{\partial \mathrm{y}} + \frac{\partial \mathrm{v}}{\partial \mathrm{y}}\frac{\partial \mathrm{v}}{\partial \mathrm{x}}\right] \quad (77)$$

On the other hand, it can also be obtained in a three dimensional space (Sutton, Yan, Deng, Cheng, & Zavattieri, 2007).

$$\varepsilon_{xx} = \frac{\partial \mathrm{u}}{\partial \mathrm{x}} + \frac{1}{2}\left[\left(\frac{\partial \mathrm{u}}{\partial \mathrm{x}}\right)^2 + \left(\frac{\partial \mathrm{v}}{\partial \mathrm{x}}\right)^2 + \left(\frac{\partial \mathrm{w}}{\partial \mathrm{x}}\right)^2\right] \quad (78)$$

$$\varepsilon_{yy} = \frac{\partial \mathrm{v}}{\partial \mathrm{y}} + \frac{1}{2}\left[\left(\frac{\partial \mathrm{u}}{\partial \mathrm{y}}\right)^2 + \left(\frac{\partial \mathrm{v}}{\partial \mathrm{y}}\right)^2 + \left(\frac{\partial \mathrm{w}}{\partial \mathrm{y}}\right)^2\right] \quad (79)$$

$$\varepsilon_{xy} = \frac{1}{2}\left[\frac{\partial \mathrm{u}}{\partial \mathrm{y}} + \frac{\partial \mathrm{v}}{\partial \mathrm{x}}\right] + \frac{1}{2}\left[\frac{\partial \mathrm{u}}{\partial \mathrm{x}}\frac{\partial \mathrm{u}}{\partial \mathrm{y}} + \frac{\partial \mathrm{v}}{\partial \mathrm{y}}\frac{\partial \mathrm{v}}{\partial \mathrm{x}} + \frac{\partial \mathrm{w}}{\partial \mathrm{y}}\frac{\partial \mathrm{w}}{\partial \mathrm{x}}\right] \quad (80)$$

CHAPTER 3

3 Methodology

For this research, a binocular stereo vision system was developed for measuring the movement of soil in three dimensional space. The development was divided into three phases namely, the calibration phase, the stereo vision phase and the 3D measurement phase.

3.1 Calibration Phase

Calibration is an essential process for reliable measurements. The calibration phase was divided into two stages consisting of 2D calibration and the 3D calibration.

3.1.1 Stage 1: 2D Camera Calibration

Prior to the calibration for the stereo vision system, 2D camera calibration was performed to eliminate the distortion. This stage involves the determination of the internal and external parameters of cameras as discussed in section 2.1.3.3.4 of Chapter 2. Presented in this section are procedures for calibrating a single camera which were implemented in Labview.

1.) A panel of dotted grid having a spacing of 2 cm center to center was placed in front of the object of concern at different orientations in a range of $\pm$ 20 degrees. Caution was made to ensure that the first image was in the field of view of the camera so that the dots can be visibly seen.

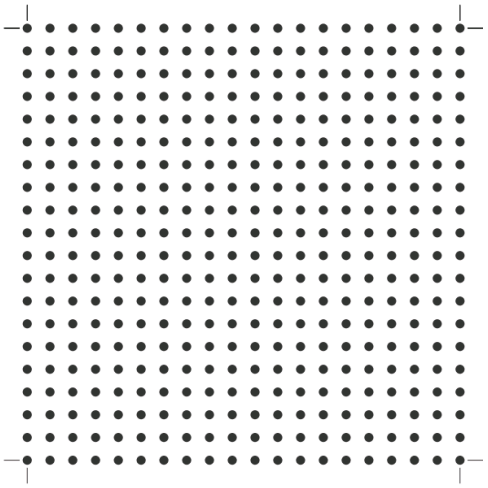

Figure 3.1.1 Sample calibration panel

2.) A threshold value was used to extract the grid feature of the calibration panel from pictures taken from the previous step.

3.) The calibration axis was established at the upper left corner of the grid.

4.) The internal, distortion and external parameters were estimated using the equations in Section 2.1.3.3.2, 2.1.3.3.3 and 2.1.3.3.4.

5.) The camera parameters maximum likelihood estimation can be refined through minimizing Equation 36.

3.1.2 Stage 2: Calibration for 3D measurement

In this stage a cube, Figure 3.1.2.a, was placed inside the triaxial cell to determine the appropriate focal length, baseline or separation between the two cameras and image resolution. The cube was used since its straight edges can be easily detected by image processing routines. The size of the cube was 9.9 x 7.5 x 6 cm. Miscellaneous parameters were varied until an optimum configuration was obtained. The configuration is optimum when it can provide a good coverage area of the object of concern. To evaluate the coverage area stereo correspondence must be performed to check if the system can reconstruct the disparity image of the object of concern. A good disparity image must have an almost equal distribution of values for the region of the object of concern. Furthermore, the image must be similar to the actual appearance of the object of concern.

a) b)

Figure 3.1.2 a) Cube b) Cube with marks

During this stage, the magnification error for the selected focal length and the distance of the camera from the object of concern was also determined. The magnification error was due to the triaxial cell that is made of plexiglass. This causes an increase in the dimension of the object that is placed inside the triaxial apparatus. To obtain this parameter, markers were placed on the cube and measured through image processing. As seen in Figure 3.1.2.b, markers of heights 3 cm, 2 cm and 1.5 cm were placed on the cube. The real dimension was plotted against the system measured dimension and from this the magnification factor was obtained. The markers were also placed inside and outside the triaxial cell for every test to serve as a reference for orientation checking.

3.2 2D Image Processing

The binocular stereo vision system was built on top of the 2D image processing system. Therefore the development for 2D measurement was implemented first. A system was made for checking the capacity of each camera that will be used in the binocular system. Calibration was performed similar to Section 3.1.

3.2.1 Accuracy check

A rubber cylinder with a height of 12.7 cm and a diameter of 5.8 cm was used to check the accuracy of the system. An angle bar as shown in Figure 3.2.1 was attached on the specimen to serve as the support for the LVDT. Three strain gauges were attached at the top, middle and bottom part of the specimen. Lucas and

Kanade pyramidal optical flow algorithm was used to track the movements of marked points. 10 sets of readings up to 1.27 cm were made in steps of 0.5 mm and 1 mm.

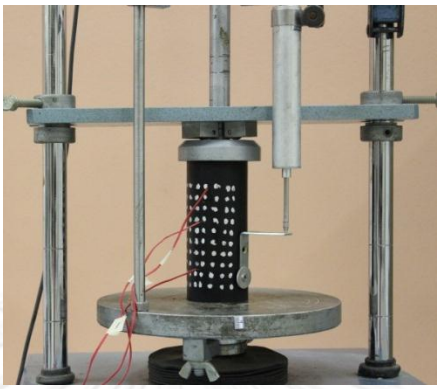

a)

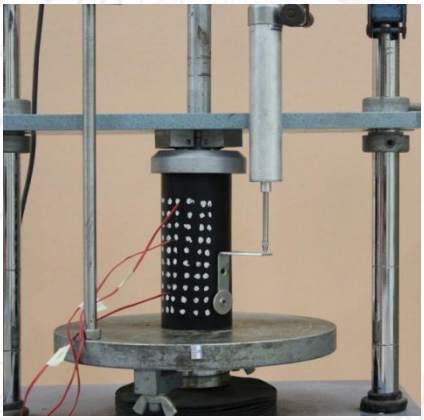

b)

Figure 3.2.1 Accuracy check using a rubber cylinder a) left image b) right image

3.2.2 Triaxial test

Two Bangkok soft clay samples taken from depths of 6 m to 7 m (BH1) and 9 m to 10 m (BH2) were tested. It can be seen in Figure 3.2.2, that a grid of dots was drawn on the membrane. A ruler was placed inside the triaxial cell to serve as a reference during the test. Consolidated drained compression unloading triaxial test was performed having a cell pressure of 50kPa for BH1 and 100kPa for BH2. For the compression unloading part of the test, it was done by increasing the deviator stress while reducing the cell pressure so that the mean effective stress decreased. Two Canon 650D cameras were used and pointed parallel towards the triaxial apparatus. Pictures were taken every hour with the use of timer remote controls.

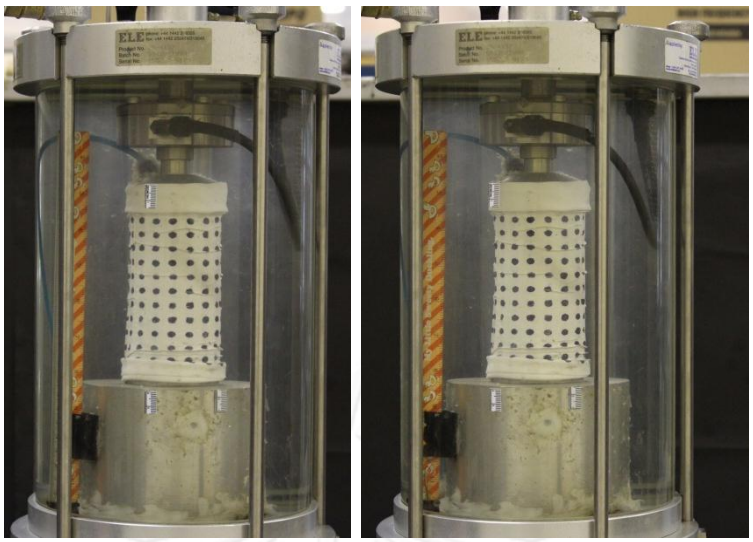

a) b)

Figure 3.2.2 Triaxial experiment set-up for the sample a) left image b) right image

3.3 Binocular Stereo Vision System

3.3.1 Stereo Vision Implementation

For a binocular stereo vision system, series of processes as shown in Figure 3.3.1 are needed to achieve the 3D position of a desired point. The role of each process was discussed in Section 2.3.

The flowchart for the developed program is presented in Figure 3.3.2. The first step is to calibrate the two cameras independently. Both cameras must see the calibration panel at the same time. They must also have a clear view of all dots in the calibration panel for a good calibration result. Then, the result from the independent calibration will be loaded to the stereo calibration program. In Labview, an error statistics can be generated that ensures the quality of the calibration. The calibration and the rectification quality must be within the range of 0.7 to 1.0. Having a calibration quality of 1.0 would mean that the system is perfectly calibrated. On the other hand the maximum rectification error should not exceed 1.5. When one of these parameters is not satisfied the stereo calibration must be repeated with some parameters adjusted. Following stereo calibration is rectification. The left image was assigned to be the reference image during rectification. The next step is stereo correspondence and consists of pre-filtering, correspondence and post-filtering. For the pre-filter settings, a sobel filter having a filter size of 11 and filter cap of 31 was

used. For the correspondence settings, SAD algorithm was implemented having a window size of 25 and a minimum disparity of 10. A target starting readable depth was set to 100cm. This limits the program to perform correspondence from 100 cm away from the cameras. Objects located less than 100 cm will be disregarded. Lastly for the post-filter settings, a speckle window size of 5 and a speckle range of 200 were used. More so, the correspondence was done with subpixel accuracy by further interpolating the disparities obtained by bilinear interpolation. The last step for stereo vision is the re-projection of the depth and 3D position with respect to the world coordinate of the object of concern. The origin of the world coordinate system was based on the left camera.

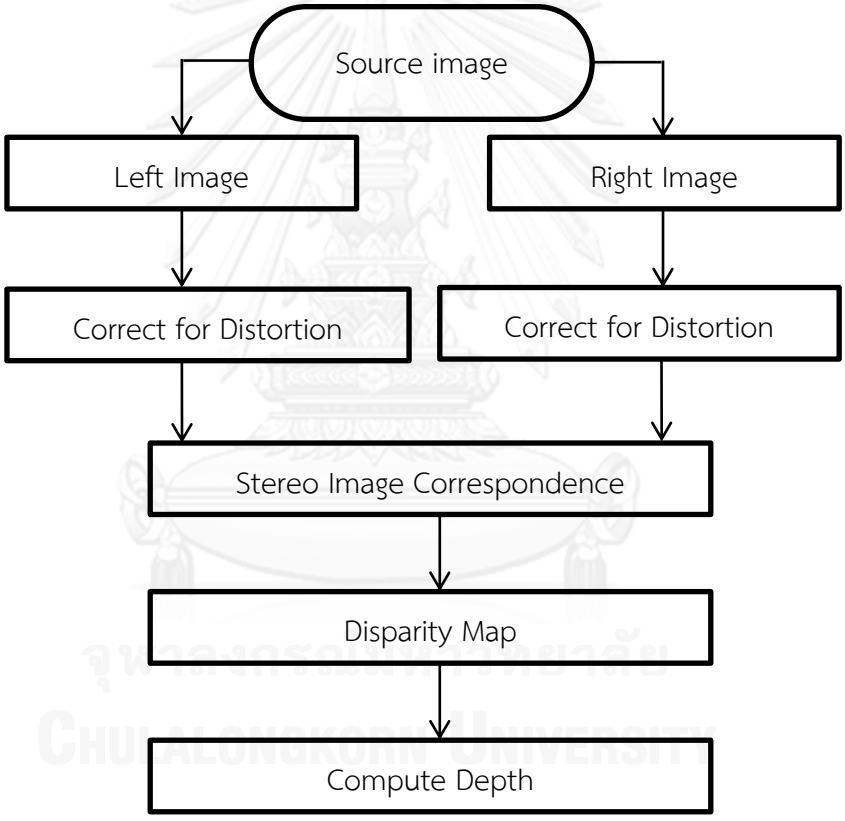

Figure 3.3.1 Process of stereo vision

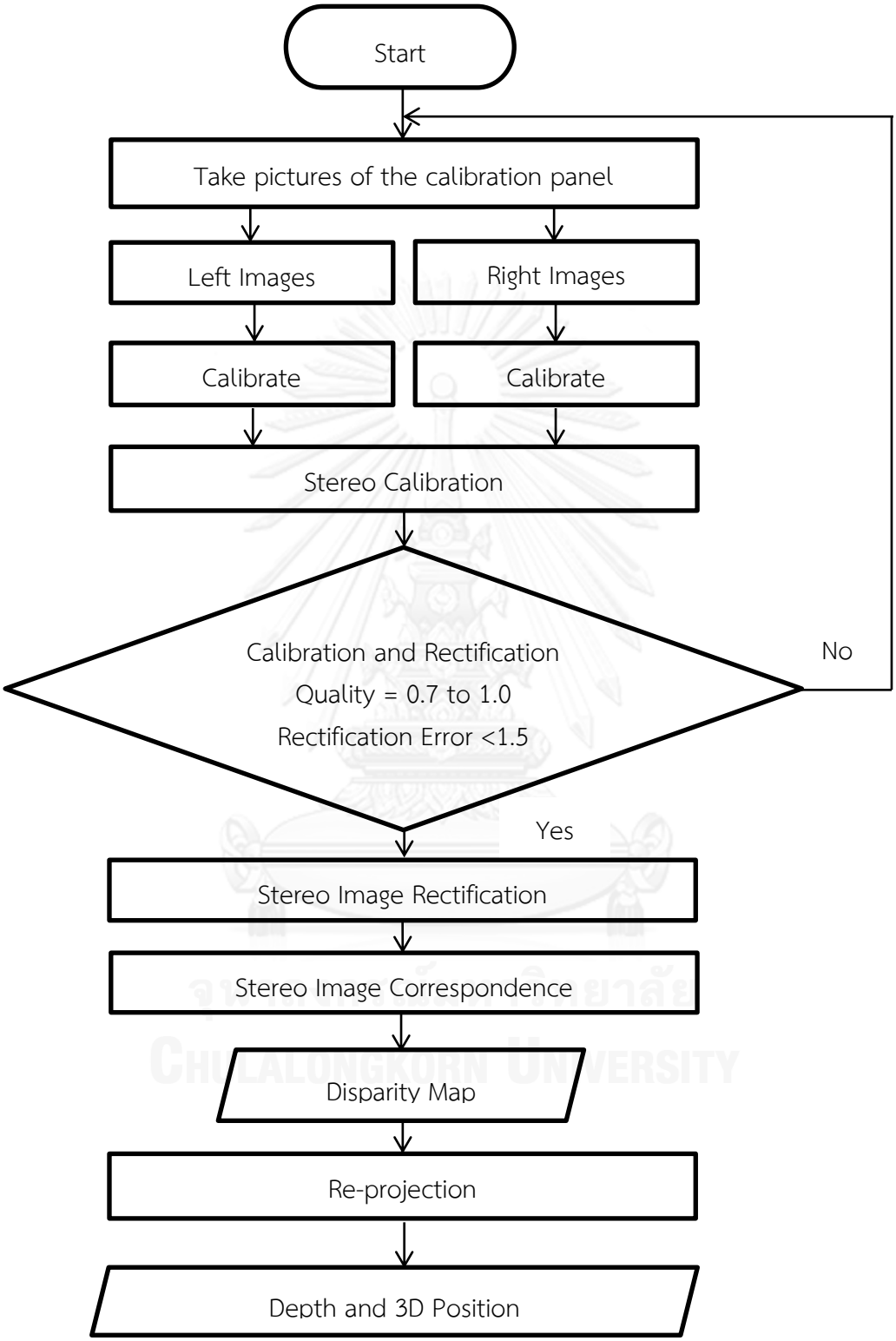

Figure 3.3.2 Flowchart of the program developed in Labview

3.3.2 Bilinear Interpolation

The result from stereo correspondence can be refined by bilinear interpoilation which uses the distance weighted average of the four nearest pixel value in order to estimate the new pixel value (Acharya & Tsai, 2007). As shown in Figure 3.3.3, the intensity value I(x, y) at the interpolated point P can be estimated as:

$$I(x,y) = \frac{(x_2-x)(y_2-y)}{(x_2-x_1)(y_2-y_1)} I(x_1,y_1) + \frac{(x-x_1)(y_2-y)}{(x_2-x_1)(y_2-y_1)} I(x_2,y_1) + \frac{(x_2-x)(y-y_1)}{(x_2-x_1)(y_2-y_1)} I(x_1,y_2) + \frac{(x-x_1)(y-y_1)}{(x_2-x_1)(y_2-y_1)} I(x_2,y_2)$$

$$I(x,y) = w_1 I(x_1,y_1) + w_2 I(x_2,y_1) + w_3 I(x_1,y_2) + w_4 I(x_2,y_2) \quad (81)$$

where

$I(x_1,y_1), I(x_2,y_1), I(x_1,y_2), I(x_2,y_2)$ = intensity values of the neighboring points

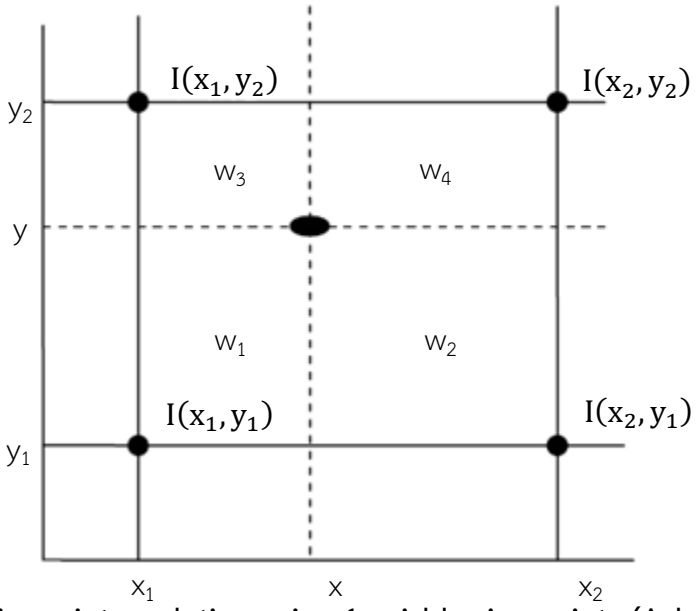

Figure 3.3.3 Bilinear interpolation using 4 neighboring points (Acharya & Tsai, 2007)

3.3.3 Validation for Depth Reading

To thoroughly check the accuracy of the system, a small card board was attached on a micrometer as seen in Figure 3.3.4. It is placed on the triaxial base at a distance of 105cm from the cameras. Ten readings were made when the cardboard was

moved in steps of 0.05, 0.1, 0.2, 0.4, 0.6, and 0.8 cm along the micrometer axis. The standard deviation from both increments was computed and used to express the repeatability of the system.

Figure 3.3.4 Experimental set up for determining the accuracy and repeatability

Figure 3.3.5 Experimental set up for determining the accuracy with respect to the triaxial apparatus

3.3.4 Calibration for Volume Measurement

The change in volume of a specimen under triaxial testing correlates with its radial and axial deformation. Therefore an experiment was carried out to verify that the developed system is also useful for volume measurement. To calculate the volume change correctly, the radial movements shall be measured for all directions around the vertical axis. However the radial deformation was determined from only one direction in this study because of limited equipments. In this study, a proof-of-concept experiment was made under an assumption that the radial deformation of the specimen would be uniform. A cylindrical sponge of height 10.5 cm and diameter of 6 cm was tested instead of a soil as seen in Figure 3.3.6. This is to have a better control on the amount of water that flows into it. A dense dot pattern was marked on the specimen for this test to enhance the quality of the stereo correspondence process. During the test, the cell pressure was kept slightly higher than the back pressure to ensure a gradual change in volume of the sample. Pictures were taken every 10 seconds while water was being injected to the sample.

Figure 3.3.6 Sponge tested

Figure 3.3.7 Pattern of the membrane

To compute the change of volume, the monitored area was divided into NxN patches. I_i represents the reference image and I_f represents the succeeding image. The volume of the brick can be computed from triple integration as shown in Equation 82.

$$\int_{z_L}^{z_u}\int_{y_L}^{y_u}\int_{x_L}^{x_u} dx\, dy\, dz = \int_{-1}^{1}\int_{-1}^{1}\int_{-1}^{1} d\xi\, d\eta\, d\zeta \tag{82}$$

Each patch was then used to form an 8-node brick element using the reference position and the deformed position as the back and front faces, respectively as shown in Figure 3.3.8.

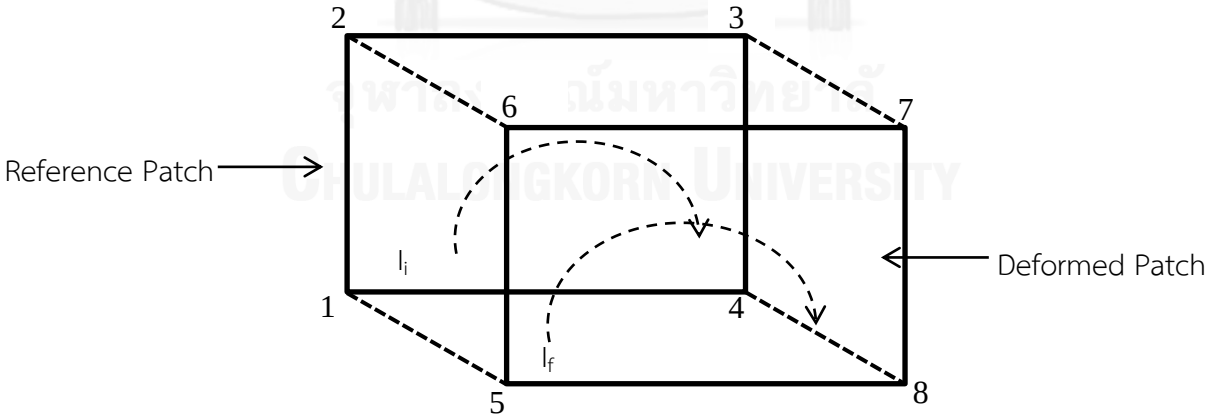

Figure 3.3.8 Node assignments and orientation

The equation can be simplified by applying chain rule and the transformation of integration domain to a range [-1, +1] for all three directions as shown below:

$$\int_{z_L}^{z_u}\int_{y_L}^{y_u}\int_{x_L}^{x_u} dx\, dy\, dz = \int_{-z_L}^{+z_u}\int_{-y_L}^{+y_u}\int_{-x_L}^{+x_u} dx\, dy\, dz \quad (83)$$

The Jacobian matrix, J, can be computed from the product of the shape function and the coordinate matrix as shown in Equation 84.

$$J = [N][x \quad y \quad z]_{nodes} \quad (84)$$

where

$$\text{Shape Function, } N = \begin{bmatrix} \frac{\partial N}{\partial \xi} \\ \frac{\partial N}{\partial \eta} \\ \frac{\partial N}{\partial \zeta} \end{bmatrix} = \frac{1}{8}\begin{bmatrix} -1 & -1 & 1 & 1 & -1 & -1 & 1 & 1 \\ -1 & 1 & 1 & -1 & -1 & 1 & 1 & -1 \\ -1 & -1 & -1 & -1 & 1 & 1 & 1 & 1 \end{bmatrix}$$

After rearranging, Equation 83 can be simplified as shown:

$$\text{Volume} = 8 * \det(J) \quad (85)$$

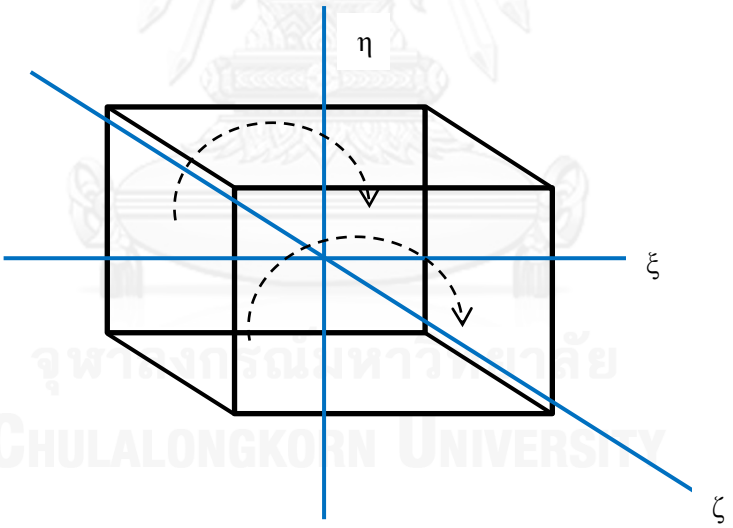

Figure 3.3.9 Shape function representation and axis

3.3.5 Validation for Depth Reading under Tilting Planes

In order to determine the capacity of the system to read depth changes under tilting planes, a laser transducer was used to get the profile of a deformed sample and it was compared to the result of the system. Oil clay was used as a sample since it is easy to manipulate. Readings were made at the center, 40° from the center and

boundary of the sample as seen in Figure 3.3.10. The profile was read for 10 times at the center and 40° from the center of the sample. For the profile at the boundary of the sample, only 3 readings were made.

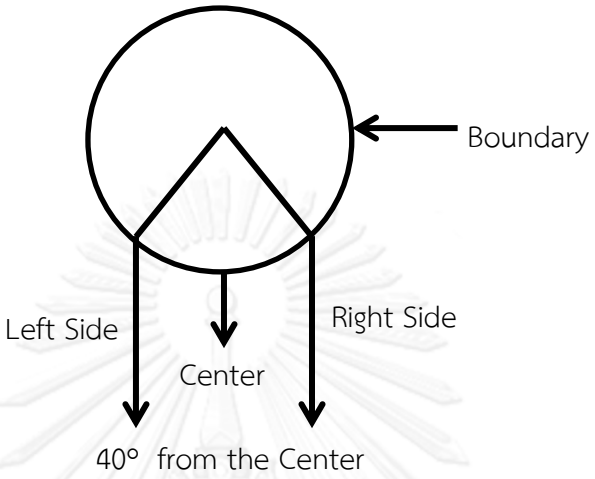

Figure 3.3.10 Locations of readings

a) **b)**

Figure 3.3.11 Set-up of the experiment

3.4 Optical Flow: Lucas and Kanade Pyramidal Optical Flow Algorithm

An optical flow algorithm specifically Lucas and Kanade pyramidal optical flow was adopted to track the position of points. The general procedure of the algorithm was discussed in Section 2.2.1.2. The flowchart of developed program is shown in Figure 3.4.1.

First a reference image and a succeeding image was chosen. The reference image was first loaded to the stereo vision program. When the disparity map was obtained the region of interest (ROI) was selected. Then the succeeding image was processed to the stereo vision program. From the disparity map of the two images the points within the region of interest was searched using Equation 34. It was minimized through least squares and iterated for 5 times. A pyramid level of 4 was used for the pyramidal implementation of the algorithm. Furthermore, a window size of 15 was adopted in searching the match of the points. When the matched was determined, the position of the points at its initial condition and succeeding condition was extracted. These positions were then re-projected to its 3D real world position. The reference was set at the left camera. From the 3D positions the displacement can be obtained.

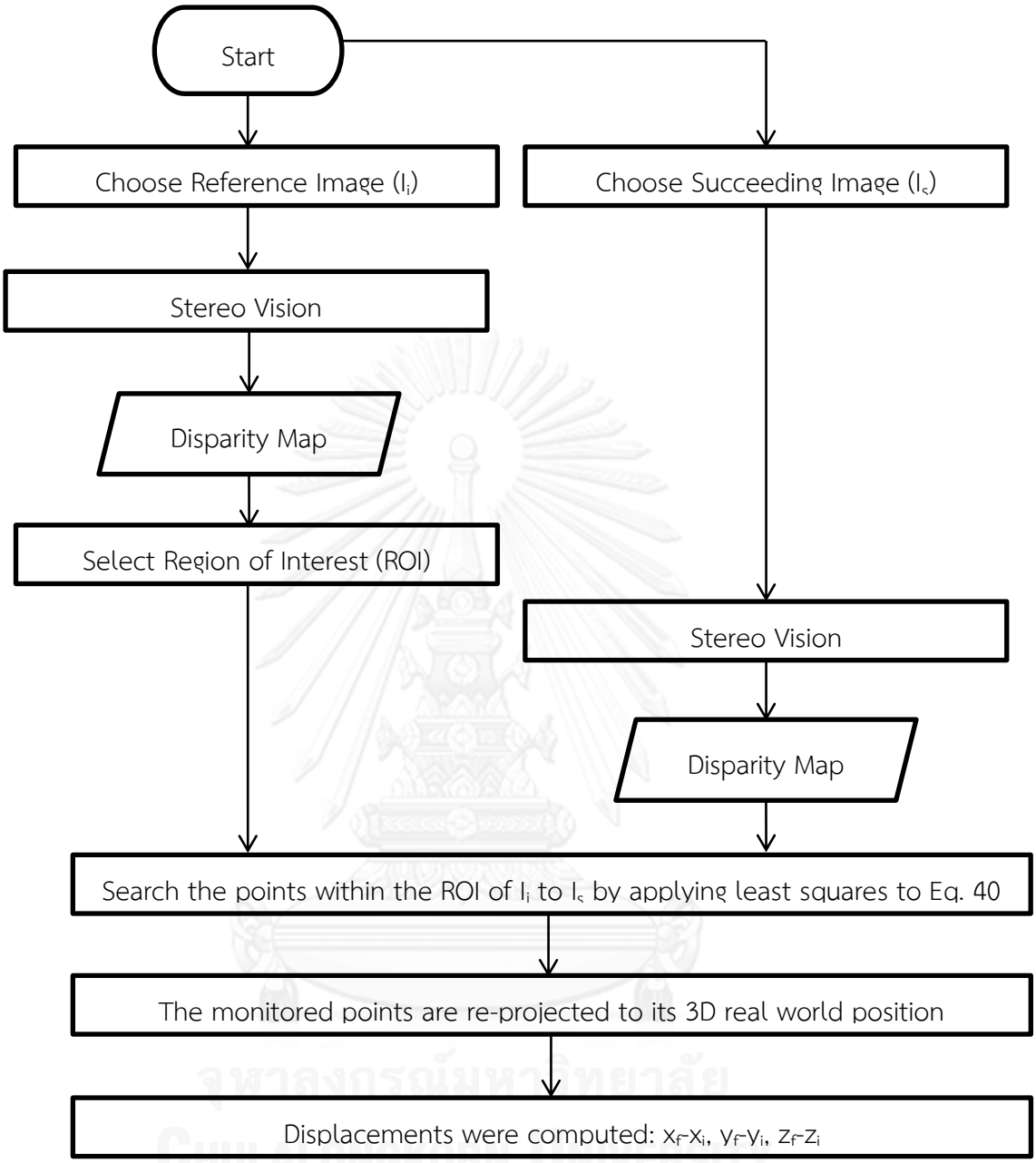

Figure 3.4.1 Flowchart for Lucas and Kanade pyramidal optical flow algorithm with stereo vision

CHAPTER 4

4 Results and Discussion

4.1 Binocular Stereo Vision Settings and Hardware

Two Canon EOS 650D cameras with 18-55mm f/3.5-5.6 IS II Kit Lenses were used. Initially, the cameras were mounted on tripods but they were not stable enough. Therefore, they were mounted on a 30cm stereo rig which was fixed on the wall as seen in Figure 4.1.1. After calibration, it was determined that the cameras must be placed at a distance of 113cm from the triaxial cell. A focal length of 55mm was used to have a better view of the object as it is being tested. An image resolution of 1920x1280 pixels was implemented since it can capture the whole object with less distortion. A baseline of 20cm was adopted based on the value of depth resolution, which will be discussed in the succeeding section.

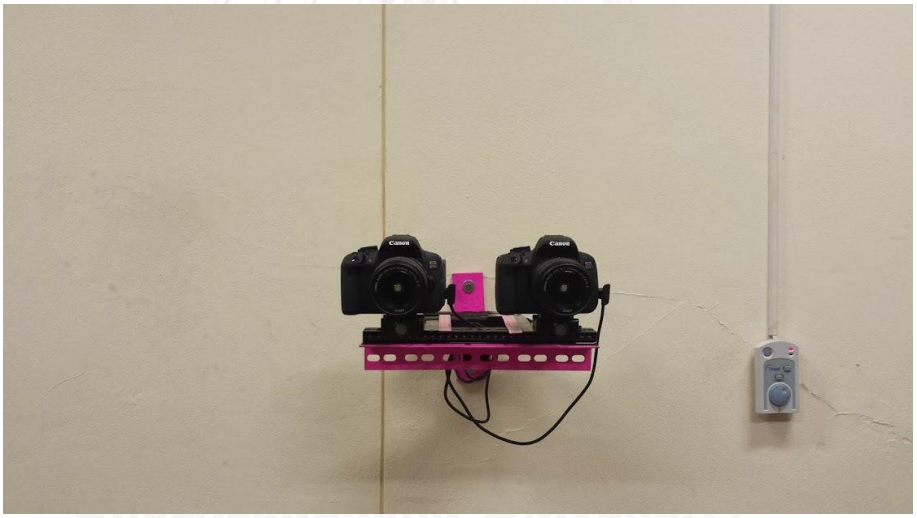

Figure 4.1.1 Camera configuration

It was also essential to modify the room for a better control of light condition. Glass windows were covered with thick dark papers and two lamps were placed close to the triaxial apparatus to maintain the intensity of light during testing. A board covered with black paper was also placed behind the triaxial apparatus to control the light as well.

4.2 Calibration

First, 2D camera calibration was performed. The rotation of the calibration grid can be seen in Figure 4.2.2 and 4.2.3. A calibrated image can be considered as an improved version of the first image. In other words, the first image of the calibration has a large effect on the calibrated results. For instance, if the first image is not in a good condition or has insufficient amount of points. The internal parameters and distortion model of each camera in this study are tabulated in Table 4.2.1. The error statistics are also presented in Table 4.2.2. If the result of the percent distortion is greater than 1 then the calibration must be repeated. From the 2D camera calibration the camera matrix M for both cameras were obtained as shown in Equation 86 and 87. The external parameters will be presented in the stereo vision calibration results.

The second stage of calibration was for the magnification error. The results are plotted as shown in Figure 4.2.1 and fitted with linear trend lines. The slope of the graph served as the magnification factor. It can be seen from the tabulated results in Table 4.2.3 that the right camera's measurement were larger that the left. However, the average magnification factor of the two cameras which was 0.89 was used to correct readings on the later stages. This parameter was used to correct the magnification from the triaxial cell.

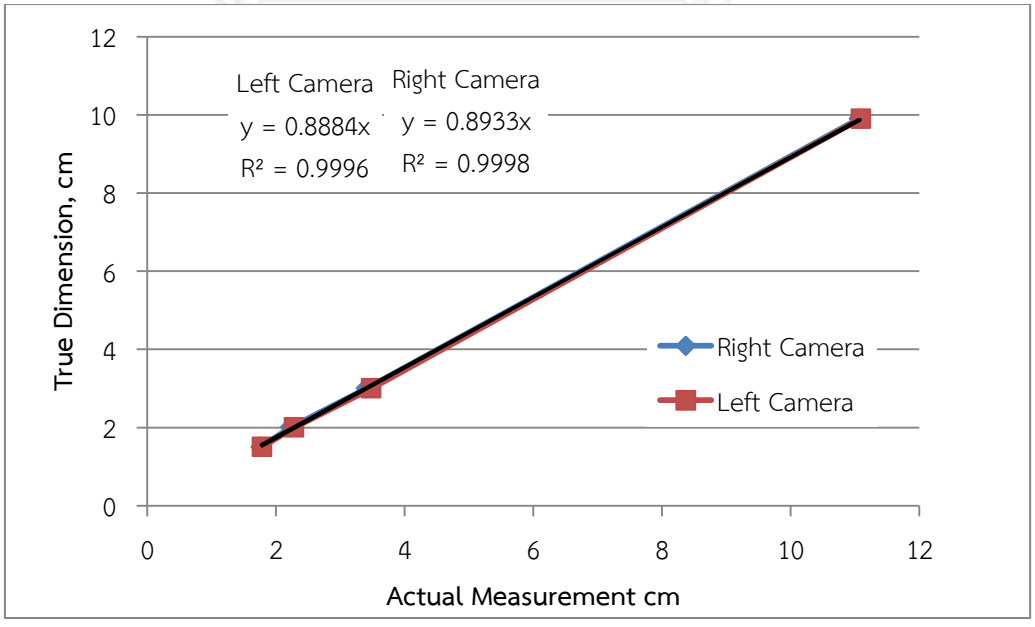

Figure 4.2.1 Plot of the calibration curve

Table 4.2.1 Internal camera parameters and distortion model coefficients of a 2D camera calibration

Camera Internal Parameters	Left Camera	Right Camera
Derivative focal Length (pixel)		
Fx	4337.51	4349.15
Fy	4293.41	4306.93
Optical Center (pixel)		
Cx	839.62	920.98
Cy	684.13	571.32
Distortion Model	Polynomial Model	Polynomial Model
Radial Coefficients (pixel)		
k1	0.2809	0.2038
k2	-4.0687	-7.3996
k3	22.7857	72.7457
Tangential Coefficients (pixel)		
p1	0.0041	-0.0065
p2	-0.0087	-0.00464

Table 4.2.2 Error Statistics for a 2D camera calibration

Error Statistics	Left Camera	Right Camera
Mean Error (pixel)	0.0228	0.0189
Maximum Error (pixel)	0.0307	0.0233
Standard Deviation (pixel)	0.0020	0.0009
% Distortion	0.1641	0.1934

Table 4.2.3 Results in determining the magnification factor

True Dimension (cm)	Left Measurement (cm)	Right Measurement (cm)
1.5	1.76	1.78
2	2.22	2.28
3	3.4	3.48
9.9	11.06	11.09
	y=0.8933x	y=0.8884x
Average	0.89	

$$\mathrm{M_{left}} = \begin{bmatrix} 0.0201 & -0.0003 & -20.7419 \\ 0.00031 & 0.0205 & -5.5341 \\ 9.9724\mathrm{e}-6 & -6.4960\mathrm{e}-5 & 1.0062 \end{bmatrix} \quad (86)$$

$$\mathrm{M_{right}} = \begin{bmatrix} 0.0202 & -0.0014 & -1.3995 \\ 0.0003 & 0.0206 & -5.3479 \\ 4.4953\mathrm{e}-6 & -5.8091\mathrm{e}-5 & 1.0146 \end{bmatrix} \quad (87)$$

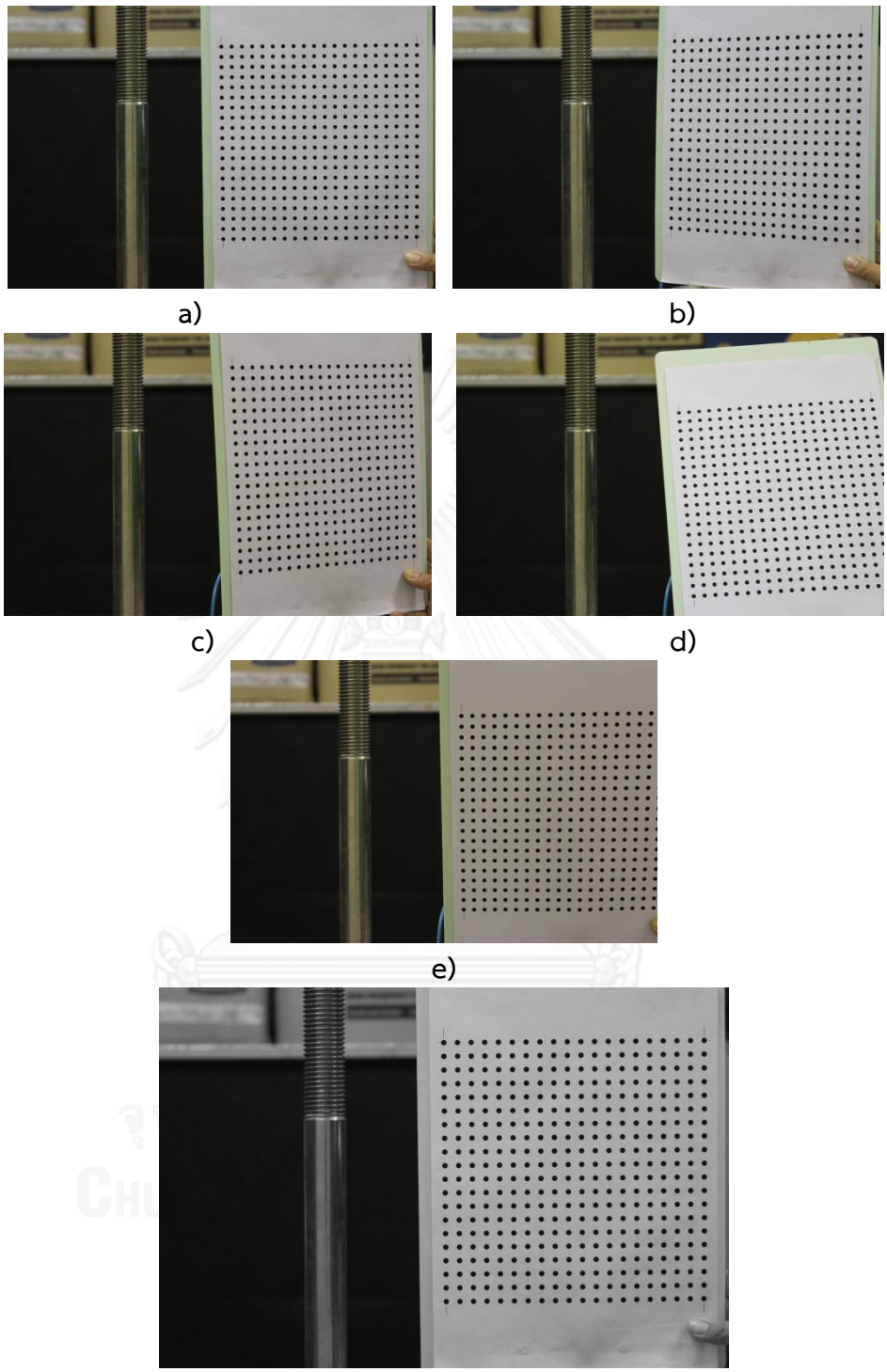

a) b) c) d) e) f)

Figure 4.2.2 Left view of the calibration grid panel a) to e) raw file f) result of calibration

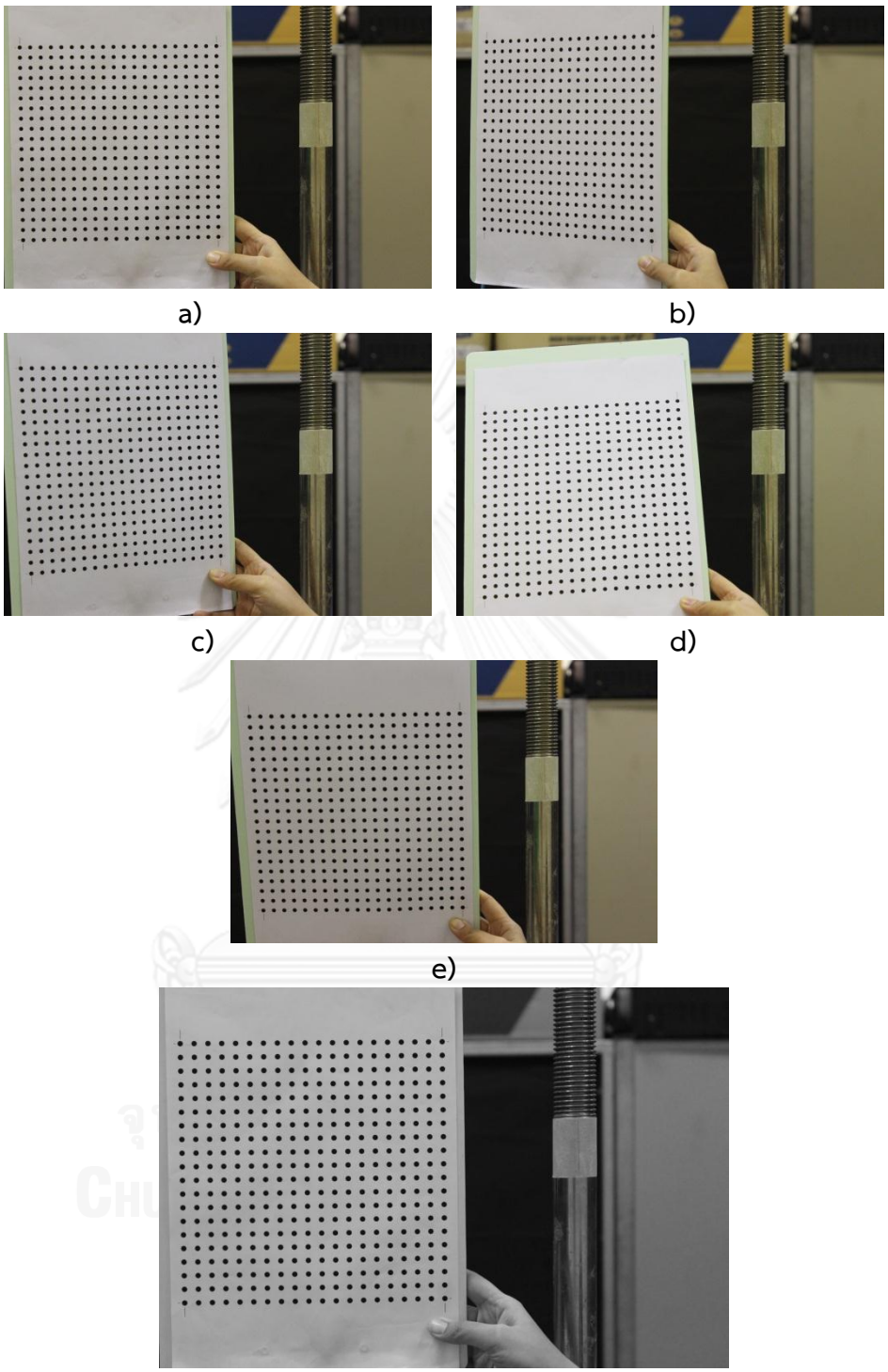

Figure 4.2.3 Right view of the calibration grid panel a) to e) raw file f) result of calibration

4.3 Binocular Stereo Vision System

After the calibration has been performed the results from both cameras were loaded to the stereo vision program where stereo calibration, stereo rectification, stereo correspondence and re-projection were carried out.

The error statistics of the stereo calibration are presented in Table 4.3.1. From the results, the calibration quality, maximum rectification error and rectification quality are all within the limits discussed in Section 3.3.1. Parameters needed for stereo rectification and re-projection which was obtained from the calibration is presented in Equation 88 to 92. The results from the rectification using these parameters are shown in Figure 4.3.1. Cameras were installed in a frontal parallel manner. Based on the results, there was not much difference between original and rectified images. For a different configuration, a result similar to Figure 4.3.2 would be obtained.

Table 4.3.1 Error statistics for the stereo calibration

Error Statistics	Result
Maximum Projection Error	1.98
Calibration Quality	0.83
Maximum Rectification Error	1.45
Rectification Quality	0.9

$$R = \begin{bmatrix} 0.9998 & 0.0028 & -0.0171 \\ -0.0023 & 0.9996 & 0.0272 \\ 0.0172 & -0.0272 & 0.9995 \end{bmatrix} \quad (88)$$

$$T = \begin{bmatrix} -19.2149 & 0.0161 & 0.2515 \end{bmatrix} \quad (89)$$

$$F = \begin{bmatrix} -4.5931e\text{-}11 & 1.3488e\text{-}8 & -1.1322e\text{-}5 \\ -3.1118e\text{-}8 & 2.8211e\text{-}8 & -0.0045 \\ 1.1156e\text{-}5 & 0.0044 & 0.0214 \end{bmatrix} \quad (90)$$

$$E = \begin{bmatrix} -0.0009 & 0.2519 & -0.0093 \\ -0.5813 & 0.5217 & -19.2007 \\ -0.0289 & 19.2078 & 0.5229 \end{bmatrix} \quad (91)$$

$$Q = \begin{bmatrix} 1 & 0 & 0 & -970.6982 \\ 0 & 1 & 0 & -627.7637 \\ 0 & 0 & 0 & 4393.0434 \\ 0 & 0 & 0.0520 & 0.3748 \end{bmatrix} \quad (92)$$

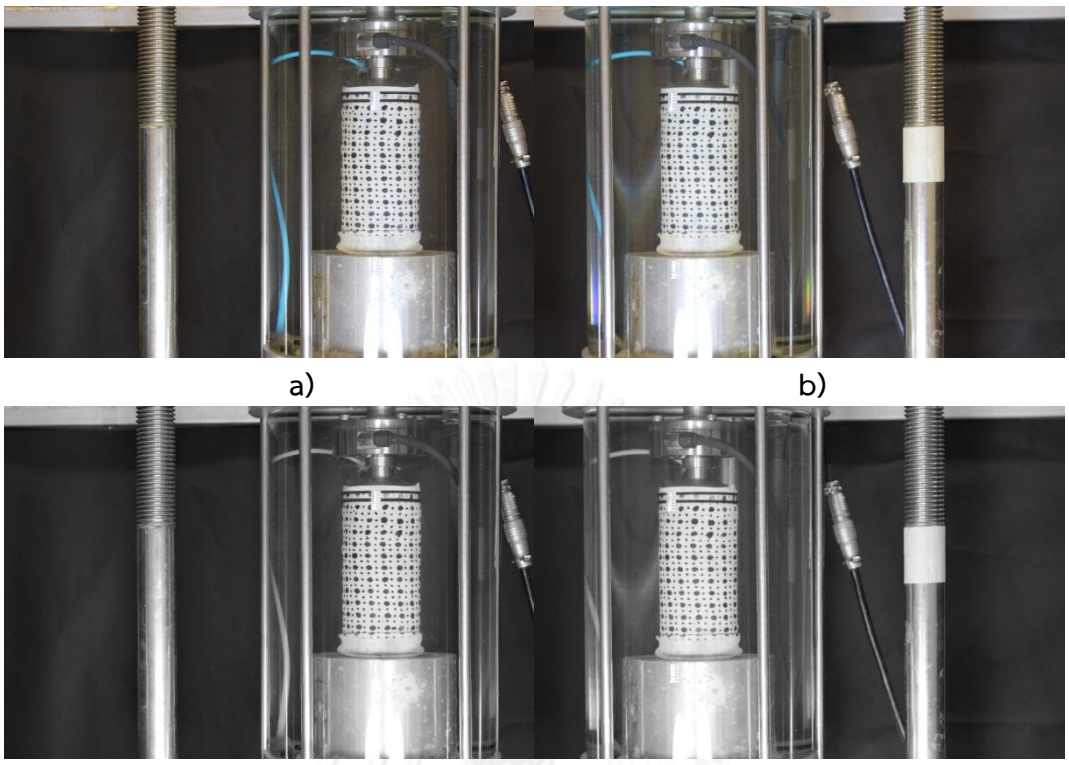

a) b)

c) d)

Figure 4.3.1 Raw images a) left view b) right view and rectified images c) left image d) right image

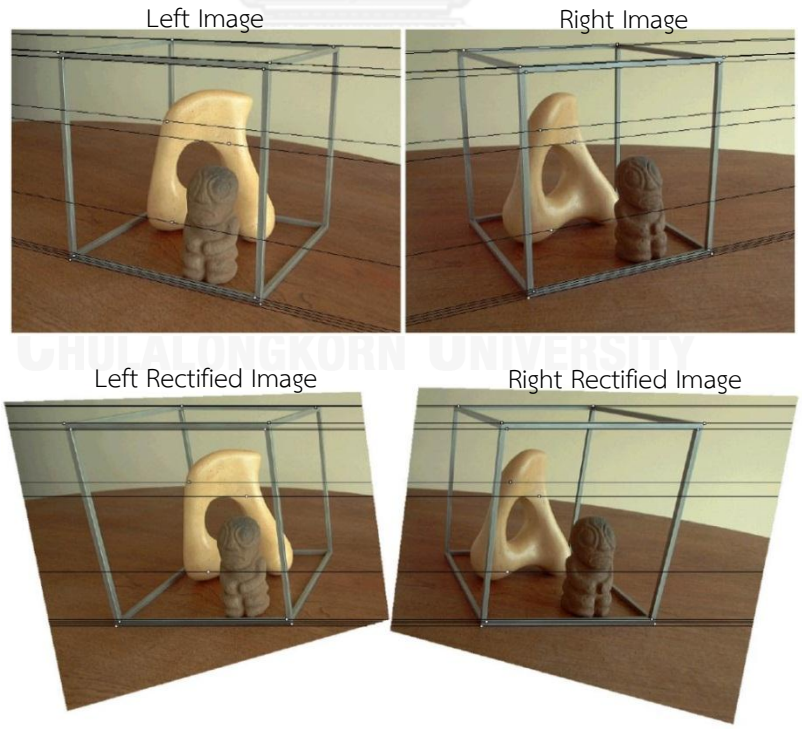

Figure 4.3.2 Sample result of a raw image that gone through the process of stereo rectification change (Hornáček, 2013)

Figure 4.3.3.a shows a disparity image obtained from the stereo correspondence. With a starting search depth of 100 cm, the blank parts of the image are areas where correspondence between the two images cannot be established. It can be seen in the disparity image that only the silhouette of the left most edge of the sample can be visibly mapped. Looking into its disparity map and depth map a bizarre pattern was observed. For the disparity and depth map the pink color represents points having small values while the black color denotes large values. On the other hand, the green or blue colors represent intermediate values. Ideally a gradual change in color of the disparity map was expected. However, it did not happen when the stereo correspondence was performed. This greatly affected the depth map as shown in Figure 4.3.3.c.

These errors were caused by an inconsistent light condition. From Figure 4.3.4, it can be seen that a cable casted a shadow on some parts of the sample. This error led to a modification on the testing room. All windows were covered with black paper to block the light from outside. Moreover, two lamps were placed close to the triaxial apparatus to maintain a constant light condition. After the modification, large improvement was observed from the disparity and depth map as shown in Figure 4.3.5. The disparity values can be obtained for almost all parts of the sample. Nonetheless, there were still some dark spots, especially from the gaps between dots on the membrane. The gradation of the disparity map became more gradual.

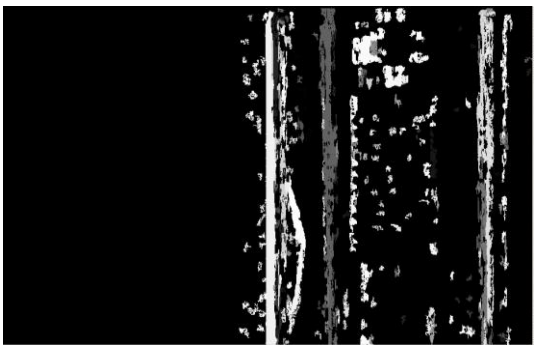

a)

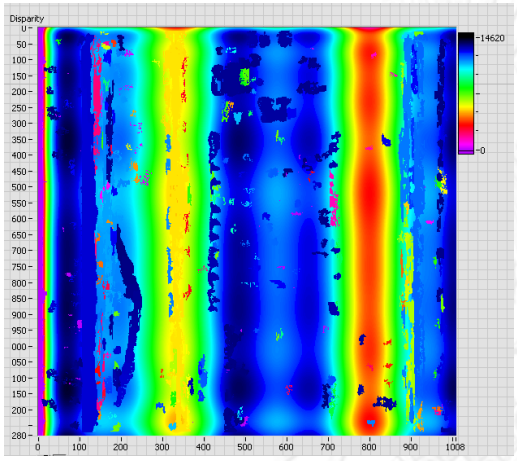

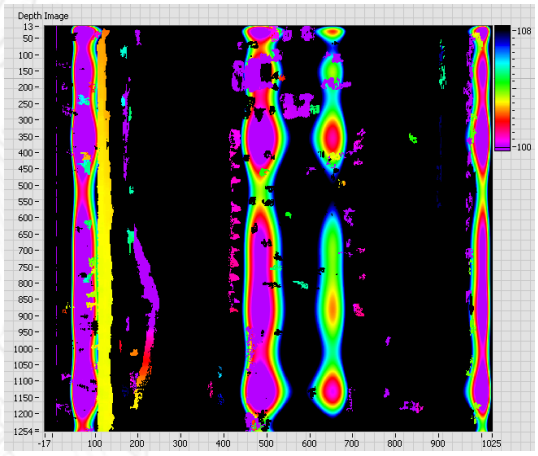

b) c)

Figure 4.3.3 Trial 1 of stereo correspondence a) disparity image b) disparity map c) depth map

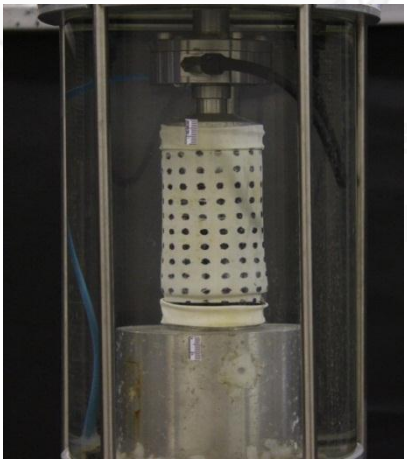

Figure 4.3.4 Image of the sample having a shadow of the load cell cable.

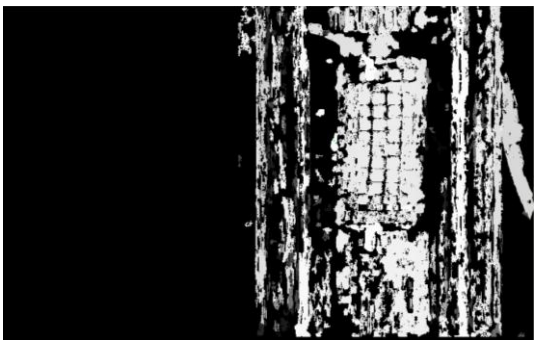

a)

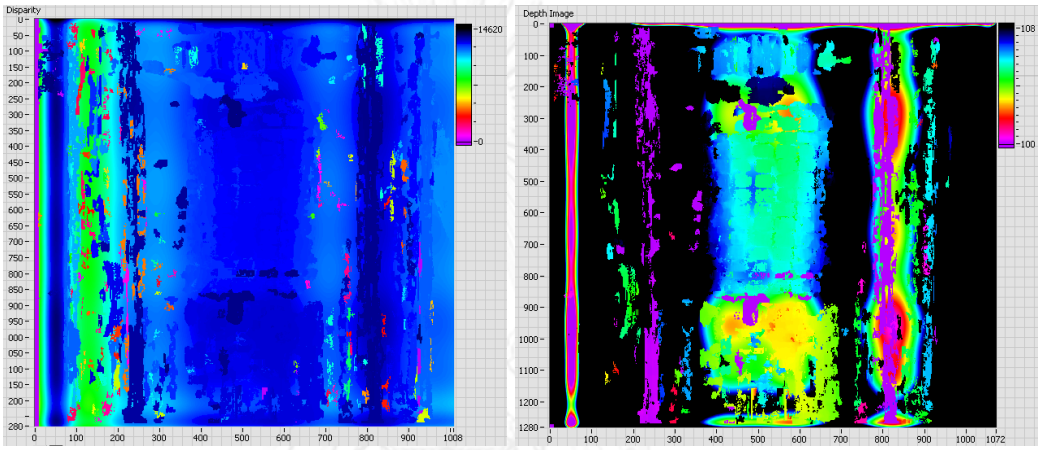

b) c)

Figure 4.3.5 Trial 2 of stereo correspondence a) disparity image b) disparity map c) depth map

To further improve the quality of the correspondence search a denser pattern was marked on the membrane as shown in Figure 4.3.6. A better disparity image was obtained compared to the previous results. The disparity map showed a good gradation of colors. A good color distribution was also observed for the depth map. A smaller amount of dark spots were observed in both the disparity image and depth map. The remaining erroneous data were then corrected by the bilinear interpolation.

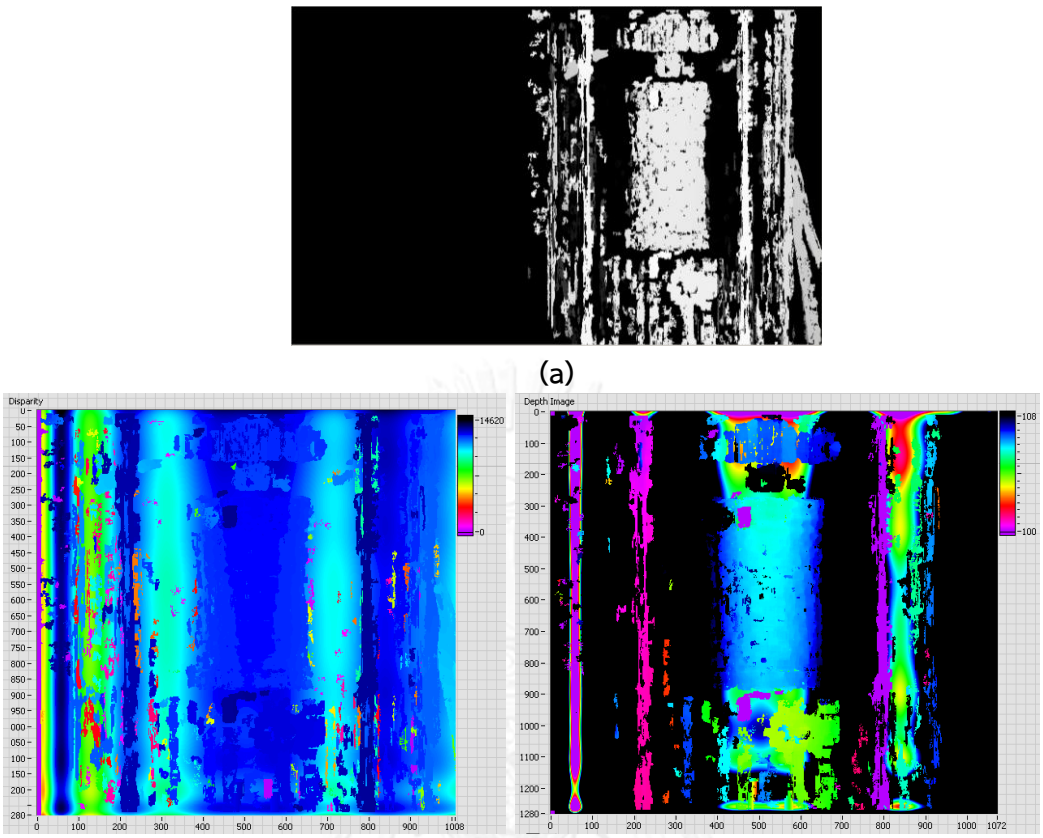

Figure 4.3.6 Trial 3 of stereo correspondence (a) disparity image (b) disparity map (c) depth map

4.3.1 Prototype Capacity and Limitations

4.3.1.1 Validation for Depth Reading

Presented in Table 4.3.2 are validations of test results of the binocular stereo vision system. The percentage error ranges between 1.98 to 15.05% for the 0.05 cm movement, 0 to 8.61% for the 0.1 cm movement, 0.50 to 5.13% for the 0.2 cm movement, 0 to 2.53% for the 0.4 cm movement, 0.17 to 1.65% for the 0.6 cm movement and 0.12 to 2.35% for the 0.8 cm movement. The coefficient of variation of the system was found to be around 0.006381 to 0.078066. The repeatability and accuracy of the system was determined from the standard deviation and it was found to be 0.006 cm and 0.004 cm, respectively.

Table 4.3.2 Results in determining the accuracy resolution (unit in cm)

Physical movement (cm)	0.05	0.1	0.2	0.4	0.6	0.8
Calculated reading	0.051	0.108	0.19	0.41	0.609	0.805
	0.043	0.1	0.204	0.399	0.606	0.819
	0.051	0.094	0.197	0.404	0.602	0.802
	0.044	0.1	0.19	0.404	0.603	0.799
	0.044	0.109	0.198	0.397	0.599	0.803
	0.051	0.095	0.199	0.399	0.603	0.811
	0.051	0.094	0.198	0.399	0.61	0.803
	0.051	0.109	0.201	0.39	0.603	0.799
	0.051	0.095	0.208	0.4	0.598	0.801
	0.044	0.103	0.191	0.404	0.605	0.807
Standard deviation	0.003755	0.006255	0.005985	0.005337	0.003853	0.006154
Coefficient of variation	0.078066	0.062113	0.030289	0.013324	0.006381	0.007646

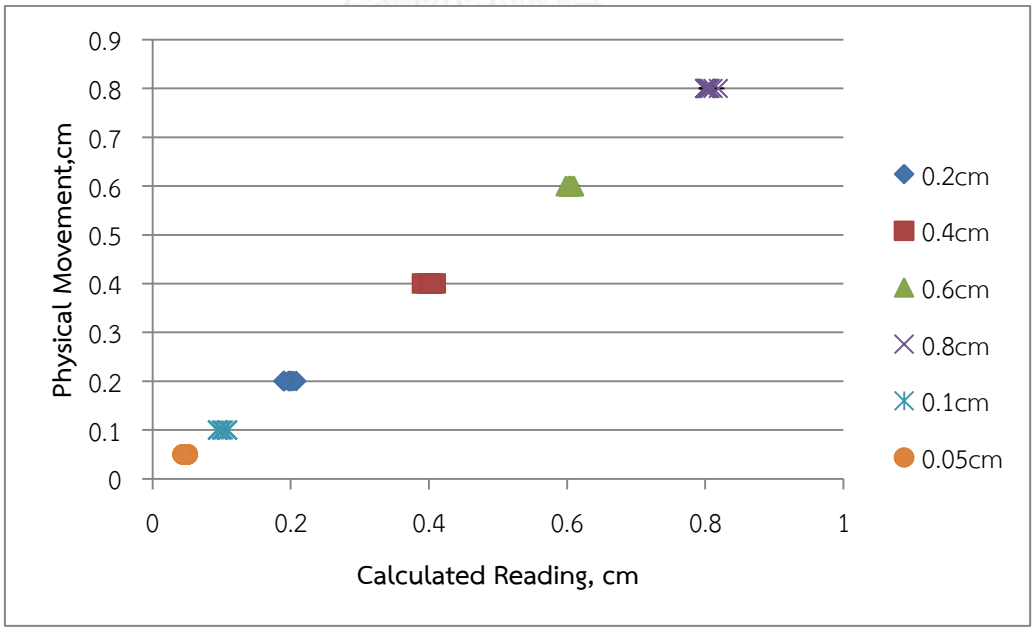

Figure 4.3.7 Plot of the physical movements versus calculated reading

4.3.1.2 Depth Resolution

Another way to check the accuracy of the system is to determine its depth resolution. Equation 61 was used to compute this parameter. The typical size of 4.3 microns or 0.0043 mm for a Canon 650D camera was used. To determine the appropriate setting, plots between the depth resolution and depth were made for focal lengths of 44 and 55 mm and for baseline distances of 16, 18, and 20 cm. It can be seen from Figure 4.3.8 that the focal length of 55 mm and the baseline of 20 cm gave the finest depth resolution. In theory, a large baseline will decrease the accuracy of stereo correspondence search. The optimum value of baseline can be deduced from the fractional overlap using Equation 62. Similar to the depth resolution, the frictional overlap depends on the focal length and baseline. When the focal length was fixed to 55 mm for the best depth resolution, the baseline of 16 cm gave the largest value as shown in Figure 4.3.9.

After computing the depth resolution and fractional overlap, a focal length of 55 mm and a baseline of 20 cm were selected as the most suitable setting for the depth resolution, even though the fractional overlap was rather small. In this regard, an effort was made to ensure that the triaxial apparatus will appear within the overlapping zone between the cameras.

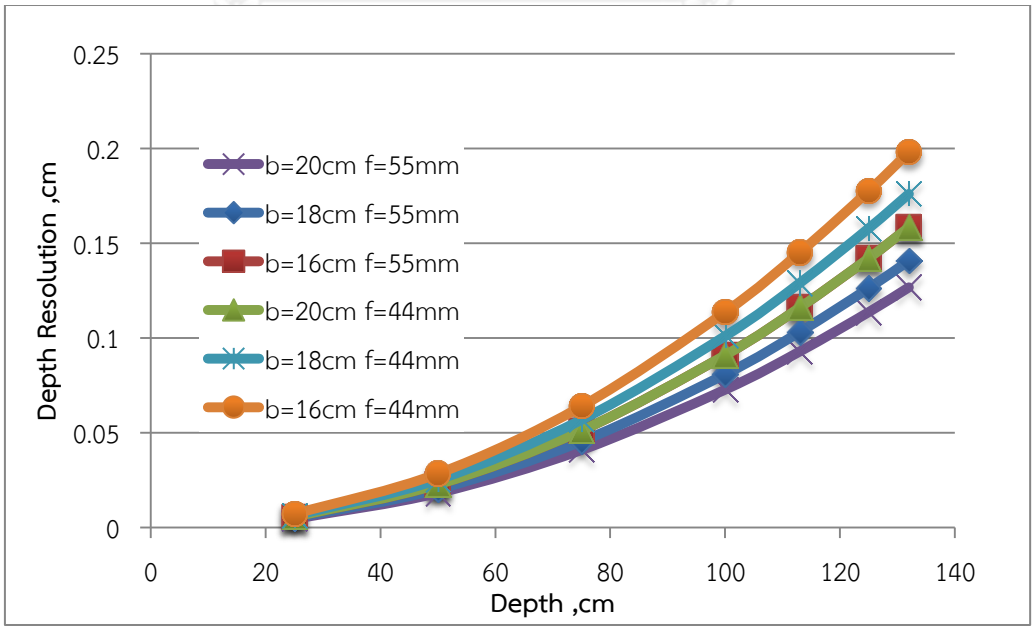

Figure 4.3.8 Depth resolution relative to object depth

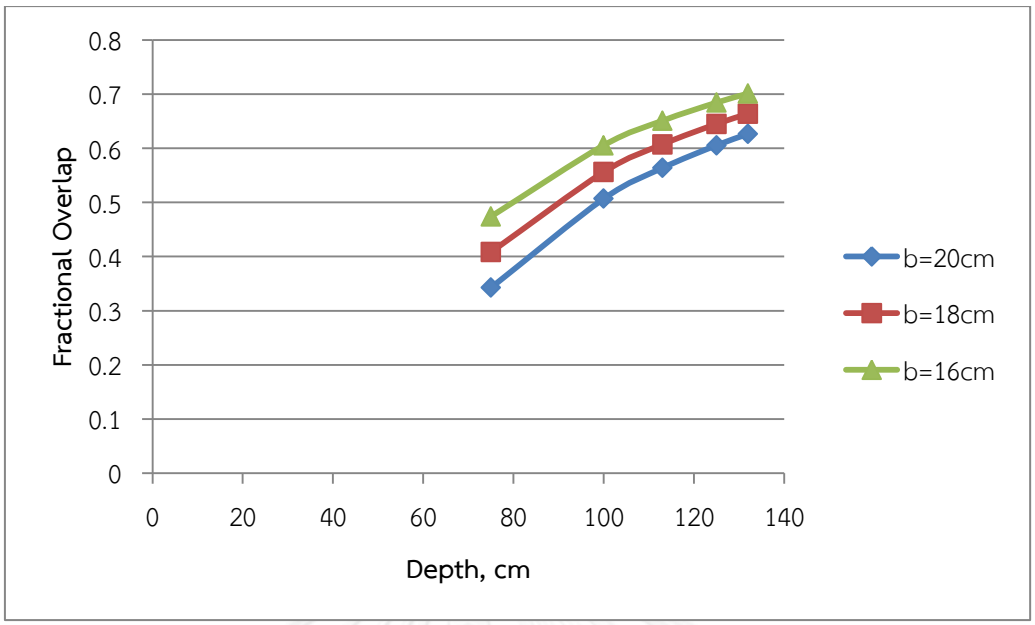

Figure 4.3.9 Fractional overlap relative to object depth

4.3.1.3 Configuration Check of the Cameras

To further check the effectiveness of the selected configuration of the cameras the equation of the depth resolution was optimized by a solver tool in Excel. The constraints for the optimization are as follows:

i. 18 mm < f < 55 mm
ii. 16 cm < T < 22 cm
iii. $\Delta z < 0.13$
iv. Fractional overlap ≥ 0.5

The first constraint was the capacity of the lens of the Canon 650D's kit lens, which can vary the focal length from 18 mm to 55 mm. The second constraint was the adjustable range of the stereo rig. The third constraint was the maximum depth resolution of the stereo vision system and it was computed from the maximum readable depth of 131 cm. The fourth constraint was the fractional overlap of the target starting readable depth of 100 cm.

The goal of this optimization is to check if the focal length and baseline were appropriate with respect to the distance between the cameras and the triaxial apparatus. The constant variables considered during the optimization are as follows:

i. Distance of the camera towards the triaxial apparatus, Z = 113 cm
ii. Smallest disparity value, Δd = 0.0043/5 = 0.00086
iii. Camera sensor size (22.3x14.9mm for Canon 650d), D = 22.3 mm

From the optimization, when the depth resolution was minimized a focal length of 55 mm and a baseline of 22 cm were obtained. From this a limit of the system can be established. A baseline distance not exceeding 22 cm and focal length of 55 mm must be implemented. The focal length and baseline of the system were within the limits established.

4.3.1.4 Camera Coverage

In this section, the range that satisfactory measurements can be obtained is determined. For a cylindrical specimen, the range can be defined by the width of measurable sector between (θ) as shown in Figure 4.3.10. This parameter has a relationship with the distance cameras and the sample, the field of view of cameras and the baseline. To determine the range of θ, viewing coverage was checked for the soil sample and the sponge. The angle was obtained by measuring the width of the sample the system can view. Since the cross-section of the object is a circle, the width can be referred to as the length of the sector which it is directly proportional to the radius of the object. Results are tabulated in Table 4.3.3, it can be seen that for both samples the system was able to view almost 80% of the sample's surface. Figure 4.3.10 shows the relationship between the field of view (FOV) of the stereo vision system and the system setup. A good coverage can be achieved when the object lies within the FOV and overlapping zone of the system. The camera coverage is greatly affected by the field of view and baseline. Increasing the field of view can improve the coverage. Decreasing the baseline distance increases the overlapping zone.

Table 4.3.3 Results for the capacity of the system to view the object

	Length of Sector (cm)	Angle of the Sector (Degrees)
Soil Sample (5cm)		
	6.35	145.53
	6.32	144.92
	6.40	146.74
Sponge (6cm)		
	7.59	140.35
	7.67	141.81
	7.81	144.26

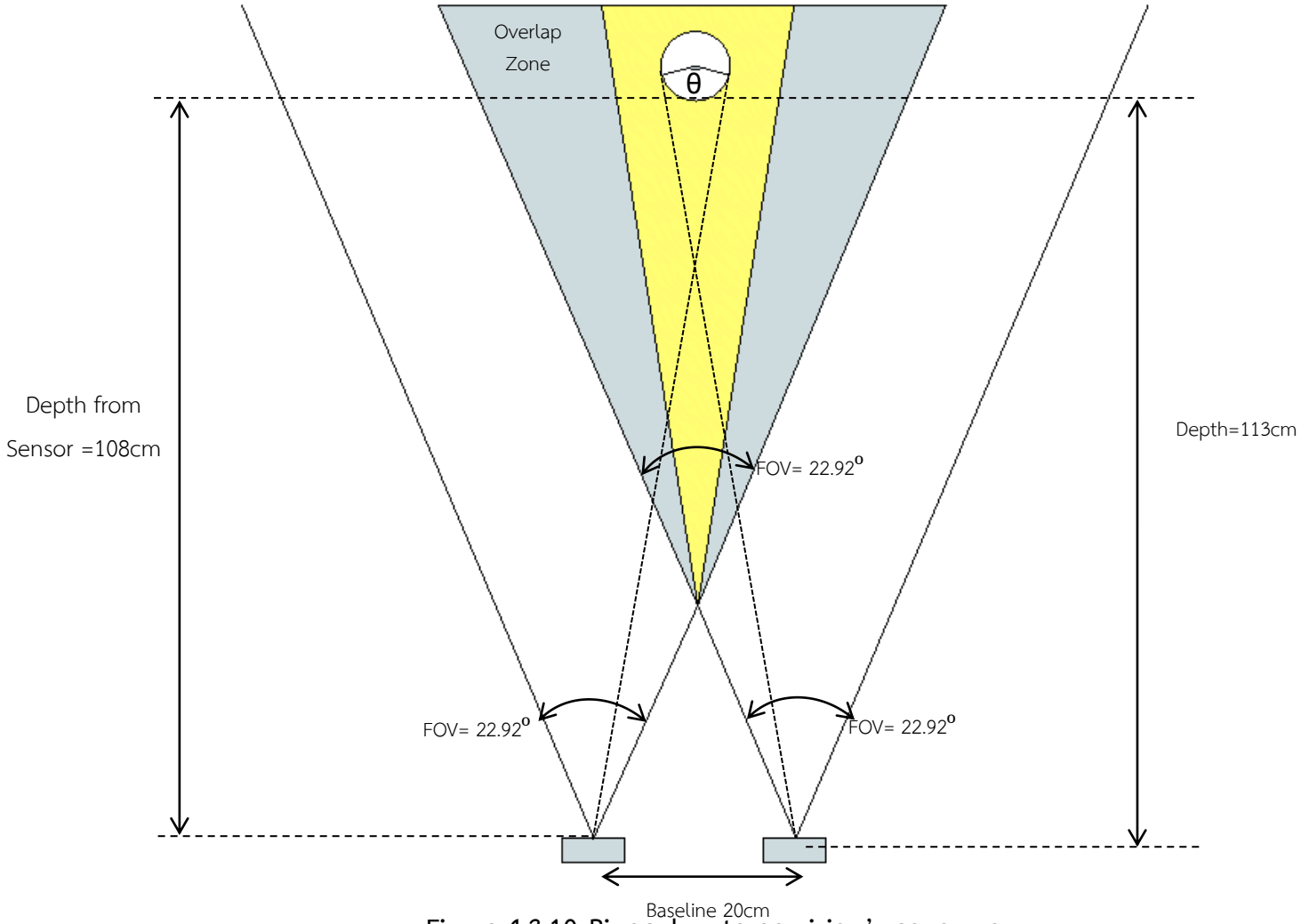

Figure 4.3.10 Binocular stereo vision's coverage

4.3.1.5 Validation for Depth Reading under Tilting Planes

The capacity of the system to read depth changes under tilting planes was determined. A comparison was made between the results of the stereo vision system and the laser transducer. As seen in the tables below the error at the center has a range of 0.39 to 0.90 mm, the error at 40° from the center has a range of 0.64 to 4.62 mm, and the error at the boundary has a range of 0.79 to 1.87 mm. Large errors were observed from the readings at 40° from the center. As seen in Figure 4.3.12, there were large fluctuations in the data. Stereo correspondence search is difficult to perform at this area since it is at the maximum camera coverage.

Table 4.3.4 Errors at the center

Trial number	Error, mm
1	0.51
2	0.39
3	0.55
4	0.47
5	0.47
6	0.58
7	0.46
8	0.40
9	0.78
10	0.90

Table 4.3.5 Errors at 40° from the center

Trial number	Error at the left side, mm	Error at the right side, mm
1	1.52	2.15
2	2.19	1.67
3	1.18	1.51
4	1.80	4.62
5	1.05	3.12
6	0.64	3.59
7	3.72	1.92
8	4.27	2.60
9	1.54	1.97
10	1.32	2.13

Table 4.3.6 Errors at the boundary

Trial number	Error at the left side, mm	Error at the right side, mm
1	1.45	0.79
2	1.20	1.85
3	1.58	1.87

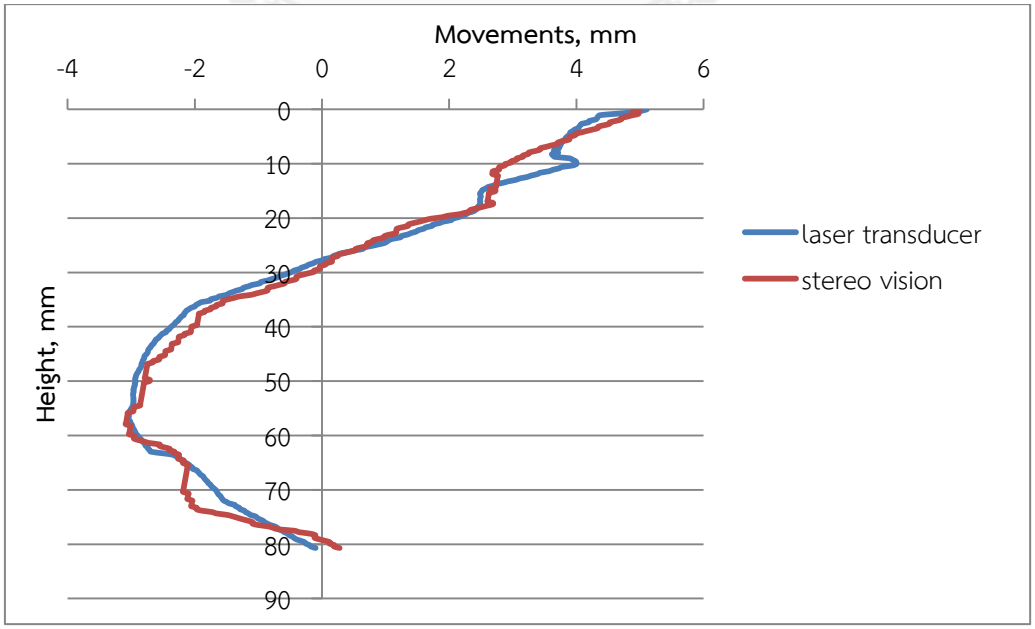

Figure 4.3.11 Profile at the center: Trial 1

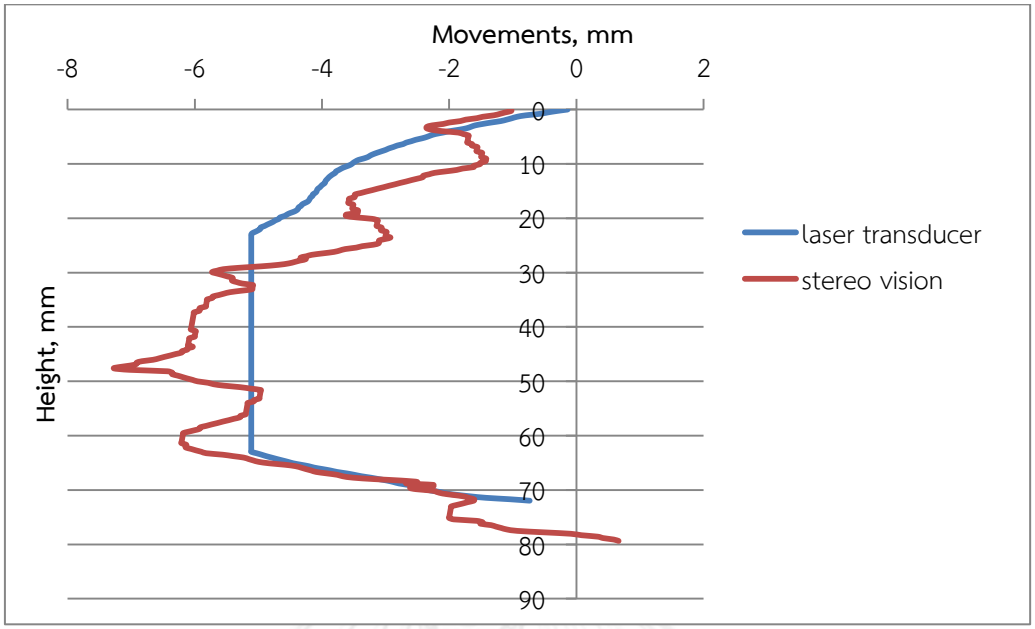

a)

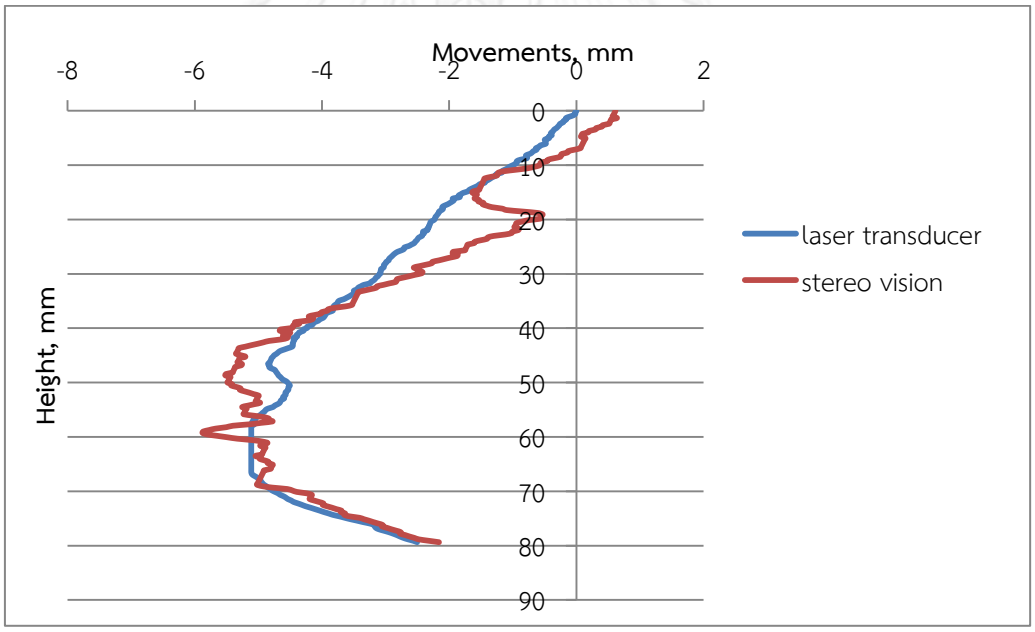

b)

Figure 4.3.12 Profile at 40° from the center: Trial 1 a) Left b) Right

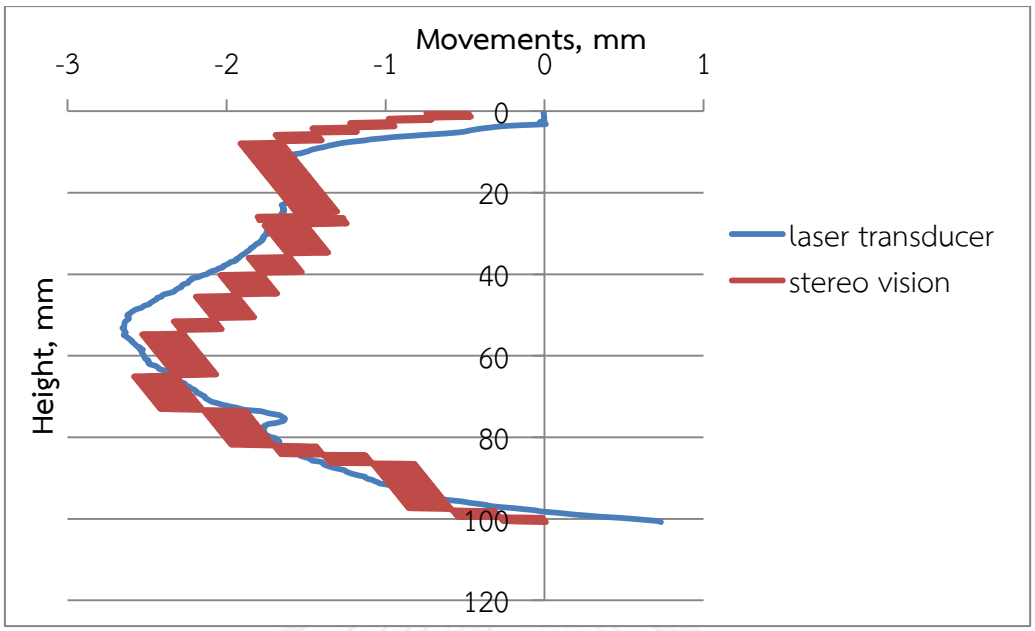

a)

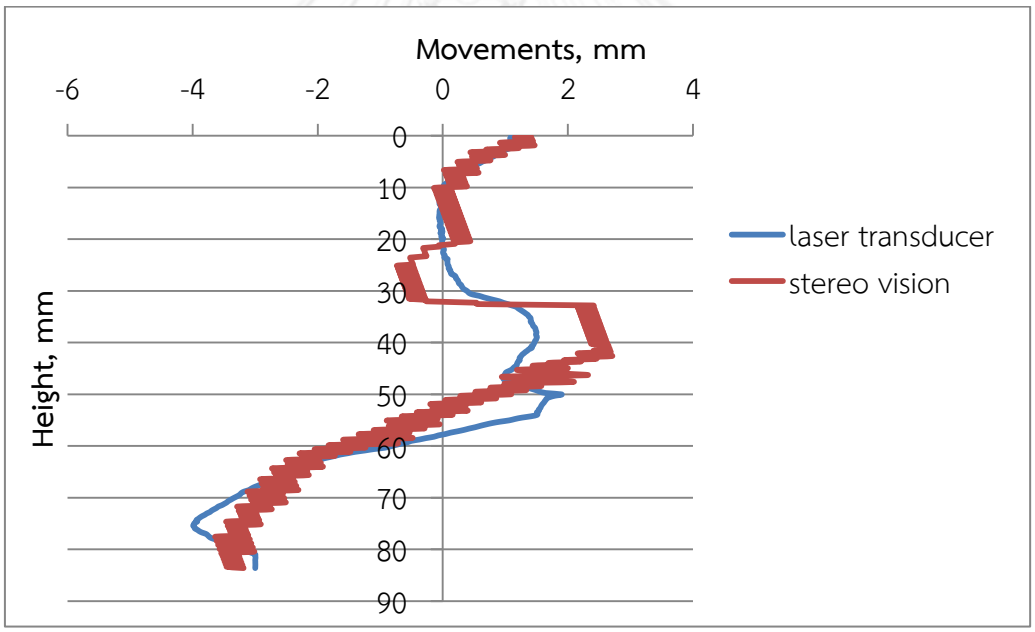

b)

Figure 4.3.13 Profile at the boundary: Trial 1 a) Left b) Right

4.4 Triaxial Testing

4.4.1 2D Image processing

At the beginning the accuracy of the 2D system was determined as discussed in Section 3.2.1. This test was made by the uniframe for an unconfined compression

test. From the test, a resolution of 0.2mm was obtained. Strains were derived from displacements obtained from image processing and compared to the readings from a strain gage. Unfortunately, a large difference was observed. A reason for this discrepancy was due to the difference in size of gage length. The strain gage measures at a single point over a gage length of 6 mm while the strain was computed over a wider distance.

After the accuracy test, two experiments were done on Bangkok Clay samples. The external and internal measurements were obtained through image processing and compared to the reading from a LVDT. The external measurement was made by selecting a region of interest at the top most part of the triaxial cell. Figure 4.4.2 presents the stress-strain curve of both tests. It can be seen that the results of both measurement techniques were well agreed. For the internal measurement, the whole region that the camera can view was tracked. A non-homogeneous deformation was observed when the sample was being sheared. Prior to the peak stage the movements of soil near the pedestal were larger than those near to the top cap. When the sample was about to fail large movements were observed locally in some areas. Figure 4.4.3, shows the internal displacement of the sample. A good fit was observed between the two results.

To further monitor the behavior of the soil the displacement field and strain field were calculated. A color magnification mapping technique was applied to determine the areas where large deformations occur. This technique was inspired from the research done at Massachusetts Institute of Technology. The pixel values were amplified to reveal hidden information within the image (Wu et al., 2012). Their technique can be referred to as Eulerian video magnification. From this, a program was developed in Labview were a color map containing amplified values was plotted and it was overlaid to the image. The color map was used as an early detection of critical zone of the soil. Three base colors in the program are red, green and blue. Red represents a large displacement while blue is for a small displacement. The program developed has a capability of showing only large disaplacements and strains by making small values transparent. The strain was computed from the change in displacement between two points dividing by the length between them. The grid size used for this computation was 1x1 pixel or 0.26x0.26 mm.

In Figure 4.4.1, the displacement history of BH2 shows that the sample tends to have a large movement at the middle in the first few days of the test. During the shearing stage, the triaxial cell was pushed from the bottom. Therefore large displacements can be observed near to the base. It can also be observed from the strain field the location where large localization occured. This trend was equivalent to a bulging mode of failure, which is normally expected for a ductile sample.

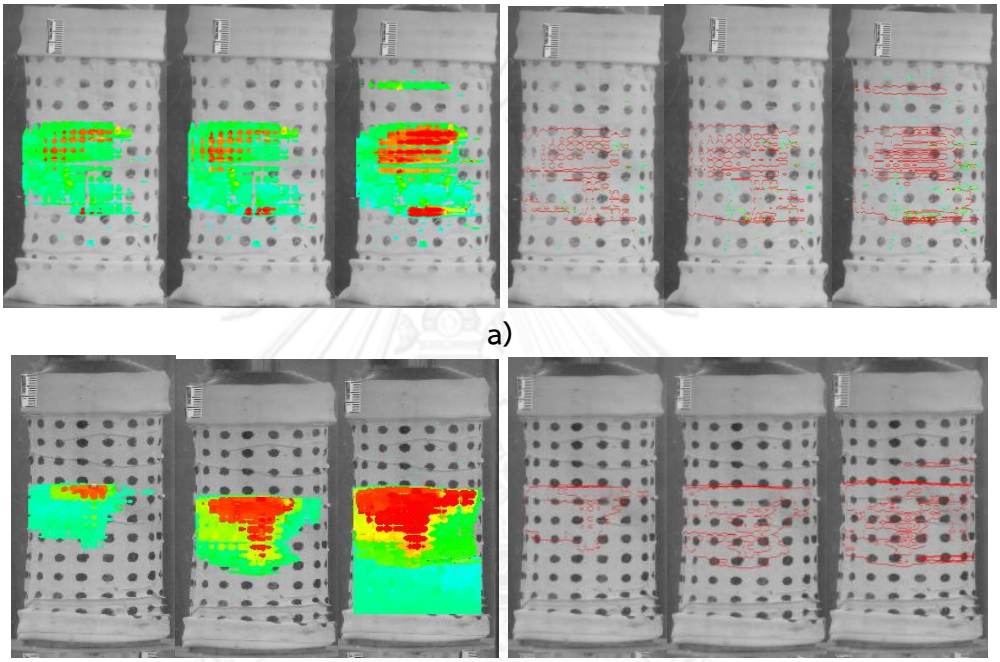

a)

b)

Figure 4.4.1 Results of displacement field and strian field from the left camera at day 1, 2 and end of the test a) BH1 b) BH2

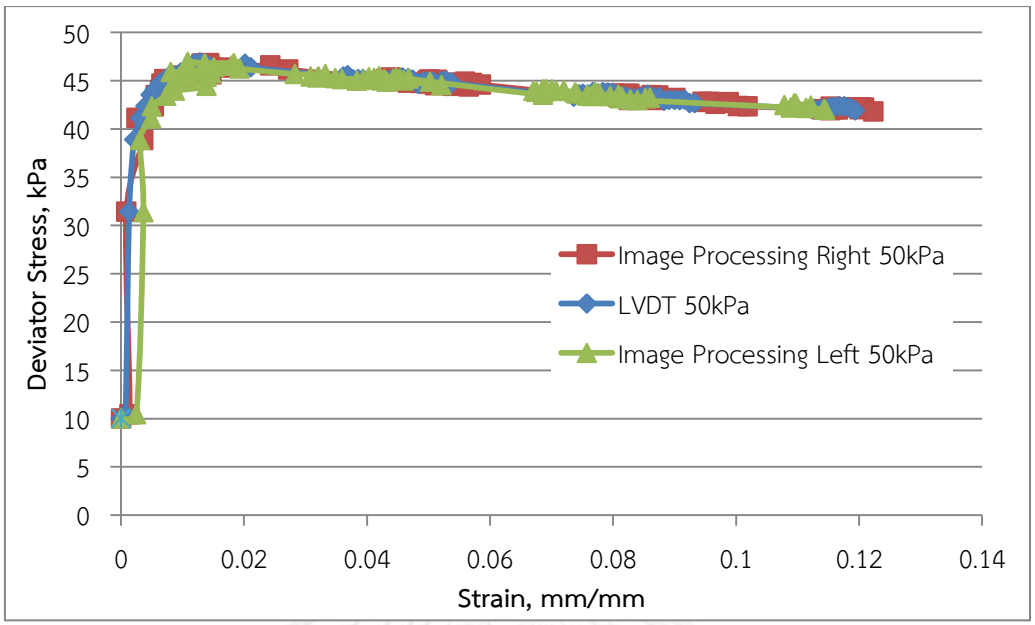

a)

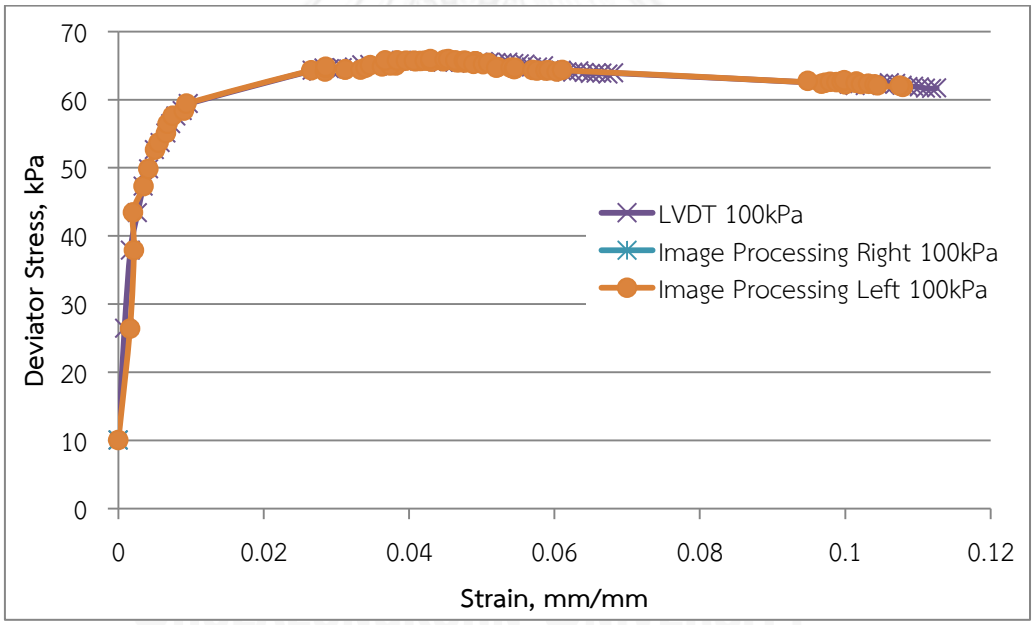

b)

Figure 4.4.2 Stress strain curve for a) BH1 b) BH2

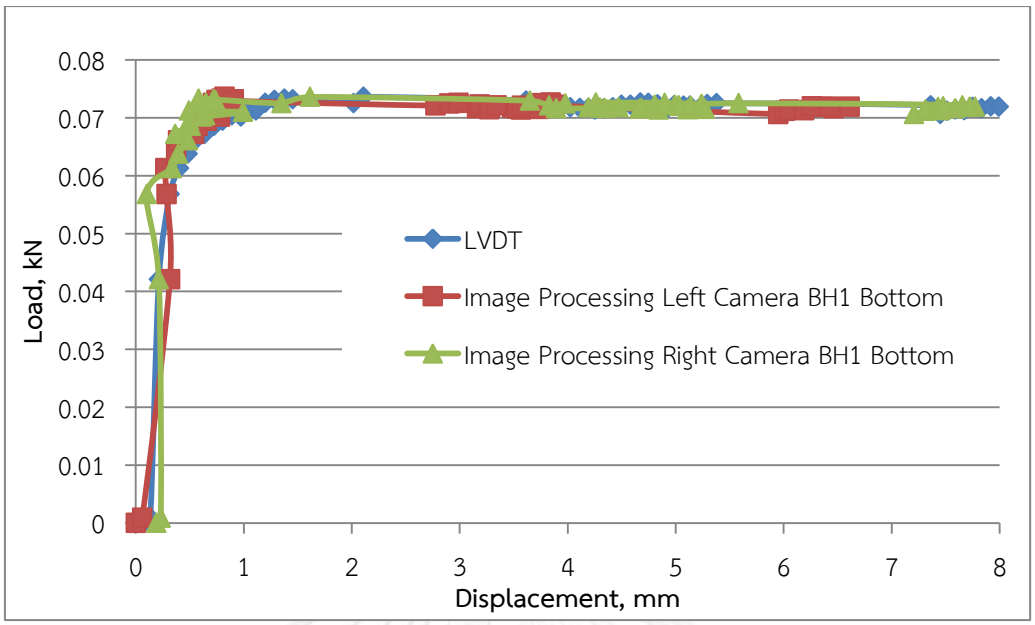

a)

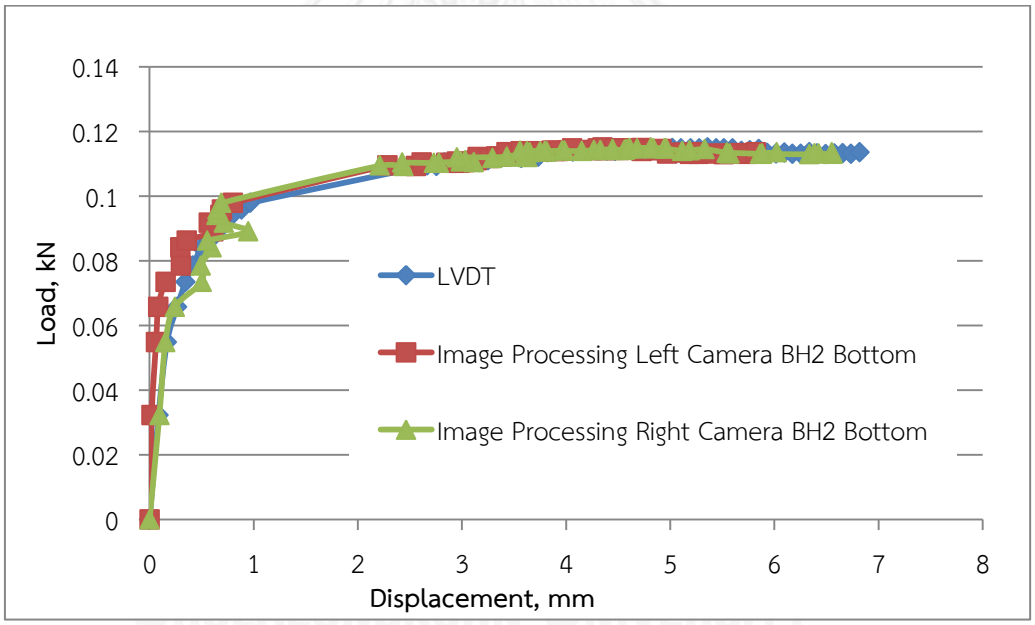

b)

Figure 4.4.3 Load vs displacement curve obtained near the pedestal of the triaxial cell (a) BH1 (b) BH2

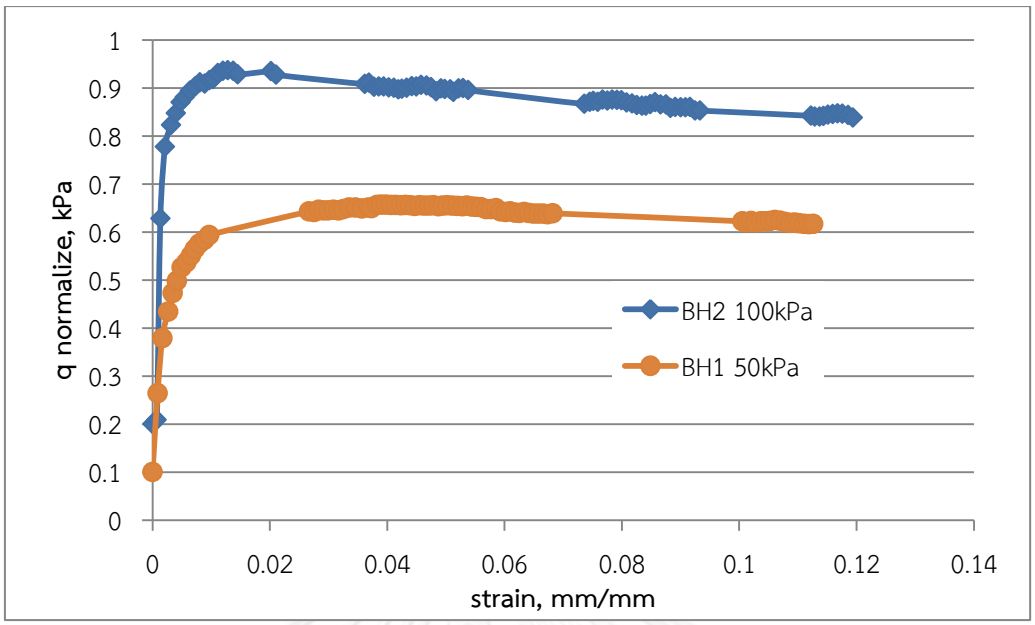

Figure 4.4.4 Normalized deviator stress vs strain

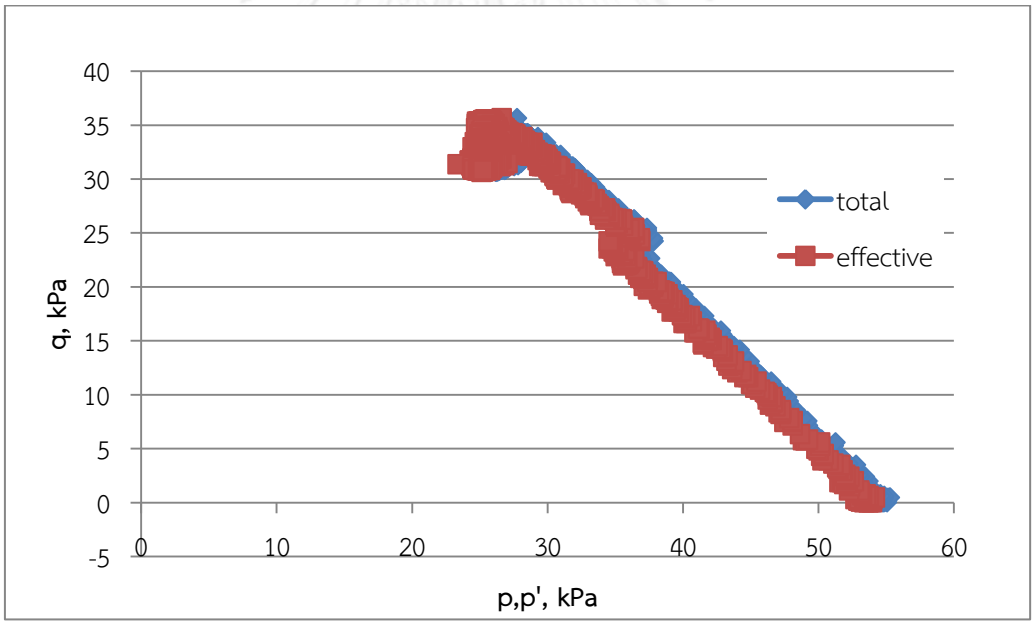

Figure 4.4.5 Stress path of BH1

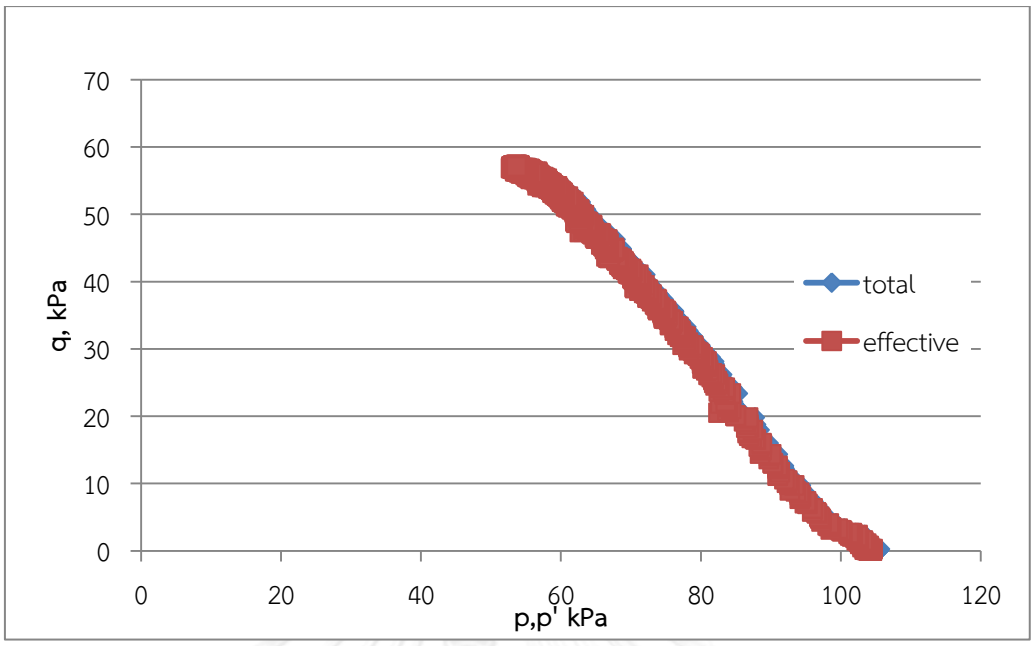

Figure 4.4.6 Stress path of BH2

4.4.2 Binocular Stereo Vision

Initially tests were planned to be done on Bangkok Clay samples but a sponge was used instead to avoid non-homogeneous mode of deformation. The use of sponge provided a better control on the flow of water. Six trials were made in determining the capacity of the system. The amount of water flowing in and out of the sponge was calculated by three different techniques.

For the first technique, the reference image was taken before the beginning of test. In this manner the cumulative volume of water can be measured. This method only worked for a certain amount of time because it became difficult to estimate movements from significantly different image pair. For the second technique, the reference image was taken right after the cell pressure and back pressure has been applied. The volume obtained from this technique is also a cumulative one. Similarly the algorithm worked over a limited period. In the third technique the change in volume between successive images was determined. Results are summarized in Tables 4.4.1 to 4.4.3. For all methods, low percentage errors in a range of 1.16% to 8.86% were observed. When the size of patch was varied to examine its influence on the calculated result, no distinct trend was observed. For the second trial, a large amount of water was introduced to the sponge to determine the ability of the system to handle large changes. Extreme amount of water was introduced to the

sponge. The volume of inflow as calculated by the second method was 43.16 cc while the measured volume was 45.88 cc and error of 6.1% was observed.

Table 4.4.1 Results of Trial 3 when the reference image was taken before the test begins

	Patch Size	Volume from Image Processing (cc)	Volume from Burette (cc)	%error
1	58	14.64	15.23	-3.97
2	58	14.75	15.20	-3.00
3	38	22.36	22.1	1.18
4	39	14.51	15.1	-3.96

Table 4.4.2 Results of Trial 3 when the reference image was the first image after the test begins

	Patch Size	Volume from Image Processing (cc)	Volume from Burette (cc)	%error
1	44	15.59	15.20	2.52
2	42	20.31	22.10	-8.42
3	39	14.97	15.10	-0.84
4	48	9.75	9.40	3.61

Table 4.4.3 Results of Trail 5 when the change of volume is obtained.

	Patch Size	Change in Volume from Image Processing (cc)	Change in Volume from Burette (cc)	%error
0-1	53	15.63	16.93	-8.03
1-2	59	30.52	30.88	-1.16
2-3	36	2.78	2.85	-2.47
3-4	23	4.11	4.04	1.55
4-5	42	9.86	10.77	-8.86
5-6	21	4.55	4.17	8.77

An area that the developed system can be applied is the real-time monitoring of soil behavior under testing. The capacity of the system was tested by shearing a soil specimen until failure. Figure 4.4.4 shows the image of the sample under test as well

as the displacement maps in out-plane and in-plane directions. For the in-plane displacement map, the negative values represent movements to the left while positive values are movements towards the right. In Figure 4.4.4.b, it can be seen that expansion is experienced close to the left bottom region and the midsection of the sample. It is represented as the purple color as shown. Contraction on the other hand also occurred which is represented as the green, yellow and black colors. The color scale of both maps was scaled based on the range of values of the data being mapped. When the color maps were counterchecked with the image of the soil sample the patterns formed were consistent with the image.

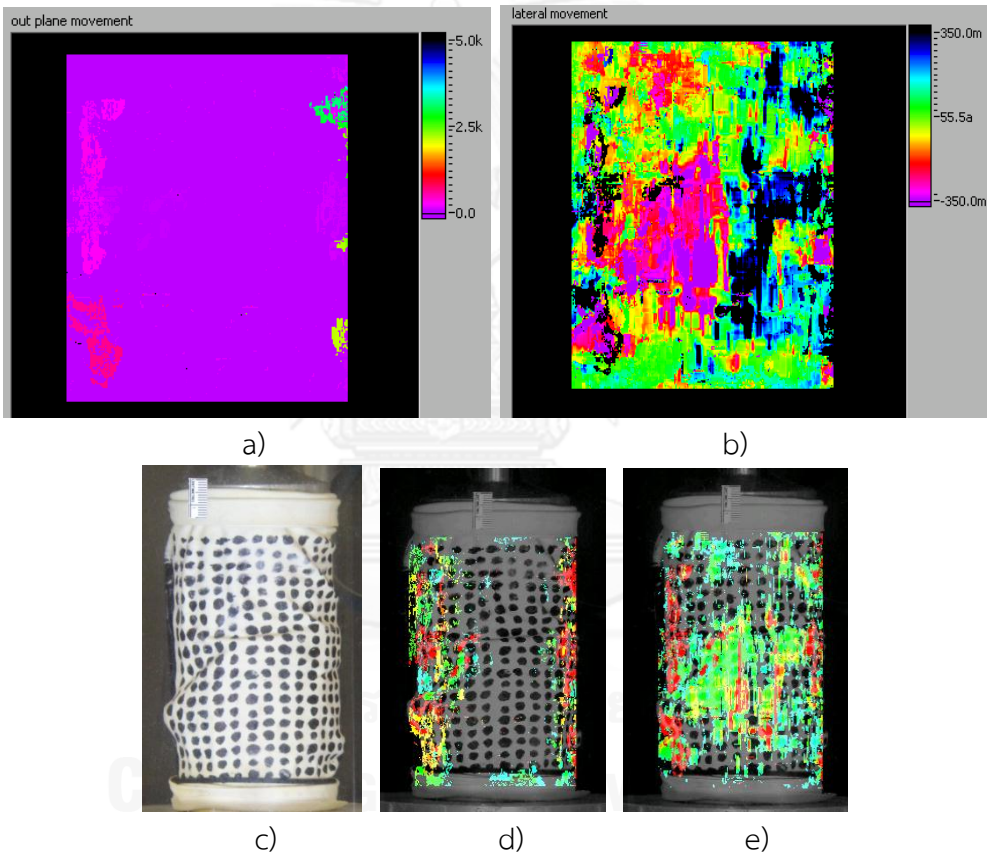

Figure 4.4.7 Displacement maps a) out-plane movement map b) lateral movement map c) image at failure d) out-plane movement map overlaid with the image at failure e) lateral movement map overlaid with the image at failure

The capacity of the system to measure at local deformations was also determined. 3 Unconsolidated undrained tests were performed using Bangkok clay. Unfortunately, only 1 trial can be analyzed because the images of the other trials

were not in good condition. An error of 1.77 to 10.14 % was observed from the results. The local deformations were measured at the midsection of the soil sample. Fluctuations were encountered when the displacements and strains were computed. To further investigate on this, displacements at the pedestal, 1/3 from the base and 2/3 from the base was obtained and compared with the result from the LVDT. From Figure 4.4.9, it can be seen that fluctuations started at a deviator stress greater than 15kPa at 2/3 from the base. To have a better understanding on what occurred during the test full-field monitoring was performed. Displacement fields are shown in Figure 4.4.9 and it can be seen that there are localizations at the area 2/3 from the base. Due to this, it is impossible to measure local deformations for this data.

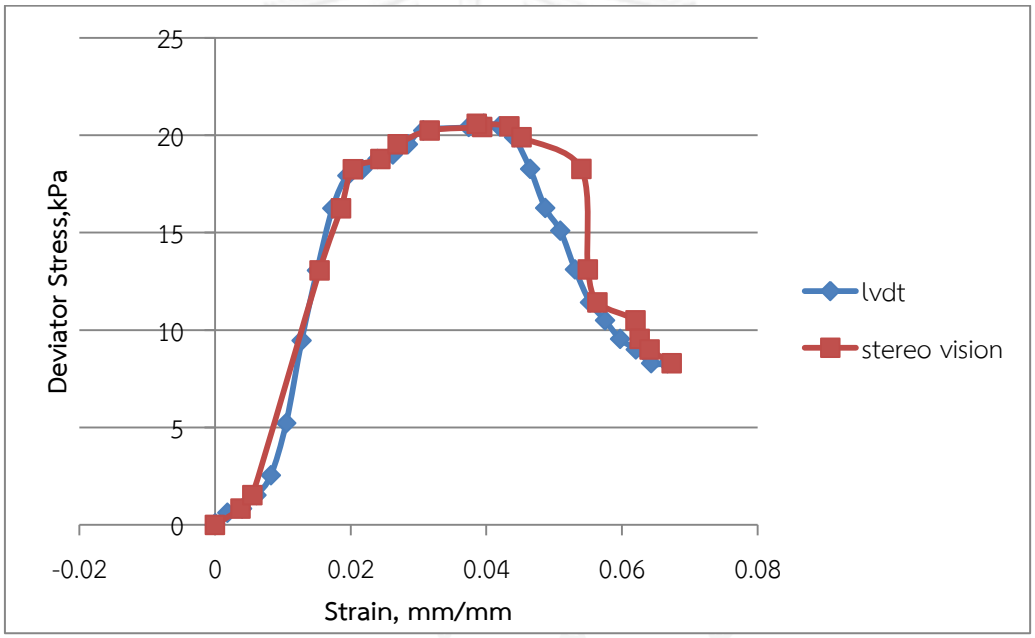

Figure 4.4.8 Stress-strain plot for Bangkok Clay

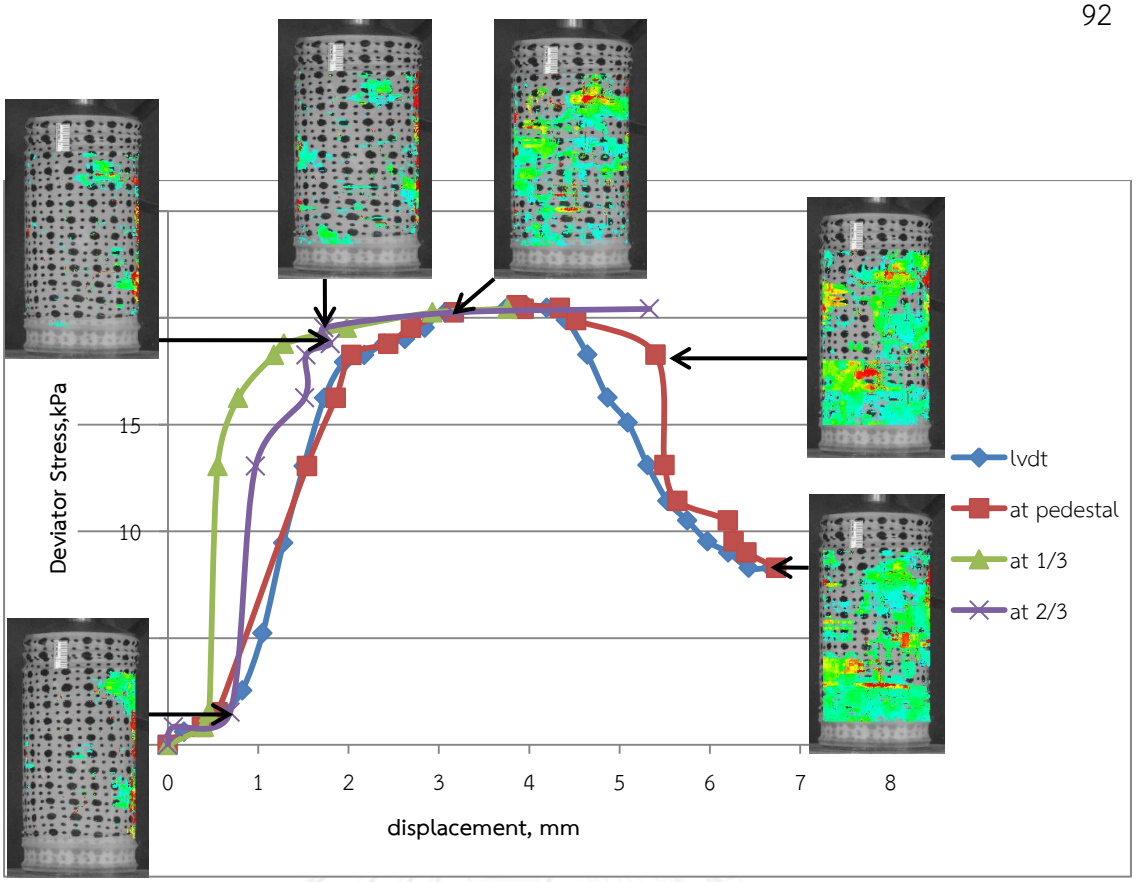

Figure 4.4.9 Stress-displacement plot for Bangkok Clay

CHAPTER 5

5 Conclusion and Recommendations

5.1 Conclusion

A non-contact measurement system was developed through the use of two Canon EOS 650D cameras with 18-55mm f/3.5-5.6 IS II Kit Lens. The software unit was implemented by Labview programming language. The prototype had the capacities to perform 2D and 3D measurements through image processing. Lukas and Kanade pyramidal optical flow algorithm was applied in both measurements to track the movement of interested points.

The 2D measuring system's resolution was 0.2 mm. When the readings from the system were compared to those from LVDT, for a consolidated drained unloading test errors ranging from 5 to 10% were observed. For the 3D measuring system, a dense pattern overlaid on the membrane can improve the quality of stereo correspondence search. It may have a random or a distinct pattern. It is also preferred that the object should be dominant within the scene. Furthermore, a uniform light condition is essential to avoid errors during the stereo correspondence search. The location and settings of the cameras were checked through the optimization of the depth resolution equation. When applied for 2 inch triaxial specimen under proposed settings, the system can measure movements on the viewable side over an angular range of 140 degrees. When measuring out of plane movements, standard deviation ranging from 0.003755 to 0.006247 cm for movements of 0.05, 0.1, 0.2, 0.4, 0.6, and 0.8 cm were obtained. From the standard deviation, the repeatability and resolution was 0.006 cm and 0.004 cm respectively. For the readings of depth at titling planes the profile from the system was compared with a laser transducer. Large differences were observed at 40° from the center at a range of 0.64 to 4.62 mm. Errors ranging from 1.16% to 8.86% were observed when computed volumes were compared with measured values. The system provides an option to compute the volume of flow between any image pair. From these, it can be concluded that the system has a good capability in obtaining 2D and 3D measurements. It can be applied in monitoring the behavior of the soil during the test such as to monitor the development of localization failures in soil. However, it is only limited to the area viewable by the cameras.

5.2 Recommendations

As a recommendation, additional cameras must be placed around the perimeter of the triaxial apparatus to increase the coverage of the system. There should be overlapping areas among the cameras. Once modified the complete behavior of the soil can be observed. Furthermore, the volume of flow cab be obtained even specimens deform in un-symmetric fashion.

REFERENCES

Acharya, T., & Tsai, P. S. (2007). *Computational foundations of image interpolation algorithms*. Paper presented at the ACM Ubiquity.

Bagga, P. J. (2013). Real Time Depth Computation using Stereo Imaging. *Journal Electrical and Electronic Engineering, 1*(2), 4.

Bradski, G., & Kaehler, A. (2008). *Learning OpenCV Computer Vision with the OpenCV Library*: O'Reilly.

Fanto, P. L. (2012). *Automatic Positioning and Design of a Variable Baseline Stereo Boom.* (Master of Science in Mechanical Engineering), Virginia Polytechnic Institute and State University, Blacksburg, Virginia.

Faugeras, O., & Luong, Q. T. (2001). *The Geometry of Multiple Images The Laws that Govern the Formation of Multiple Images of a Scene and Some of their Applications* London, England: The MIT Press.

Fernando, W. S. P., Udawatta, L., & Pathirana, P. (2007). *Identification of moving obstacles with pyramidal Lucas and Kanade optical flow and k means clustering.* Paper presented at the Proceedings on the 2007 Third International Conference on Information and Automation for Sustainability.

Frank, B., Stachniss, C., Grisetti, G., Arras, K., & Burgard, W. (2009). Robotics 2 Camera Calibration.

Galbiati, L. J. (1990). Machine Vision and Digital Image Processing Fundamentals. . *New Jersey: Prentice Hall*.

Han, J., Hong, K., & Kim, S. (2012). *Application of a Photogrammetric System for Monitoring Civil Engineering Structures*. Rijeka, Croatia: InTech.

Hornáček, M. (2013). Tutorial: Calibrated Rectification Using OpenCV (Bouguet's Algorithm).

Ibrahim, A., Orense, R. P., Pender, M. J., & Kikkawa, N. (2009). *Quasi-elastic Stiffness of Auckland Clays.* Paper presented at the New Zealand Society for Earthquake Engineering Conference.

Islam, M. (2008). *Developing Video Measurement of Strain for Polymers using Labview.* (Bachelor of Science in Mechanical Engineering), Bangladesh University of Engineering & Technology, Dhaka, Bangladesh.

Johnson, G. W., & Jennings, R. (2001). *Labview Graphical Programming*. USA: McGraw-Hill.

Kheng, L. W. (2012). Computer Vision and Pattern Recognition.

Khosravi, M., Tang, L., Pipatpongsa, T., Takemura, J., & Doncommul, P. (2012). Performance of Counterweight Balance in Stability of Undercut Slope Evaluated by Physical Modeling. *International Journal of Geotechnical Engineering, 6*, 193-205.

Kuhl, A. (2005). *Comparison of Stereo Matching Algorithms for Mobile Robots.* The University of Western Australia.

Lim, M. S., & Lim, J. (2008). Visual measurement of pile movements for the foundation work using a high-speed line-scan camera. *Pattern Recognition, 41*(6), 2025-2033.

Mahalingam, V., Bhattacharya, K., Ranganathan, N., Chakravarthula, H., Murphy, R. R., & Pratt, K. S. (2010). A VLSI Architecture and Algorithm for Lucas-Kanade Based Optical Flow Computation. *IEEE Transaction on Very Large Scale Integration (VLSI) Systems*, 29-38.

Marr, W. A. (2000). Advances and Retreats in Geotechnical Measurements. *ASCE GSP, 111*.

Means, W. D. (1976). *Stress and Strain Basic Concepts of Continuum Mechanics for Geologists*. New York, USA: Springer-Verlag.

Medioni, G., & Kang, S. B. (2004). *Emerging Topics in Computer Vision*.

Neale, W. T. C., Hessel, D., & Terpstra, T. (2011). Photogrammetric Measurement Error Associated with Lens Distortion. *SAE Technical Paper, 1*(0286), 1-52.

O'Donovan, P. (2005). *Optical Flow: Techniques and Applications*. The University of Saskatchewan.

Qiao, H., Nakata, Y., Hyodo, M., & Kikkawa, N. (2008). Triaxial Compression Test for Unsaturated Sandy Soil using Image Processing Technique *Deformational Characteristics of Geomaterials* (pp. 529-534).

Ratananikom, W., Likitlersuang, S., & Yimsiri, S. (2007). *Development of Triaxial System for Soil Testing at Wide Strain Range: Preliminary Results.* Paper presented at the International Symposium on Geotechnical Engineering, Ground Improvement, and Geosynthetics for Human Security and Environmental Preservation.

Rodriguez, J. M., Johansson, J. M. A., & Edeskär, T. (2012). *Particle Shape Determination by Two-Dimension Image Analysis in Geotechnical Engineering.* . Paper presented at the Proceedings of Nordic Conference on Soil Mechanics and Geotechnical NGM.

Rojas, J. C., Gallipoli, D., & Wheeler, S. J. (2012). Image analysis of strains in soils subjected to wetting and drying. *ATM Geotechnical Testing Journal, 35*(1).

Sach, L. T., Atsuta, K., Hamamoto, K., & Kondo, S. (2009). A Robust Stereo Matching Method for Low Texture Stereo Images. *IEEE*.

Sadd, M. H. (2005). *Elasticity Theory, Applications and Numeric.* USA: Elsevier.

Saidon, M. S., Desa, H., Murugesa, P., & Rosbi, M. S. M. (2009). Developing Stereo Vision System for Object Recognition and Positioning of AMAD-R Mobile Robot. *Proceedings of the International Conference on Man-Machine Systems*, 3B8-1-5.

Salvi, J., Armangue, X., & Batlle, J. (2002). A Comparative Review of Camera Methods with Accuracy Evaluation. *Pattern Recognition, 35*, 18.

Scharstein, D. (1997). *View Sythesis Using Stereo Vision.* (Doctor of Philosophy), Cornell University.

Sonka, M., Hlavac, V., & Boyle, R. (2008). *Image Processing Analysis, and Machine Vision* (3rd Edition ed.). United States of America: Thomson Learning

Sutton, M. A., Orteu, J. J., & Schreier, H. W. (2009). *Image Correlation for Shape, Motion and Deformation Measurements: Basic Concepts, Theory and Applications*: Springer.

Sutton, M. A., Yan, J., Deng, X., Cheng, C. S., & Zavattieri, P. (2007). Three dimensional digital image correlation to quantify deformation and crack opening displacement in ductile aluminum under mixed-mode I/III loading. . *Optical Engineering, 46*(5).

Thota, S. D., Vemulapalli, K. S., Chintalapati, K., & Srinivas, P. S. (2013). Comparison Between The Optical Flow Computational Techniques. *International Journal of Engineering Trends and Technology, 4*(10), 5.

Tung, S. H., & Sui, C. H. (2010). Application of Digital Image Correlation Techniques in Analyzing Cracked Cylindrical Pipes. *Sadhana, 35*(5), 557-567.

Viggiani, G., & Hall, S. A. (2008). *Full-field measurements, a new tool for laboratory experimental geomechanics.* Paper presented at the Proceedings of the 4th International Symposium on Deformation Characteristics of Geomaterials (Burns SE, Mayne PW and Santamarina JC (Eds.)).

Wedel, A., & Cremers, D. (2011). *Stereo Scene Flow for 3D Motion Analysis* (Vol. 9).

White, D. J., Take, W. A., & Bolton, M. D. (2001). *Measuring Soil Deformation in Geotechnical Models using Digital Images and PIV Analysis.* Paper presented at the 10th International Conference on Computer Methods and Advances in Geomechanics Balkema, Rotterdam.

Wu, H. Y., Rubinstein, M., Shih, E., Guttag, J., Durand, F., & Freeman, W. T. (2012). Eulerian video magnification for revealing subtle changes in the world.

Xing, Z. X., Wells, L. G., Yaping, J., & Shearer, S. A. (1997). Using Image Analysis to Measure Two-Dimensional Soil Deformation. *Journal of Terramechanics, 34*(2), 73-82.

Xue, T., Wu, B., Zhu, J. G., & Ye, S. H. (2007). Complete Calibration of a Structure-Uniform Stereovision Sensor with Free-Position Planar Pattern. . *Sensors and Actuators, 135*, 185-191.

Yamamoto, H. (2008). *Application of digital image analysis to displacement measurements of sand particles in shear zone.* Paper presented at the Deformational Characteristics of Geomaterials: Proceedings of the Fourth International Symposium on Deformation Characteristics of Geomaterials, IS Atlanta 2008, 22-24 September 2008, Atlanta, Georgia, USA.

Zhang, Z. (1998). A Flexible New Technique for Camera Calibration. Redmond, WA: Microsoft Corporation.

APPENDIX

2D Prototype Data

A. Accuracy Check

Table 5.2.1 Summary of results

Physical movement (mm)	1mm		0.5mm	
	Left	Right	Left	Right
Calculated reading	1.08	1.08	0.58	0.54
	1.08	0.91	0.53	0.43
	0.94	1.03	0.57	0.53
	1.07	1.01	0.55	0.54
	1.17	1.11	0.46	0.47
	1.08	1.10	0.46	0.46
	1.06	1	0.43	0.48
	0.93	0.98	0.41	0.51
	1.09	0.99	0.43	0.42
	1.27	1.09	0.42	0.46
Standard deviation	0.097772	0.065296	0.066903	0.044754

B. Displacement and Strain Field

Test 1: Right Camera

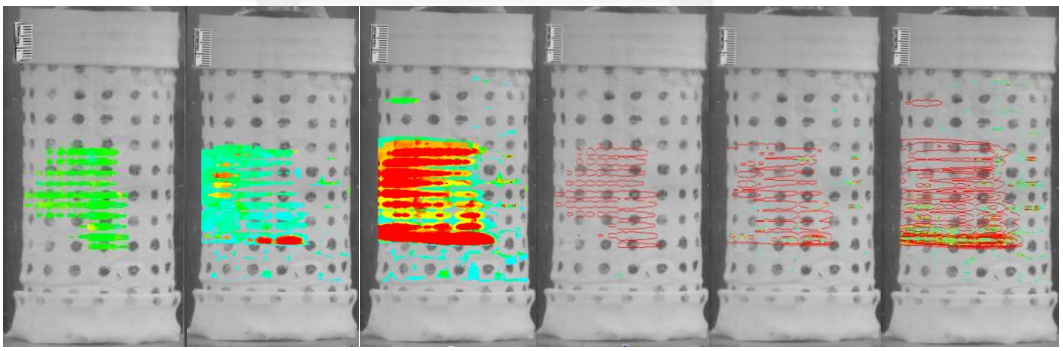

Figure 5.2.1 Results of displacement field and strian field at day 1, 2 and end of the test

Test 1: Left Camera

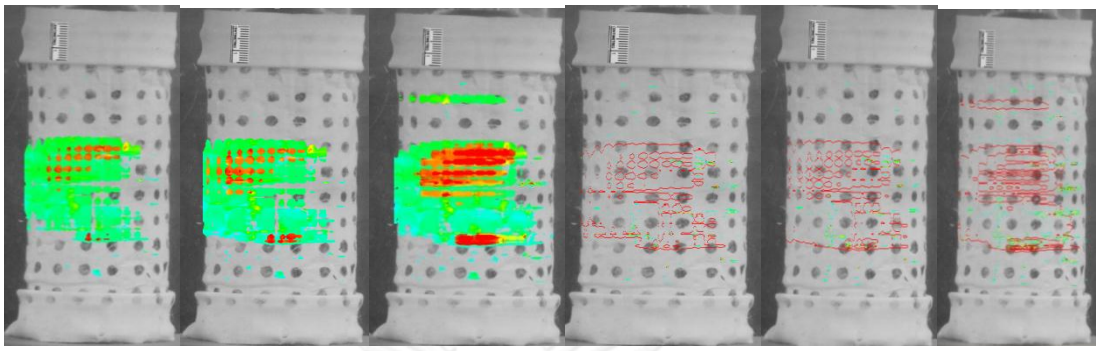

Figure 5.2.2 Results of displacement field and strian field at day 1, 2 and end of the test

Test 2: Right Camera

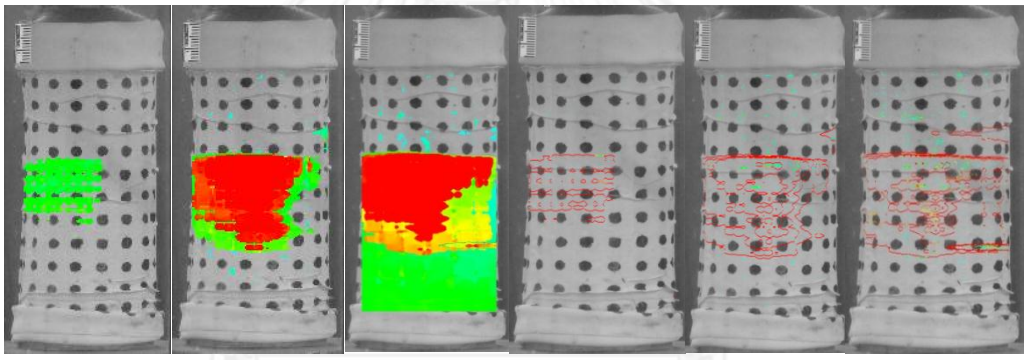

Figure 5.2.3 Results of displacement field and strian field at day 1, 2 and end of the test

Test 2: Left Camera

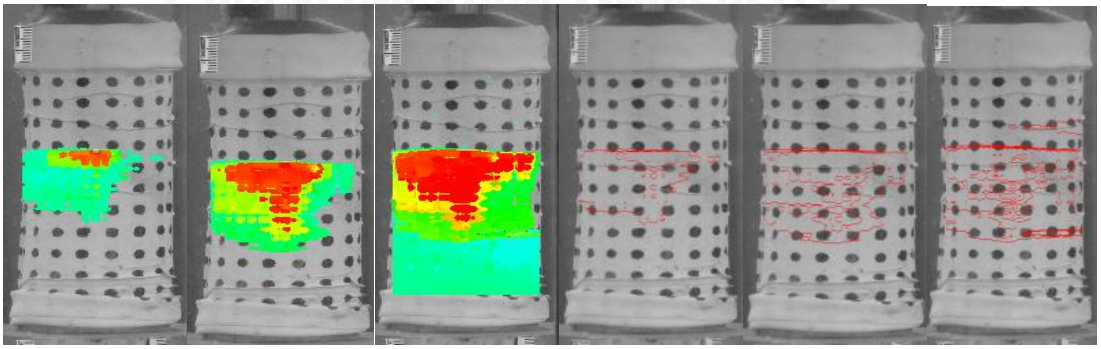

Figure 5.2.4 Results of displacement field and strian field at day 1, 2 and end of the test

Binocular Stereo Vision Data

Trial 1

A. Picture 0

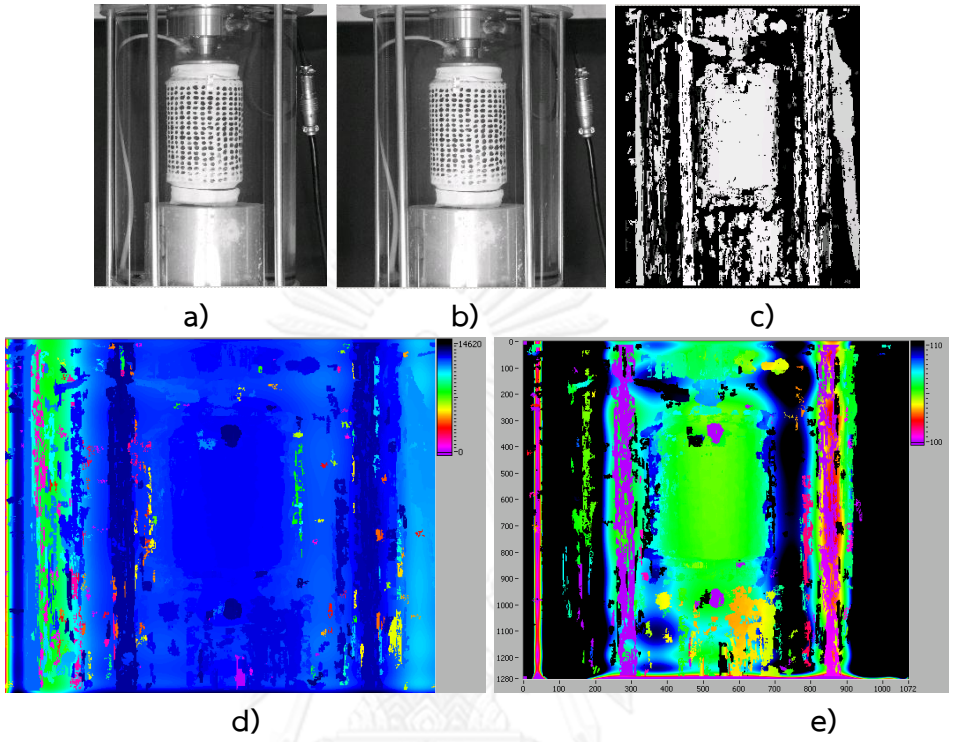

a) b) c)

d) e)

Figure 5.2.5 Binocular stereo vision data 1 a) left image b) right image c) disparity image d) disparity map e) depth map

B. Picture 1

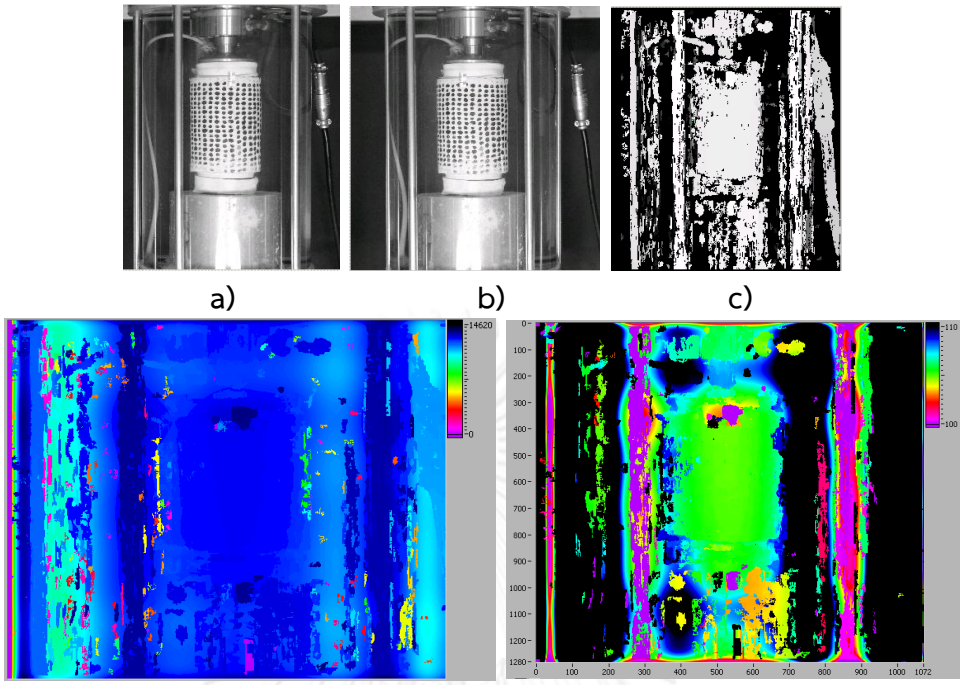

a) b) c)

d) e)

Figure 5.2.6 Binocular stereo vision data 2 a) left image b) right image c) disparity image d) disparity map e) depth map

C. Picture 2

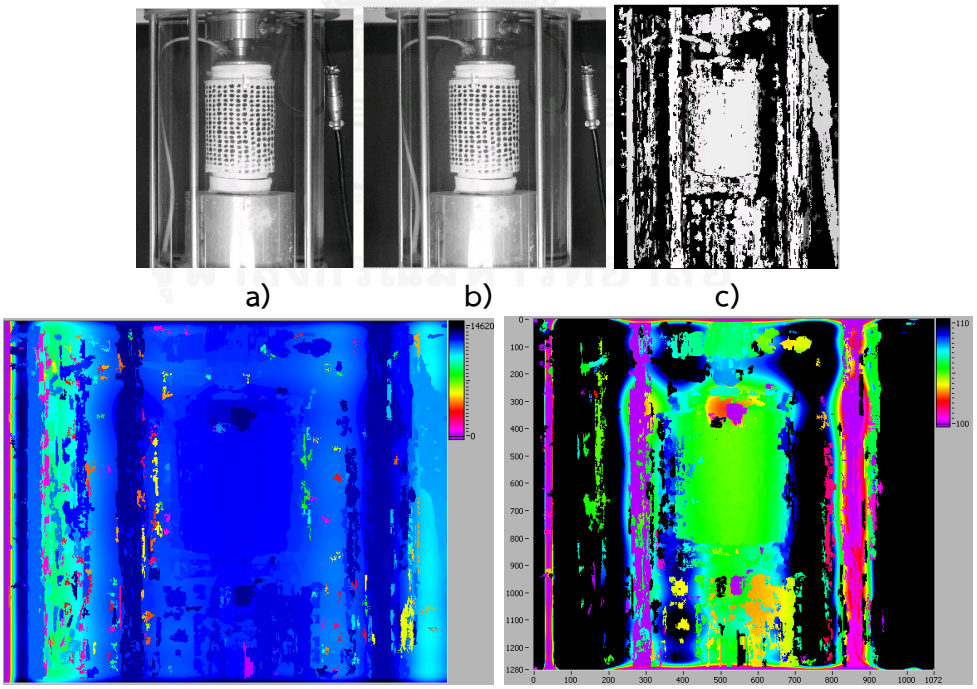

a) b) c)

d) e)

Figure 5.2.7 Binocular stereo vision data 3 a) left image b) right image c) disparity image d) disparity map e) depth map

D. Picture 3

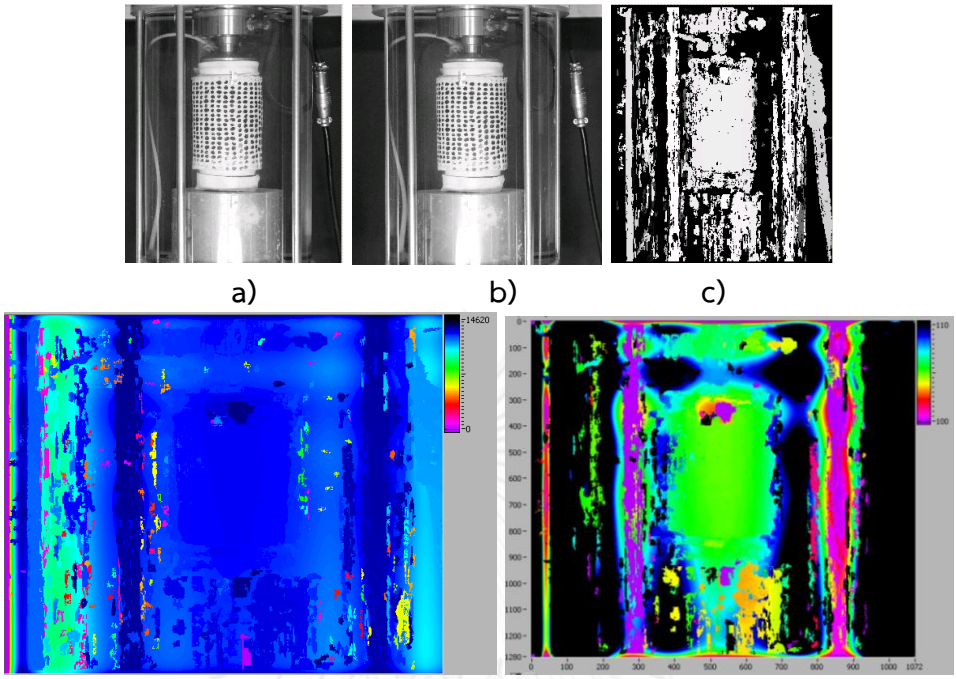

a) b) c)

d) e)

Figure 5.2.8 Binocular stereo vision data 4 a) left image b) right image c) disparity image d) disparity map e) depth map

E. Picture 4

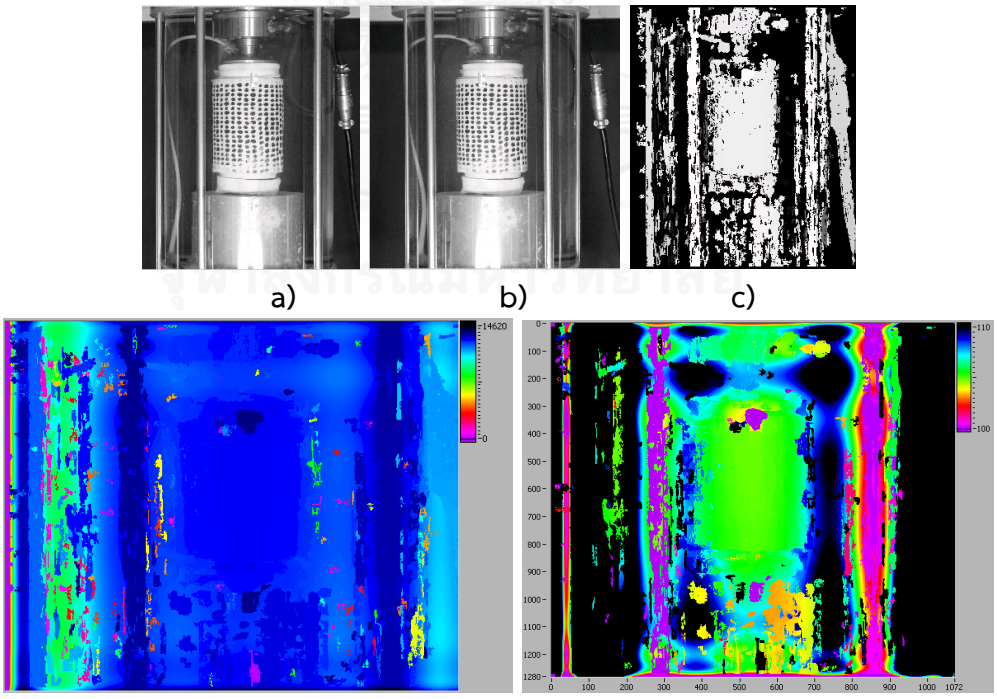

a) b) c)

d) e)

Figure 5.2.9 Binocular stereo vision data 5 a) left image b) right image c) disparity image d) disparity map e) depth map

F. Picture 5

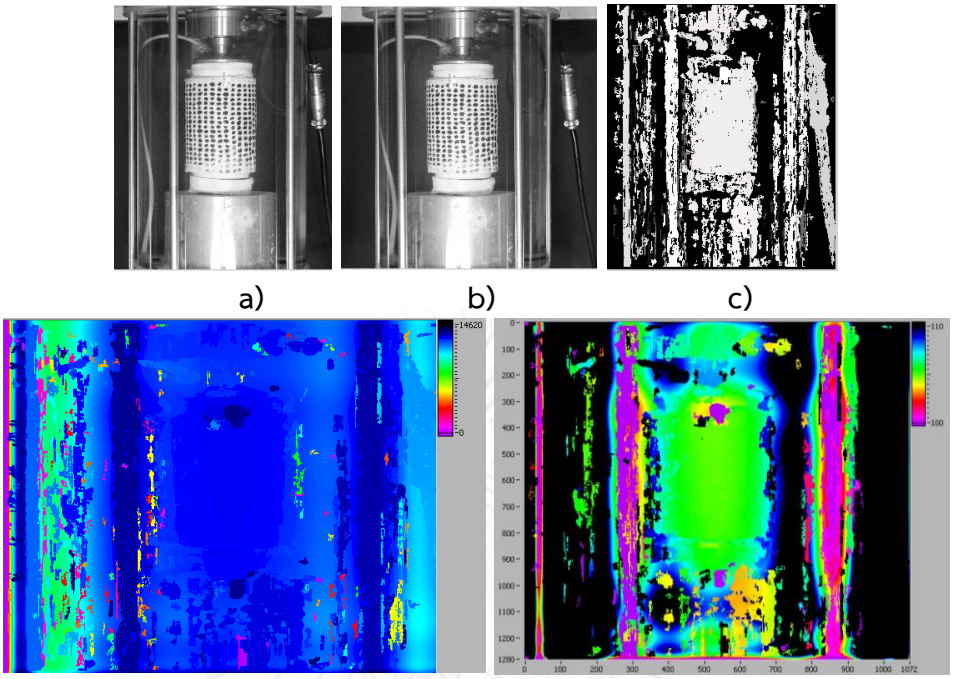

a) b) c)

d) e)

Figure 5.2.10 Binocular stereo vision data 6 a) left image b) right image c) disparity image d) disparity map e) depth map

G. Picture 6

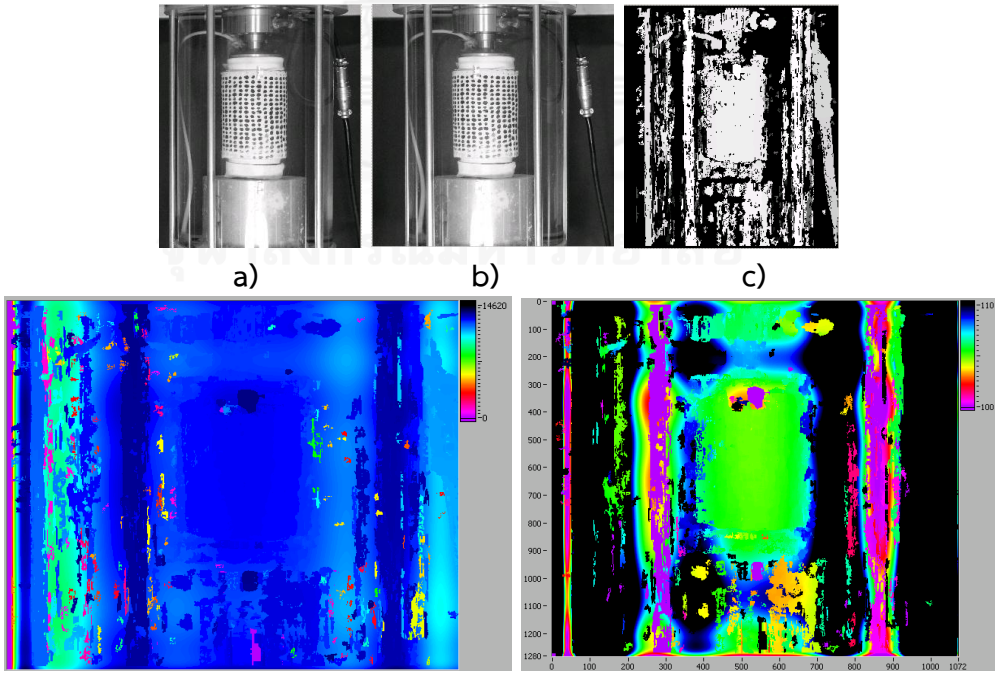

a) b) c)

d) e)

Figure 5.2.11 Binocular stereo vision data 7 a) left image b) right image c) disparity image d) disparity map e) depth map

H. Picture 7

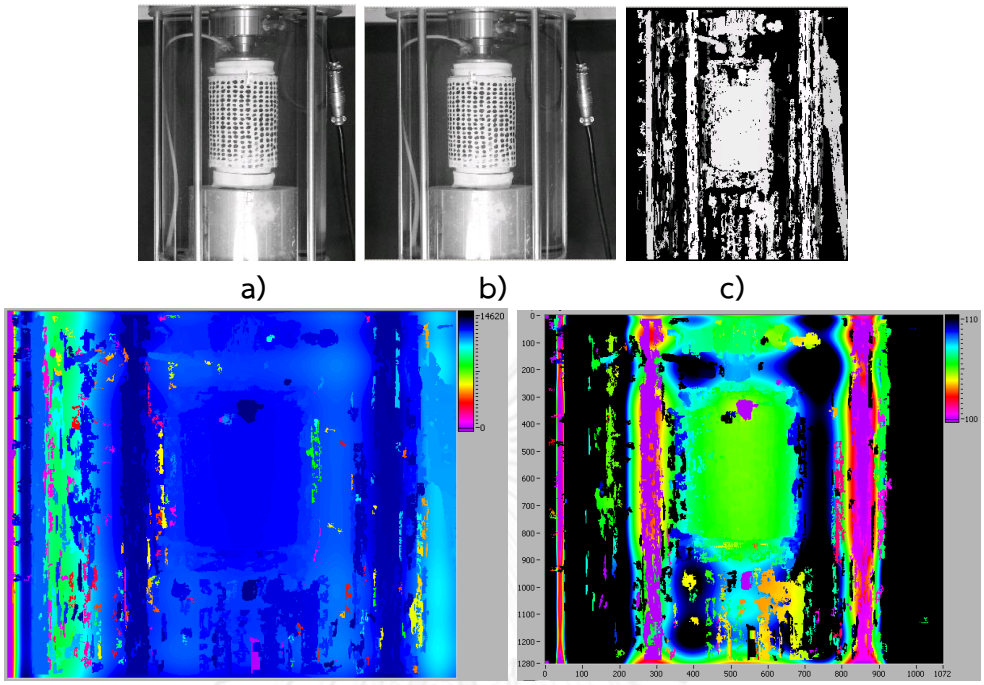

a) b) c)

d) e)

Figure 5.2.12 Binocular stereo vision data 8 a) left image b) right image c) disparity image d) disparity map e) depth map

I. Picture 8

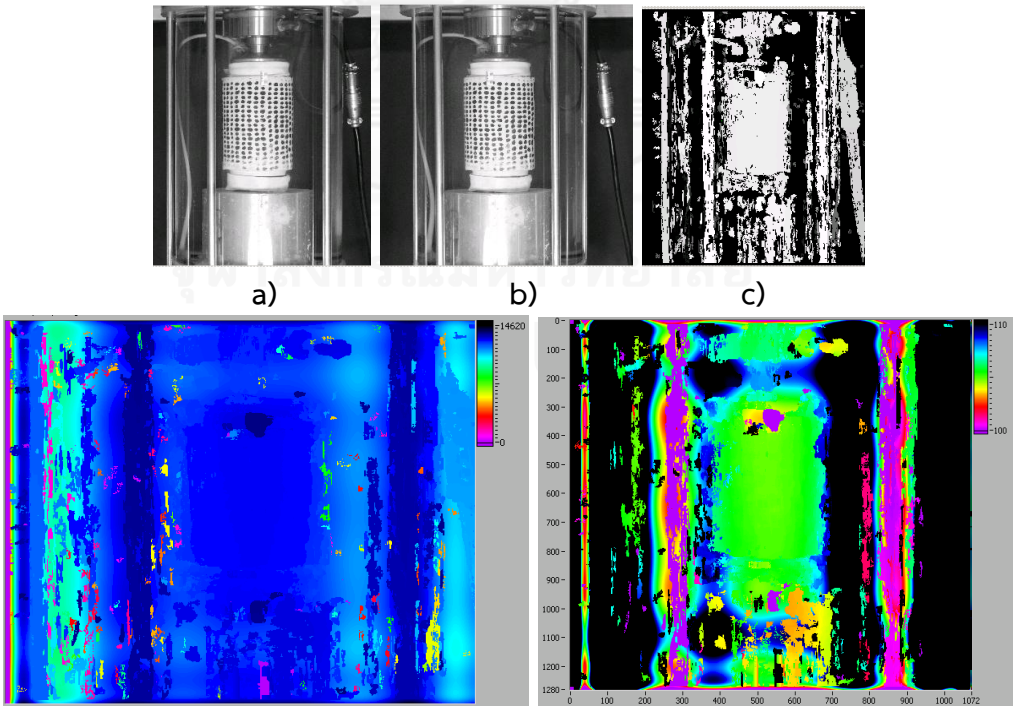

a) b) c)

d) e)

Figure 5.2.13 Binocular stereo vision data 9 a) left image b) right image c) disparity image d) disparity map e) depth map

Table 5.2.2 Results of Trial 1 when the change of volume was computed

	Patch Size	Change in Volume from Image Processing (cc)	Change in Volume from Burette (cc)	%error
0to1	32	14.95	14.71	1.56
1to2	51	63.12	64.05	-1.47
2to3	31	7.36	7.04	4.39

Trial 2

A. Picture 0

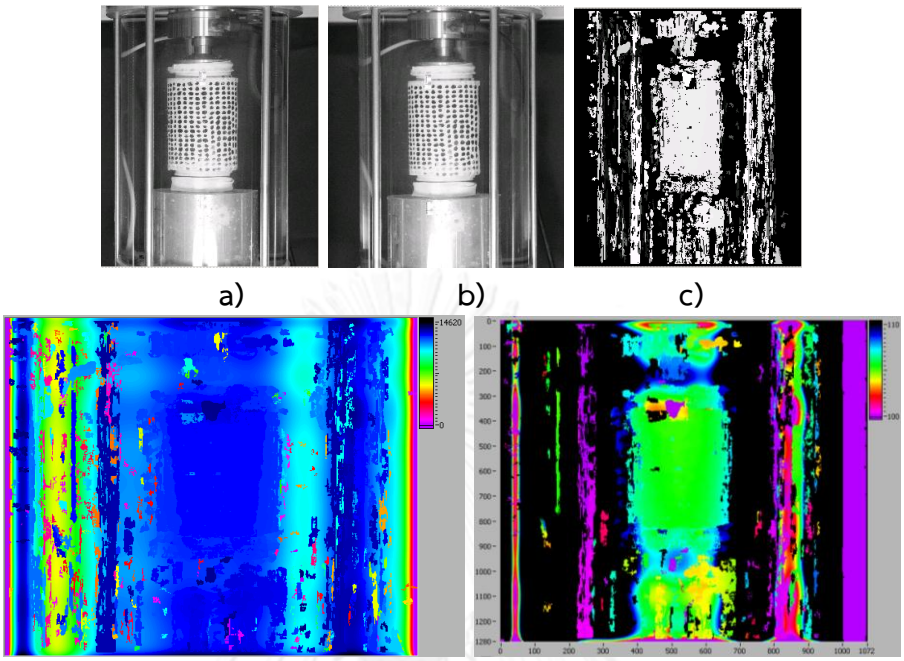

a) b) c)

d) e)

Figure 5.2.14 Binocular stereo vision data 1 a) left image b) right image c) disparity image d) disparity map e) depth map

B. Picture 1

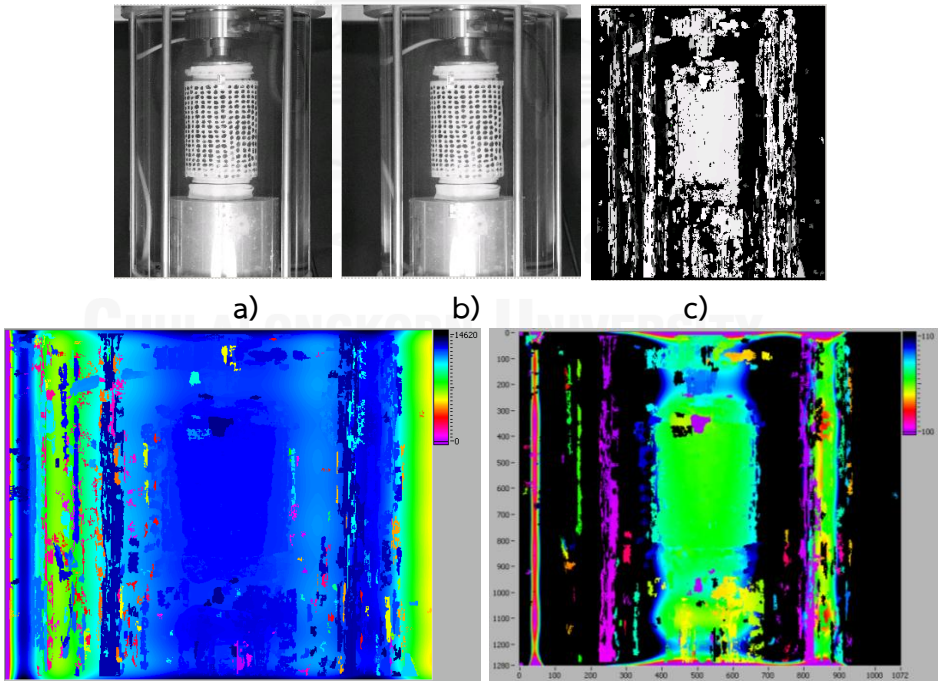

a) b) c)

d) e)

Figure 5.2.15 Binocular stereo vision data 2 (a) left image (b) right image (c) disparity image (d) disparity map (e) depth map

C. Picture 2

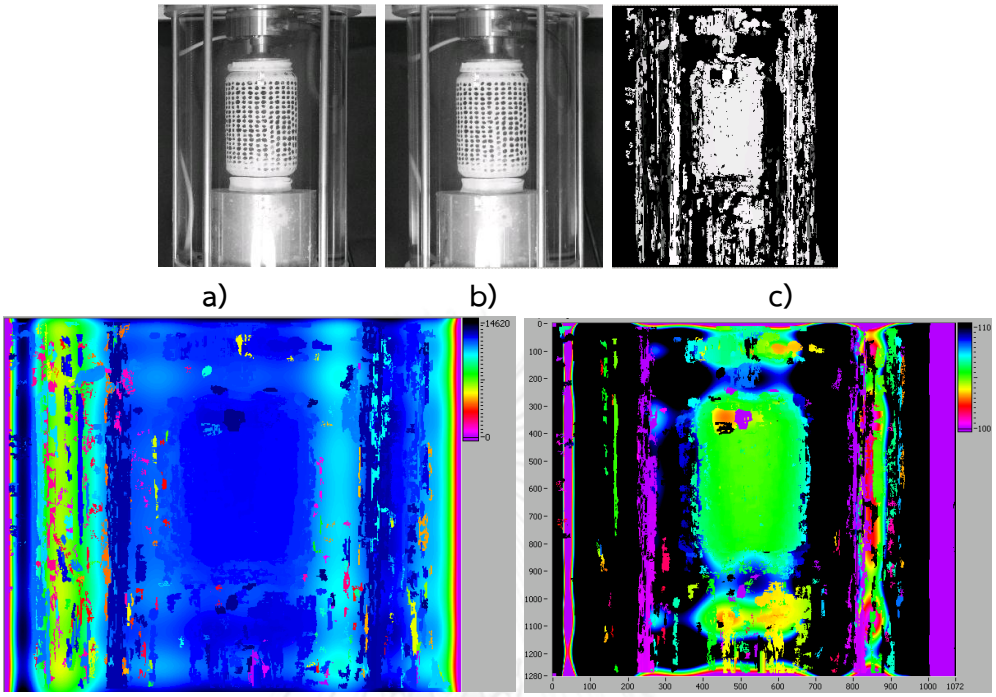

a) b) c)

d) e)

Figure 5.2.16 Binocular stereo vision data 3 a) left image b) right image c) disparity image d) disparity map e) depth map

D. Picture 3

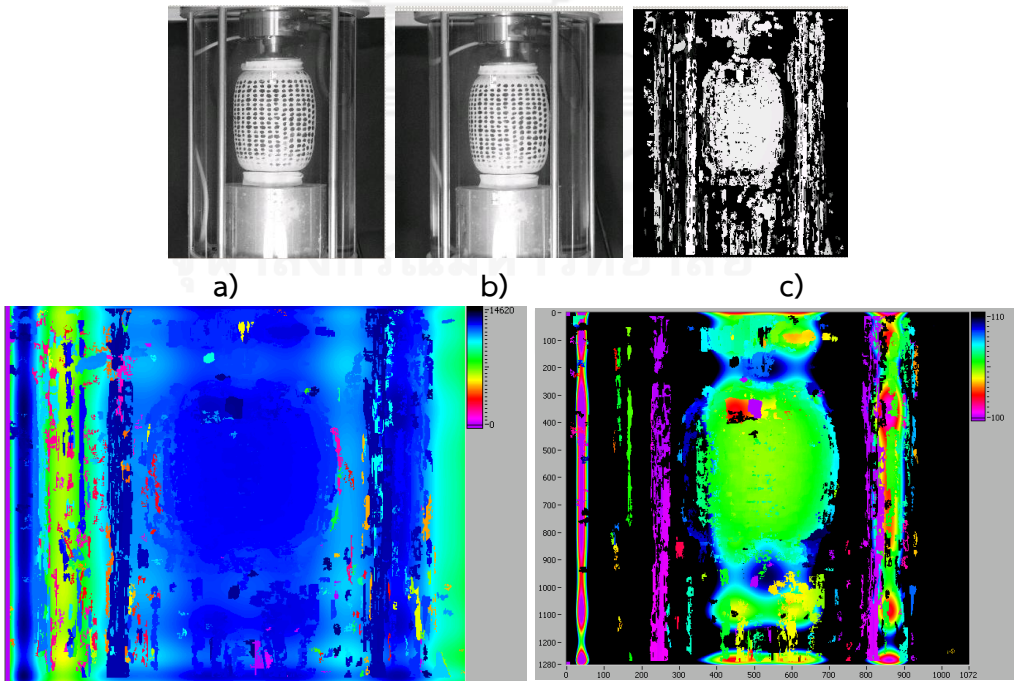

a) b) c)

d) e)

Figure 5.2.17 Binocular stereo vision data 4 a) left image b) right image c) disparity image d) disparity map e) depth map

E. Picture 4

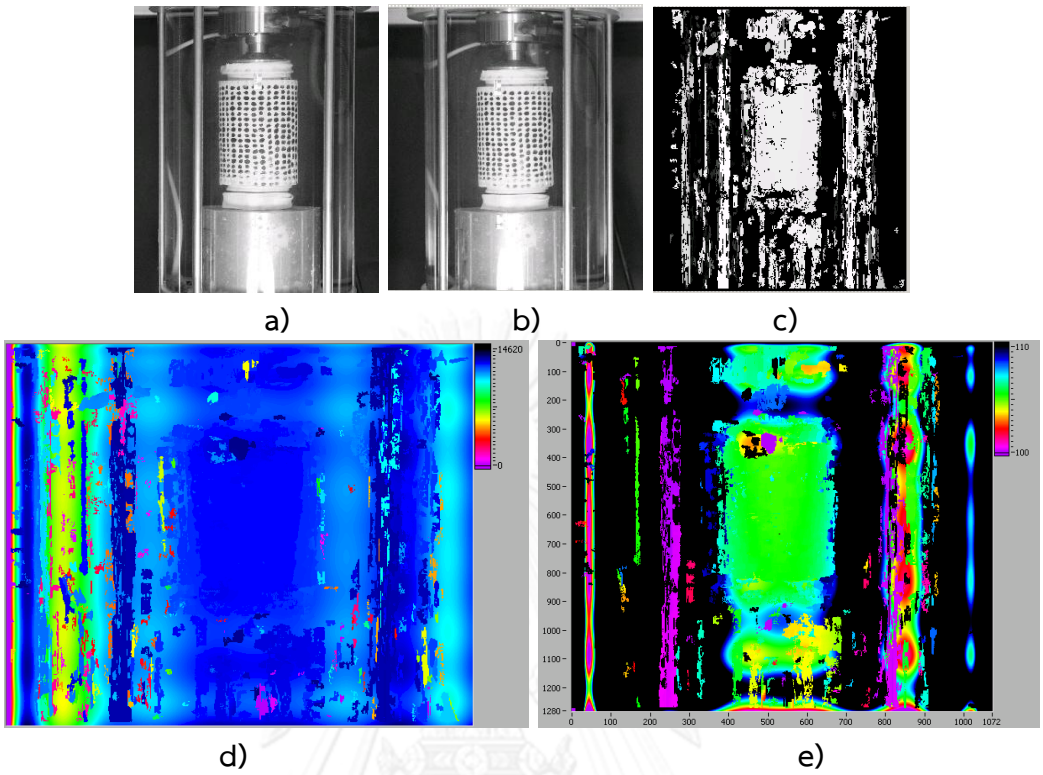

a) b) c)

d) e)

Figure 5.2.18 Binocular stereo vision data 5 a) left image b) right image c) disparity image d) disparity map e) depth map

Table 5.2.3 Results of Trial 2 when the reference image used was taken before the test begins

Steps	Patch Size	Volume from Image Processing (cc)	Volume from Burette (cc)	%error
0to1	46	13.66	13.49	1.27
0to2	52	22.25	21.15	5.07
0to3	54	46.45	45.88	1.23
0to4	34	34.01	34.25	-0.71

Trial 3

A. Picture 0

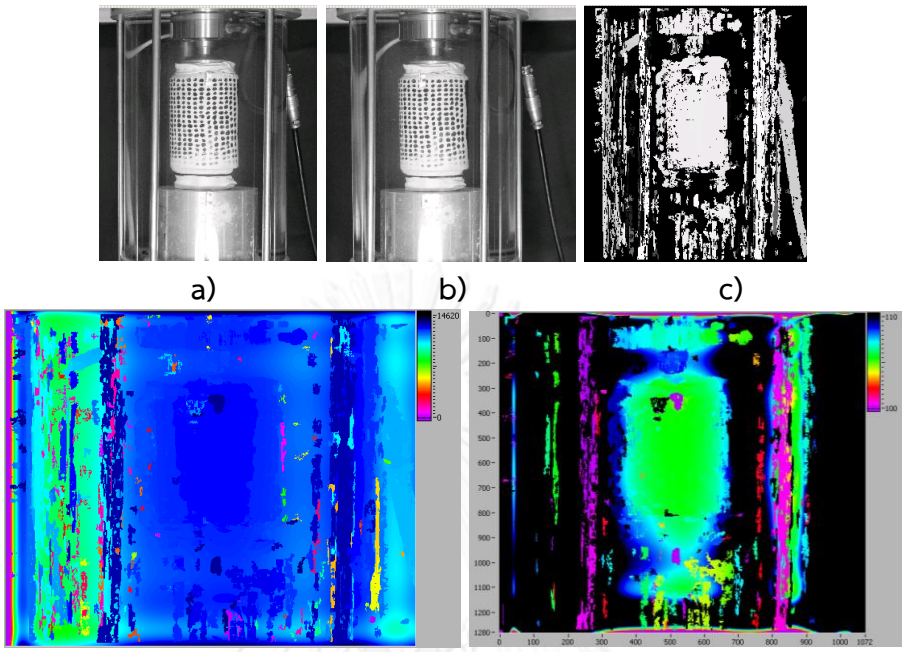

a) b) c)

d) e)

Figure 5.2.19 Binocular stereo vision data 1 a) left image b) right image c) disparity image d) disparity map e) depth map

B. Picture 1

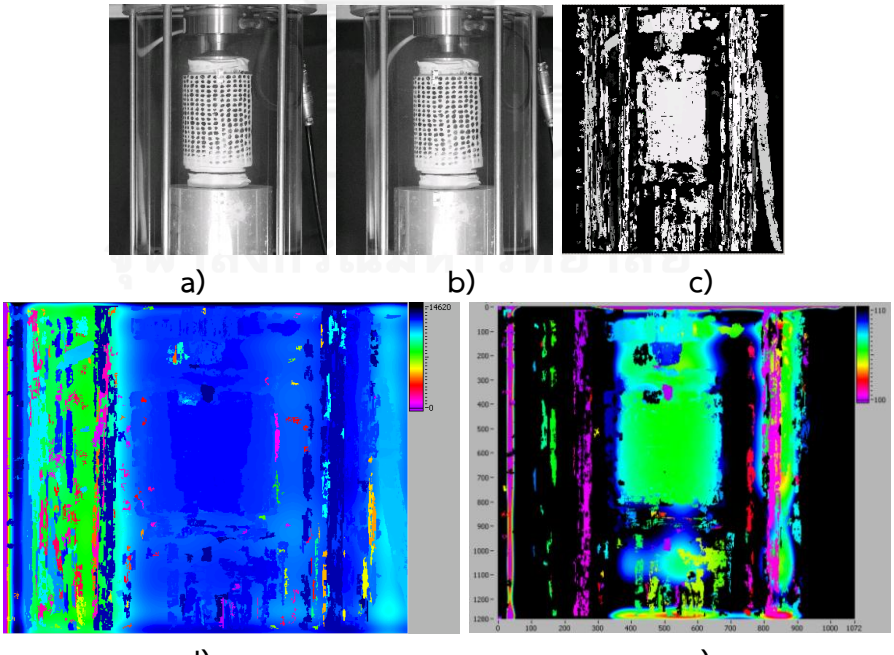

a) b) c)

d) e)

Figure 5.2.20 Binocular stereo vision data 2 a) left image b) right image c) disparity image d) disparity map e) depth map

C. Picture 2

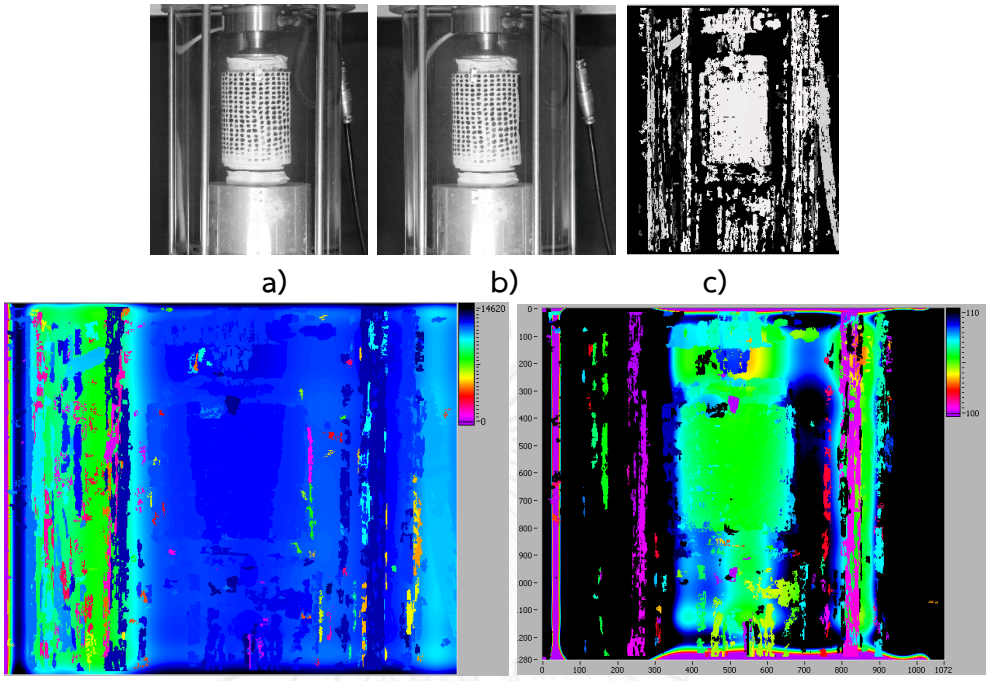

a) b) c)

d) e)

Figure 5.2.21 Binocular stereo vision data 3 a) left image b) right image c) disparity image d) disparity map e) depth map

D. Picture 3

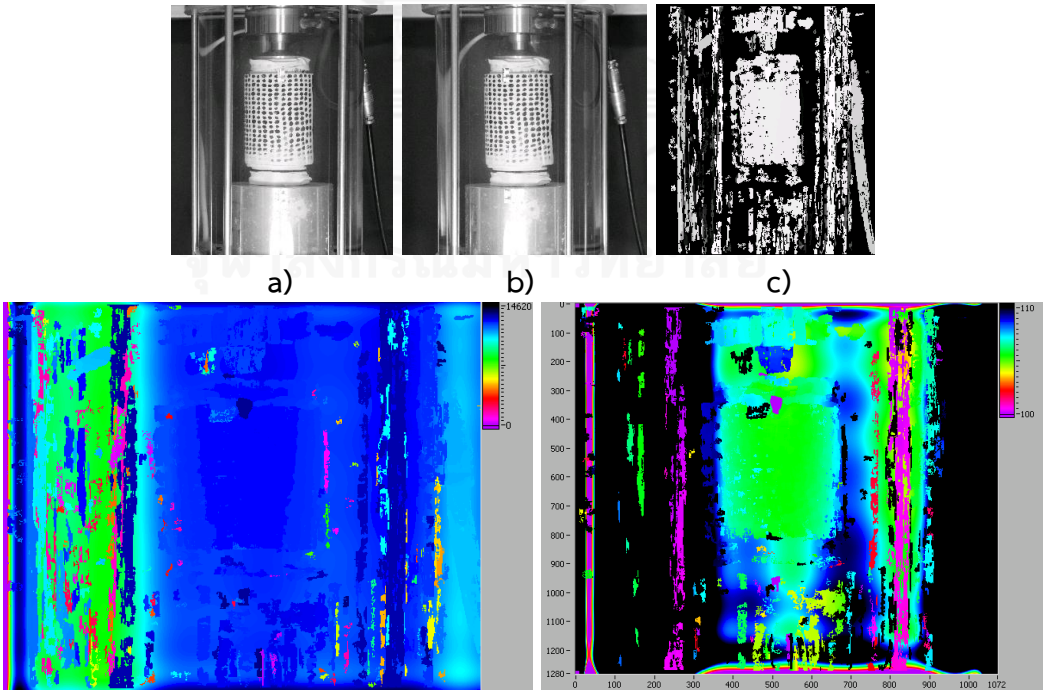

a) b) c)

d) e)

Figure 5.2.22 Binocular stereo vision data 4 a) left image b) right image c) disparity image d) disparity map e) depth map

E. Picture 4

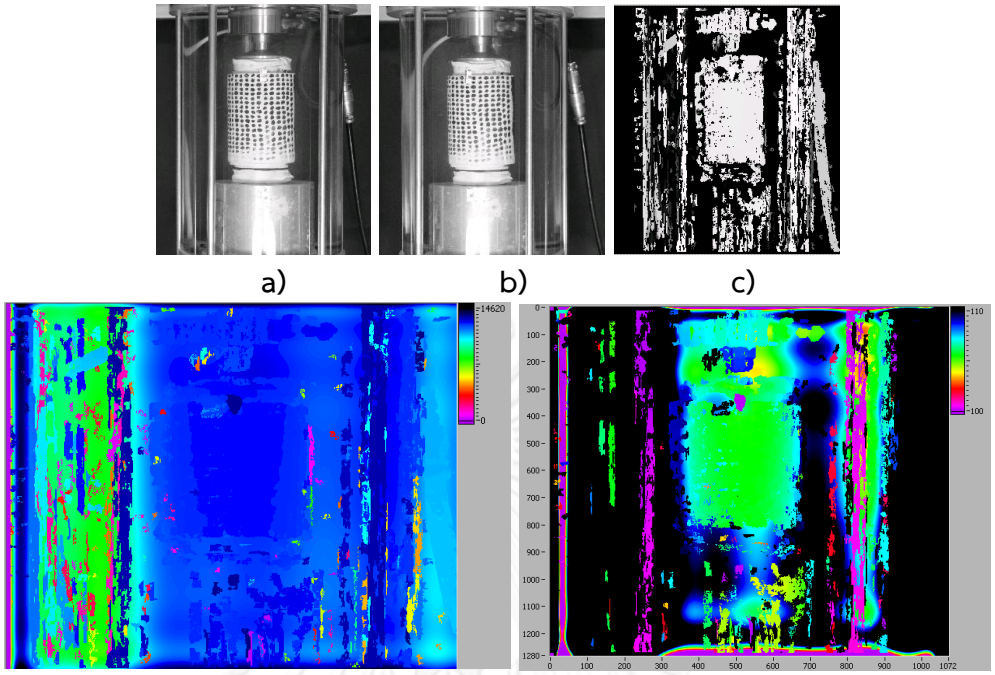

a) b) c)

d) e)

Figure 5.2.23 Binocular stereo vision data 5 a) left image b) right image c) disparity image d) disparity map e) depth map

F. Picture 5

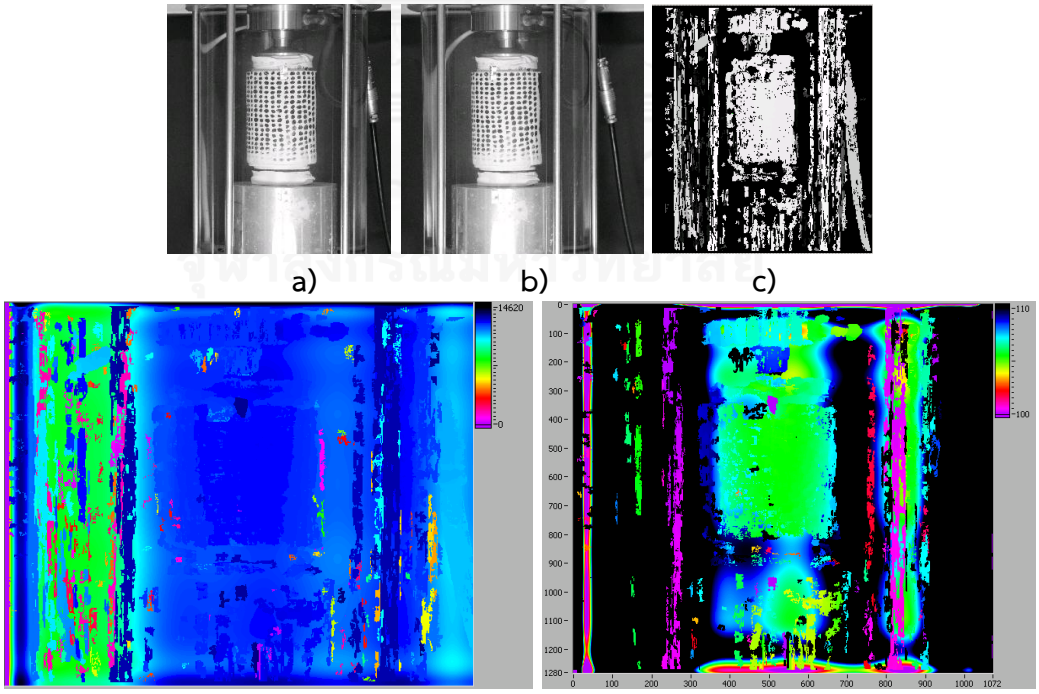

a) b) c)

d) e)

Figure 5.2.24 Binocular stereo vision data 6 a) left image b) right image c) disparity image d) disparity map e) depth map

Table 5.2.4 Results of Trial 3 when the reference image was taken before the test begins

Steps	Patch Size	Volume from Image Processing (cc)	Volume from Burette (cc)	%error
0to1	58	14.64	15.23	-3.97
0to2	58	14.75	15.20	-3.00
0to3	38	22.36	22.1	1.18
0to4	39	14.51	15.1	-3.96

Table 5.2.5 Results of Trial 3 when the reference image was the first image after the test begins

Steps	Patch Size	Volume from Image Processing (cc)	Volume from Burette (cc)	%error
1to2	44	15.59	15.20	2.52
1to3	42	20.31	22.10	-8.42
1to4	39	14.97	15.10	-0.84
1to5	48	9.75	9.40	3.61

Trial 4

A. Picture 0

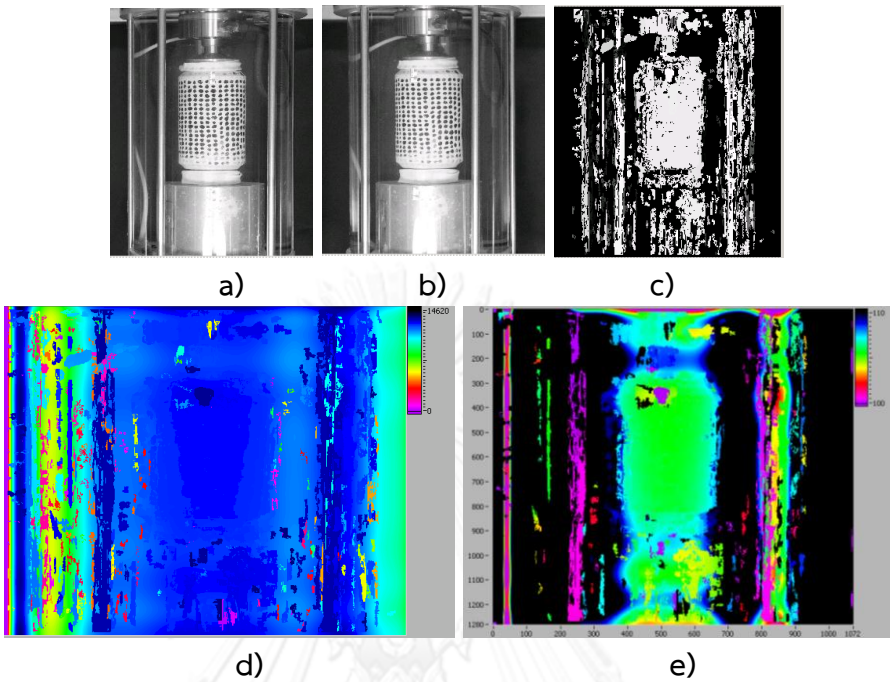

a) b) c)

d) e)

Figure 5.2.25 Binocular stereo vision data 1 a) left image b) right image c) disparity image d) disparity map e) depth map

B. Picture 1

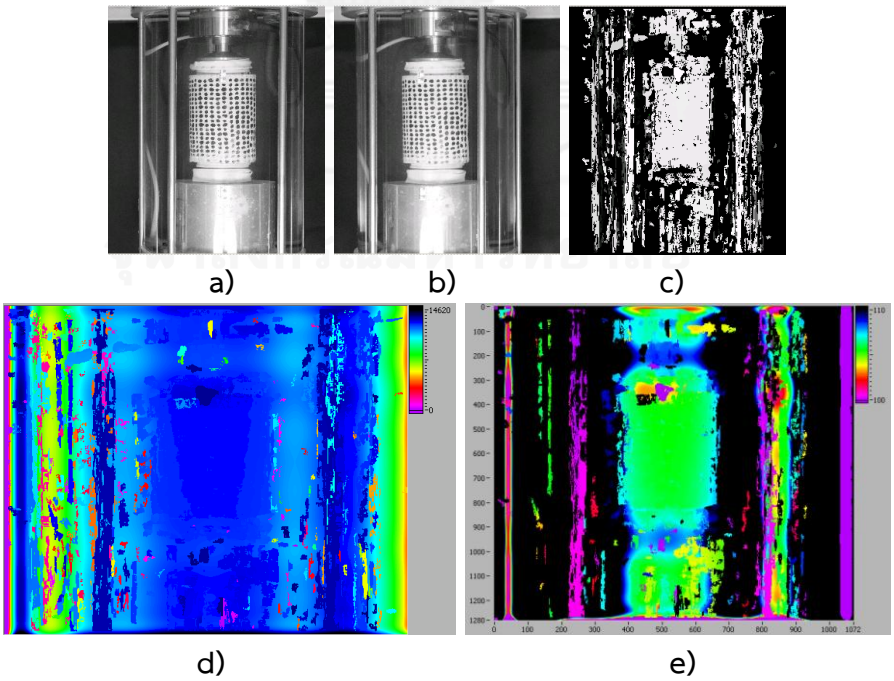

a) b) c)

d) e)

Figure 5.2.26 Binocular stereo vision data 2 a) left image b) right image c) disparity image d) disparity map e) depth map

C. Picture 2

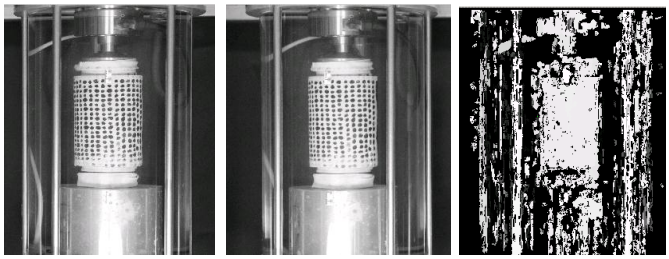

a) b) c)

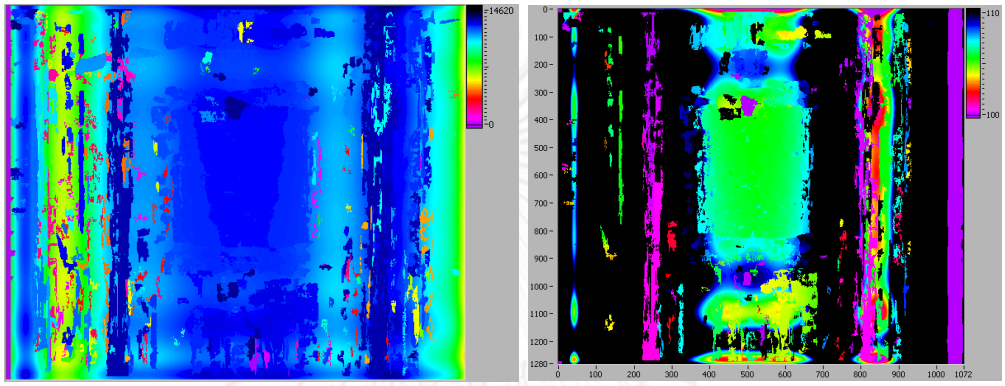

d) e)

Figure 5.2.27 Binocular stereo vision data 3 a) left image b) right image c) disparity image d) disparity map e) depth map

D. Picture 3

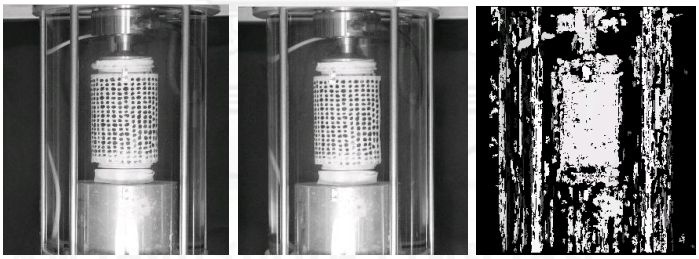

a) b) c)

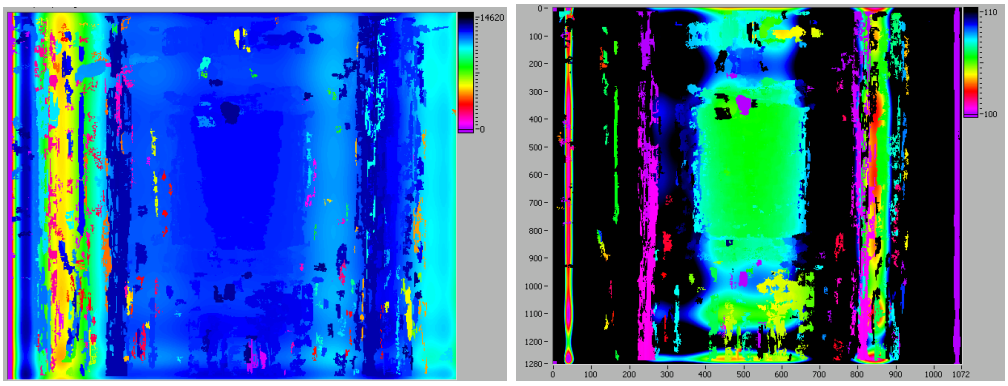

d) e)

Figure 5.2.28 Binocular stereo vision data 4 a) left image b) right image c) disparity image d) disparity map e) depth map

E. Picture 4

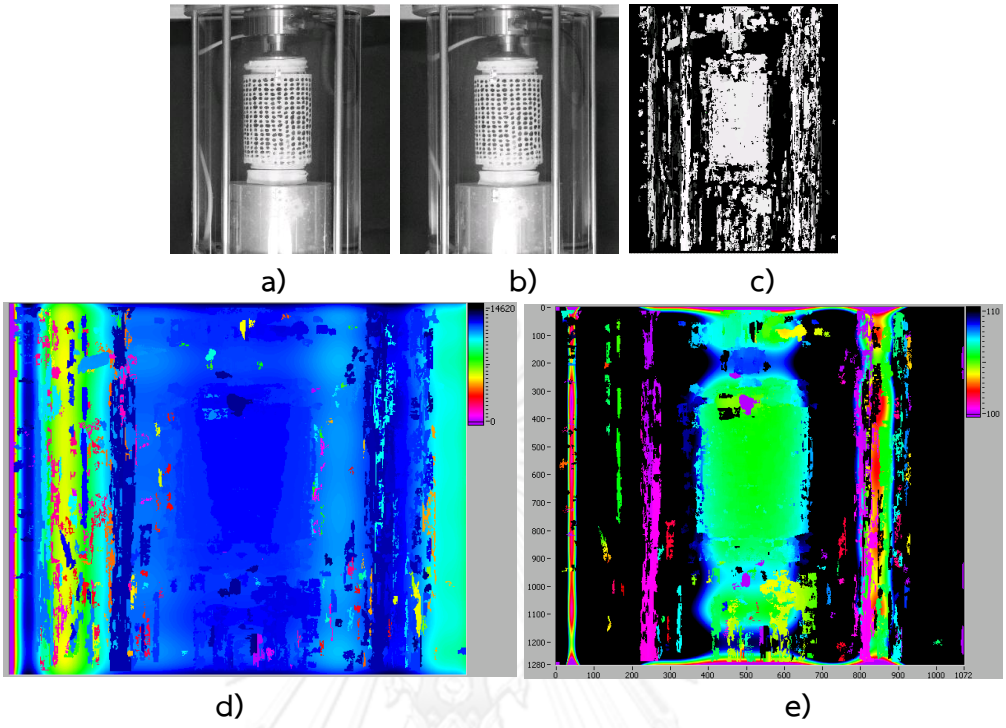

Figure 5.2.29 Binocular stereo vision data 5 a) left image b) right image c) disparity image d) disparity map e) depth map

F. Picture 5

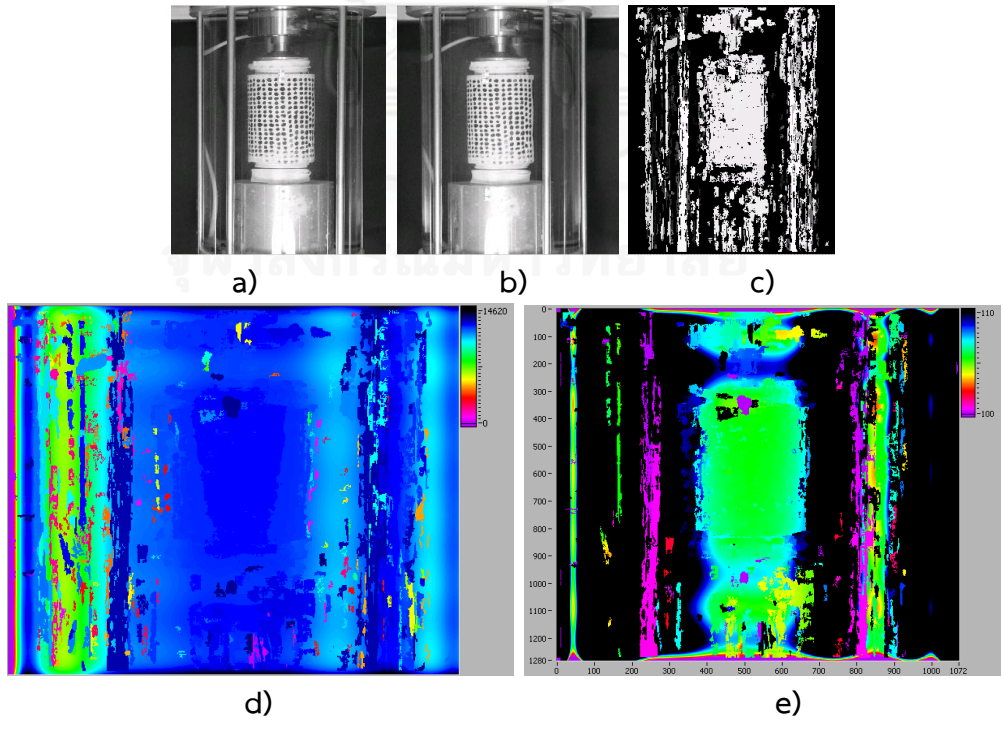

Figure 5.2.30 Binocular stereo vision data 6 (a) left image (b) right image (c) disparity image (d) disparity map (e) depth map

Table 5.2.6 Results of Trial 4 when the reference image used was taken before the test begins

Steps	Patch Size	Volume from Image Processing (cc)	Volume from Burette (cc)	%error
0to1	46	14.13	13.48	4.72
0to4	36	25.59	25.67	-0.31
0to5	35	21.85	20.66	5.60

Table 5.2.7 Results of Trial 4 when the reference image was the first image after the test begins

Steps	Patch Size	Volume from Image Processing (cc)	Volume from Burette (cc)	%error
0to1	46	14.13	13.48	4.72
1to2	35	33.28	32.09	3.63
2to3	34	5.34	5.51	-3.09
3to4	27	14.20	14.36	1.10
4to5	46	4.82	5.01	3.74

Trial 5

A. Picture 0

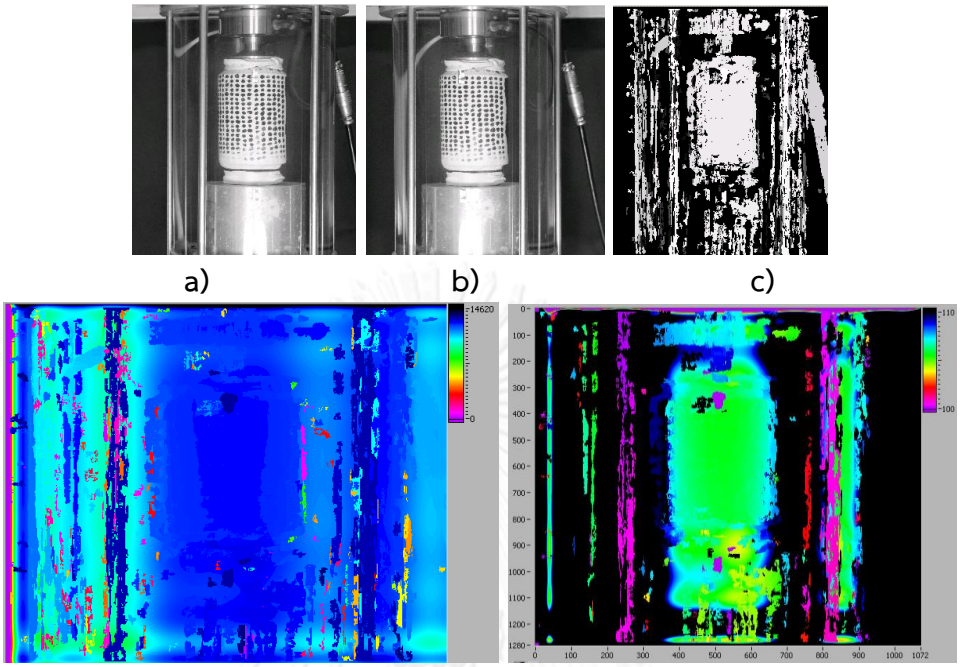

a) b) c)

d) e)

Figure 5.2.31 Binocular stereo vision data 1 (a) left image (b) right image (c) disparity image (d) disparity map (e) depth map

B. Picture 1

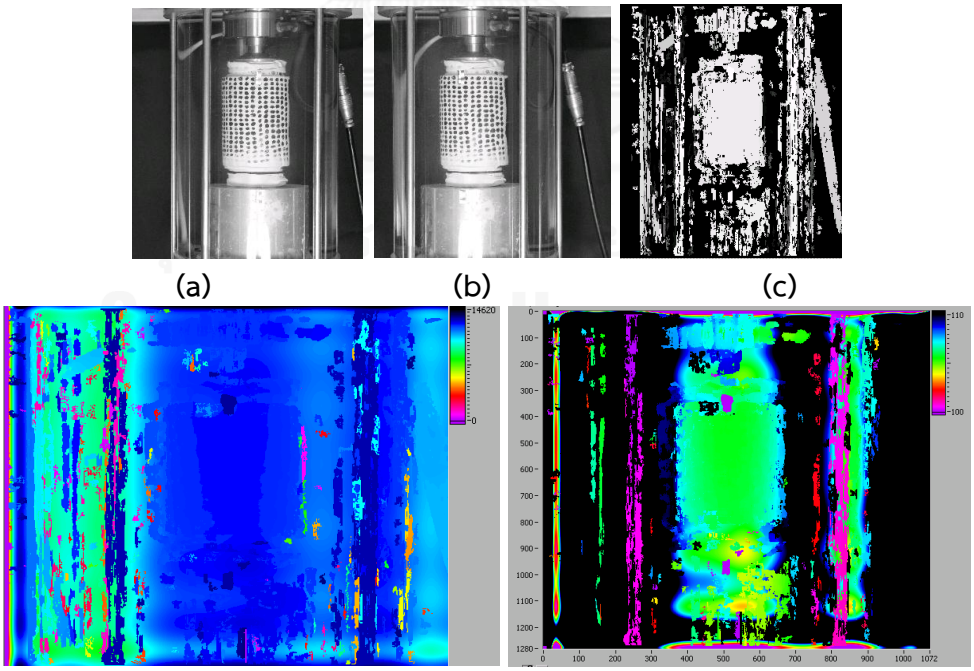

(a) (b) (c)

(d) (e)

Figure 5.2.32 Binocular stereo vision data 2 (a) left image (b) right image (c) disparity image (d) disparity map (e) depth map

C. Picture 2

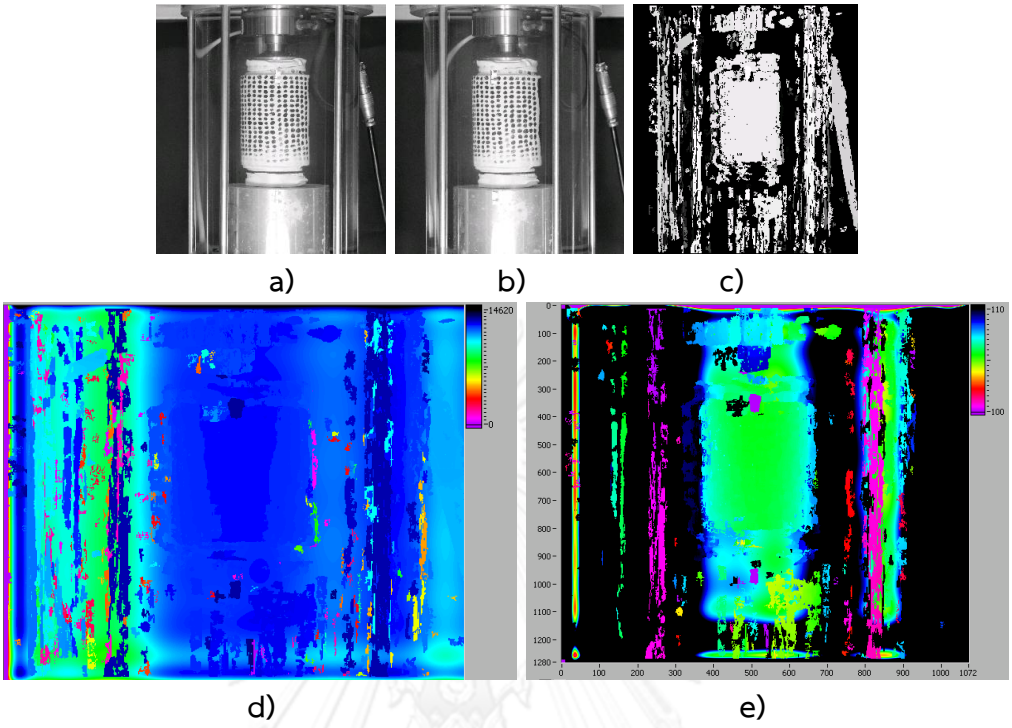

a) b) c)

d) e)

Figure 5.2.33 Binocular stereo vision data 3 a) left image b) right image c) disparity image d) disparity map e) depth map

D. Picture 3

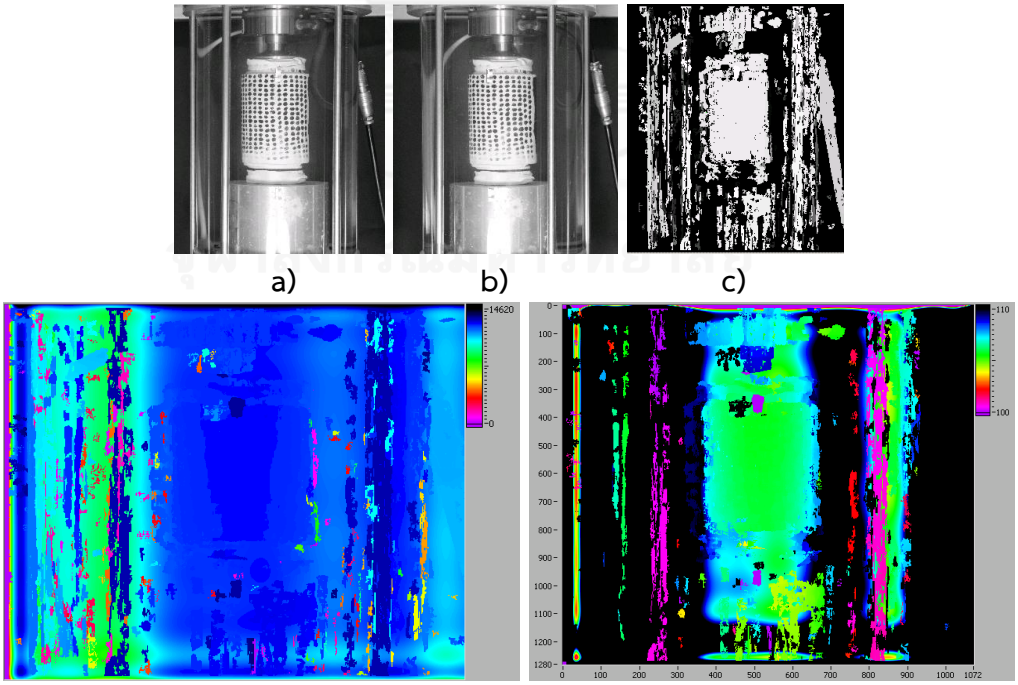

a) b) c)

d) e)

Figure 5.2.34 Binocular stereo vision data 4 a) left image b) right image c) disparity image d) disparity map e) depth map

E. Picture 4

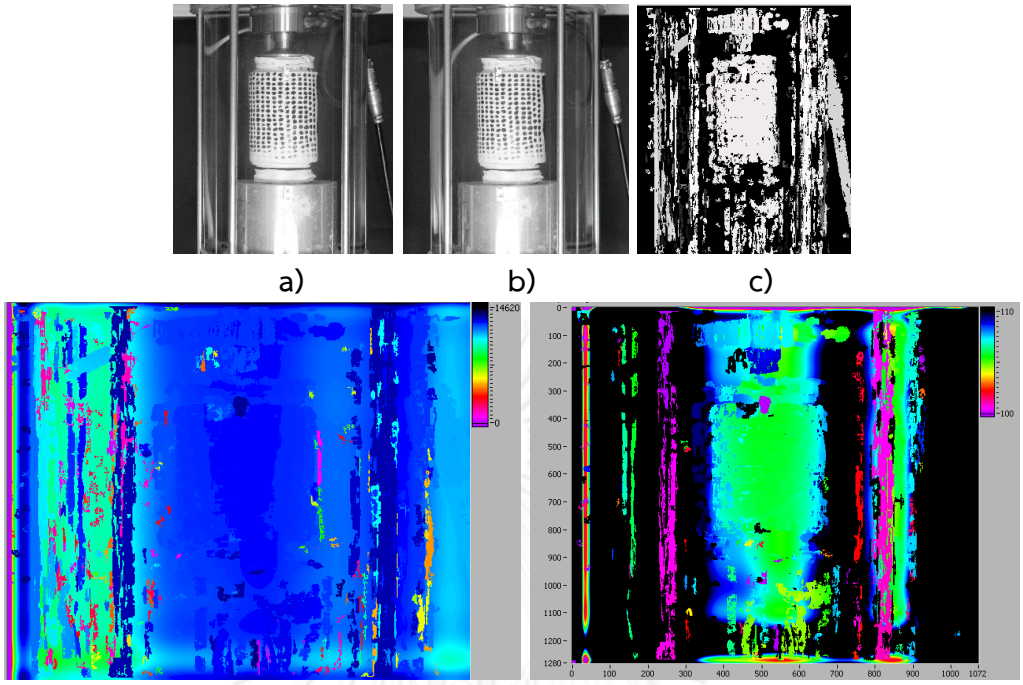

a) b) c)

d) e)

Figure 5.2.35 Binocular stereo vision data 5 a) left image b) right image c) disparity image d) disparity map e) depth map

F. Picture 5

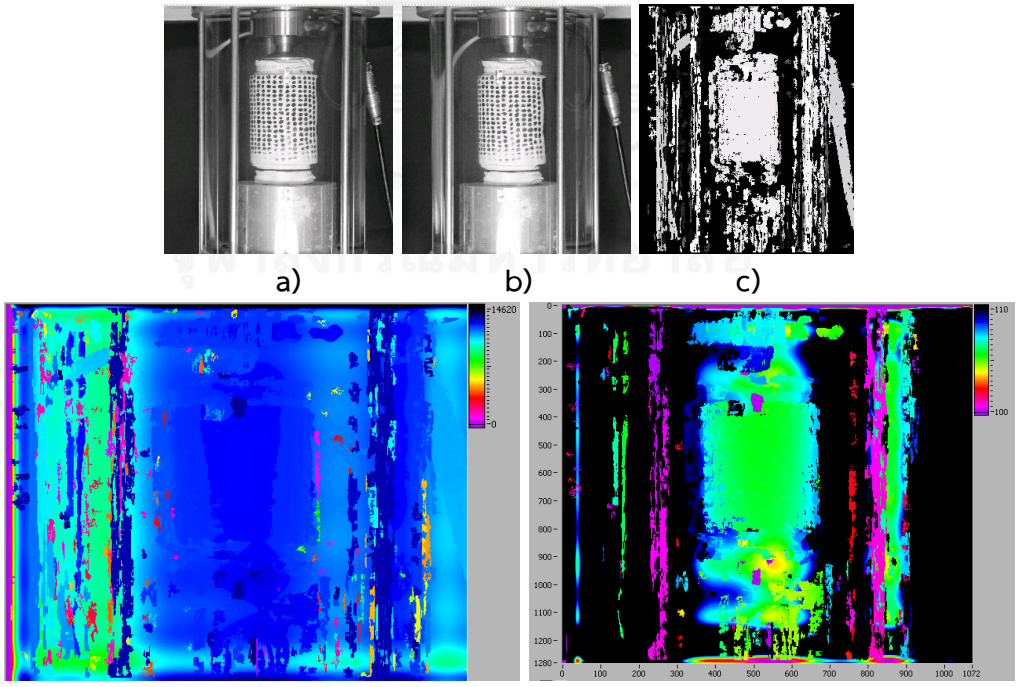

a) b) c)

d) e)

Figure 5.2.36 Binocular stereo vision data 6 (a) left image (b) right image (c) disparity image (d) disparity map (e) depth map

G. Picture 6

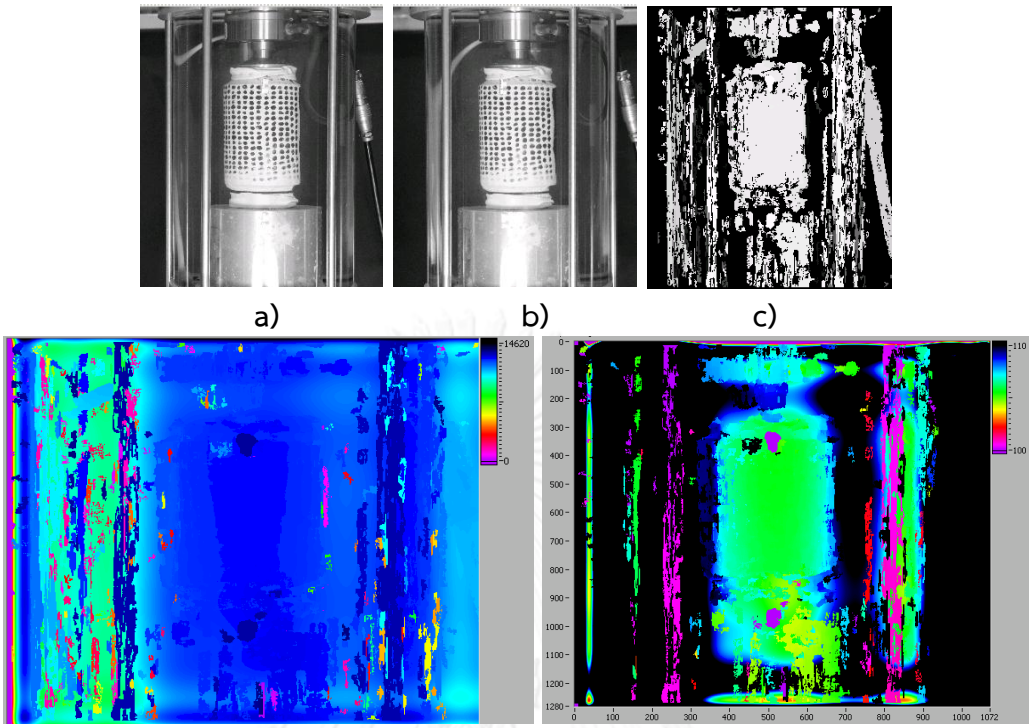

a) b) c)

d) e)

Figure 5.2.37 Binocular stereo vision data 7 a) left image b) right image c) disparity image d) disparity map e) depth map

Table 5.2.8 Results of Trail 5 when the change of volume was obtained

Steps	Patch Size	Change in Volume from Image Processing (cc)	Change in Volume from Burette (cc)	%error
0-1	53	15.63	16.93	-8.03
1-2	59	30.52	30.88	-1.16
2-3	36	2.78	2.85	-2.47
3-4	23	4.11	4.04	1.55
4-5	42	9.86	10.77	-8.86
5-6	21	4.55	4.17	8.77

Trial 6

A. Picture 0

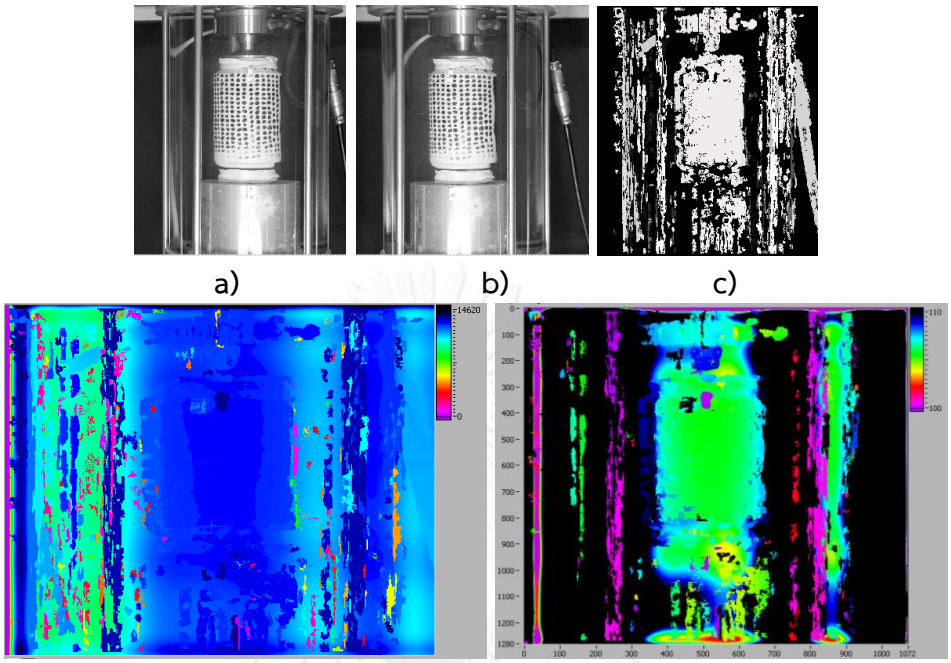

a) b) c)

d) e)

Figure 5.2.38 Binocular stereo vision data 1 a) left image b) right image c) disparity image d) disparity map e) depth map

B. Picture 1

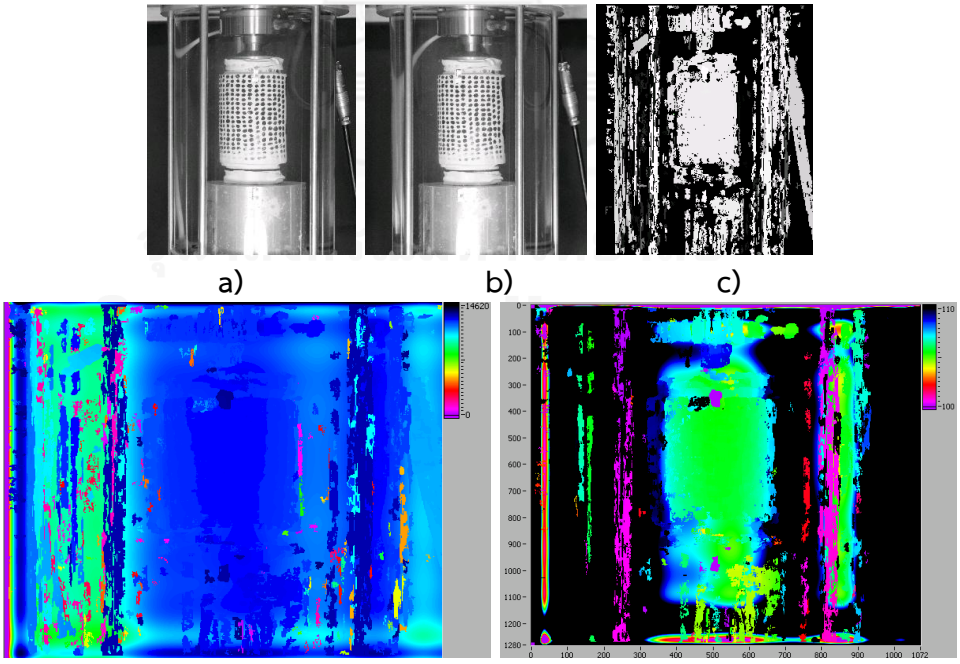

a) b) c)

d) e)

Figure 5.2.39 Binocular stereo vision data 2 a) left image b) right image c) disparity image d) disparity map e) depth map

C. Picture 2

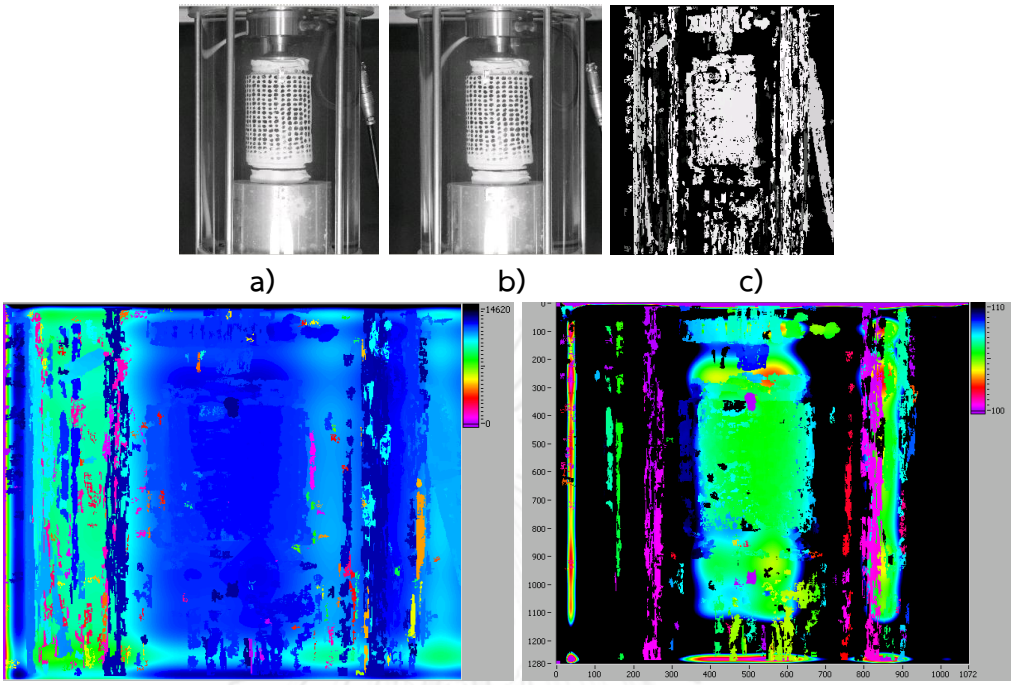

a) b) c)

d) e)

Figure 5.2.40 Binocular stereo vision data 3 a) left image b) right image c) disparity image d) disparity map e) depth map

D. Picture 3

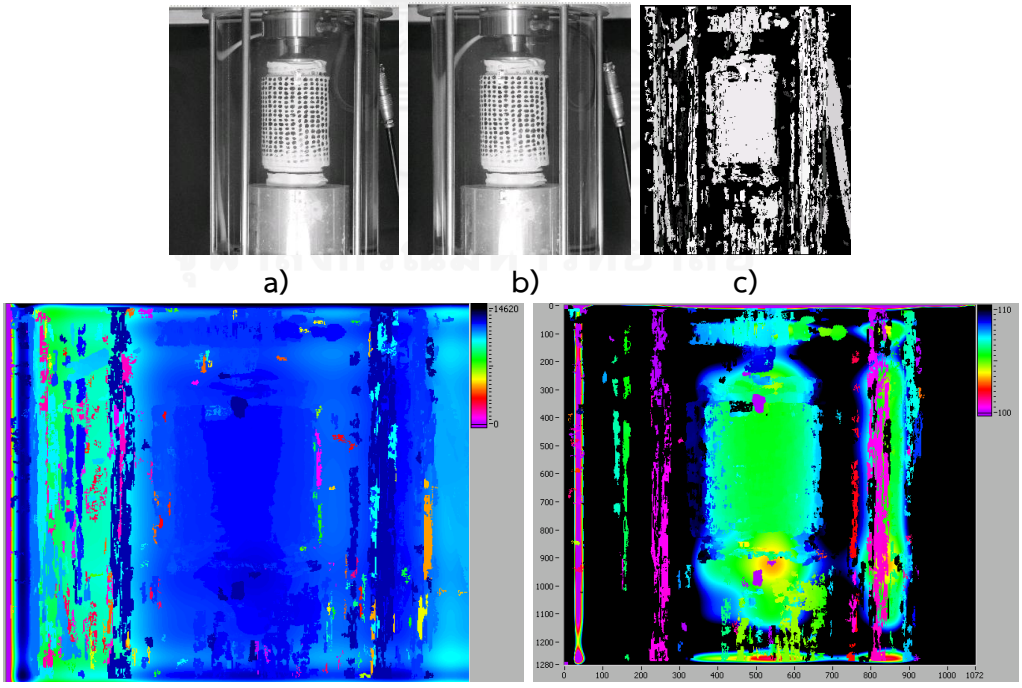

a) b) c)

d) e)

Figure 5.2.41 Binocular stereo vision data 4 a) left image b) right image c) disparity image d) disparity map e) depth map

E. Picture 4

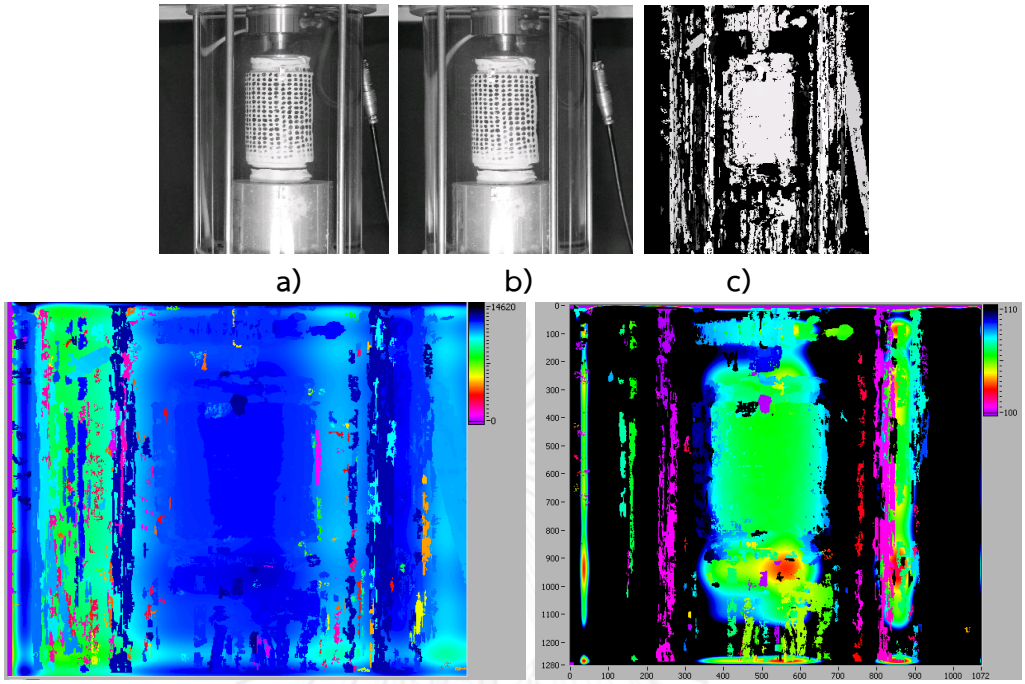

a) b) c)

d) e)

Figure 5.2.42 Binocular stereo vision data 5 a) left image b) right image c) disparity image d) disparity map e) depth map

F. Picture 5

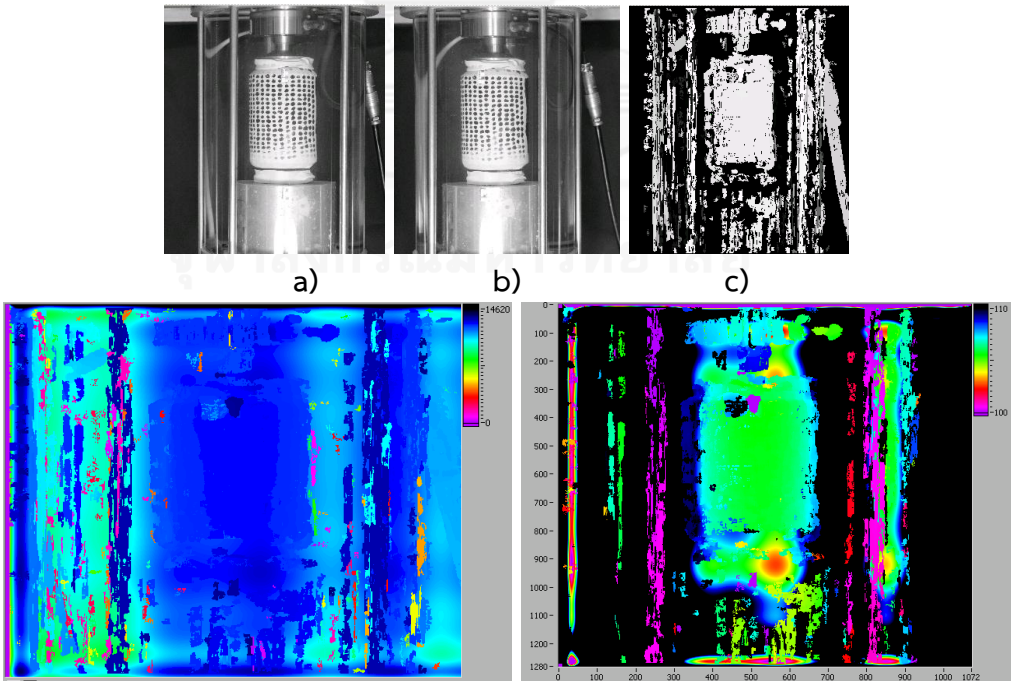

a) b) c)

d) e)

Figure 5.2.43 Binocular stereo vision data 6 a) left image b) right image c) disparity image d) disparity map e) depth map

G. Picture 6

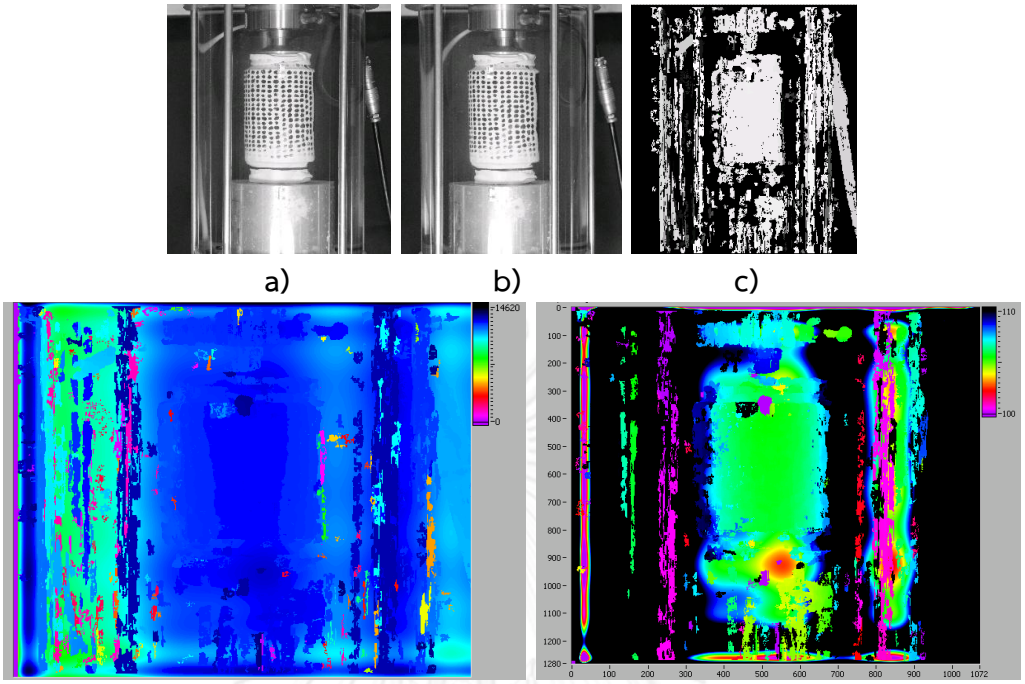

a) b) c)

d) e)

Figure 5.2.44 Binocular stereo vision data 7 a) left image b) right image c) disparity image d) disparity map e) depth map

H. Picture 7

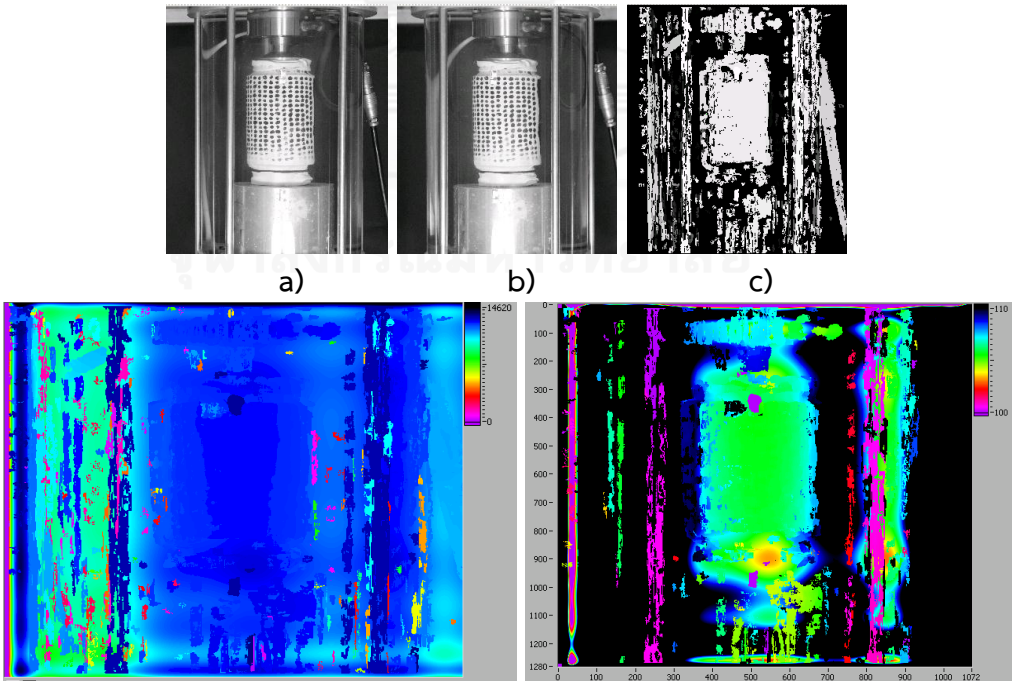

a) b) c)

d) e)

Figure 5.2.45 Binocular stereo vision data 8 a) left image b) right image c) disparity image d) disparity map e) depth map

I. Picture 8

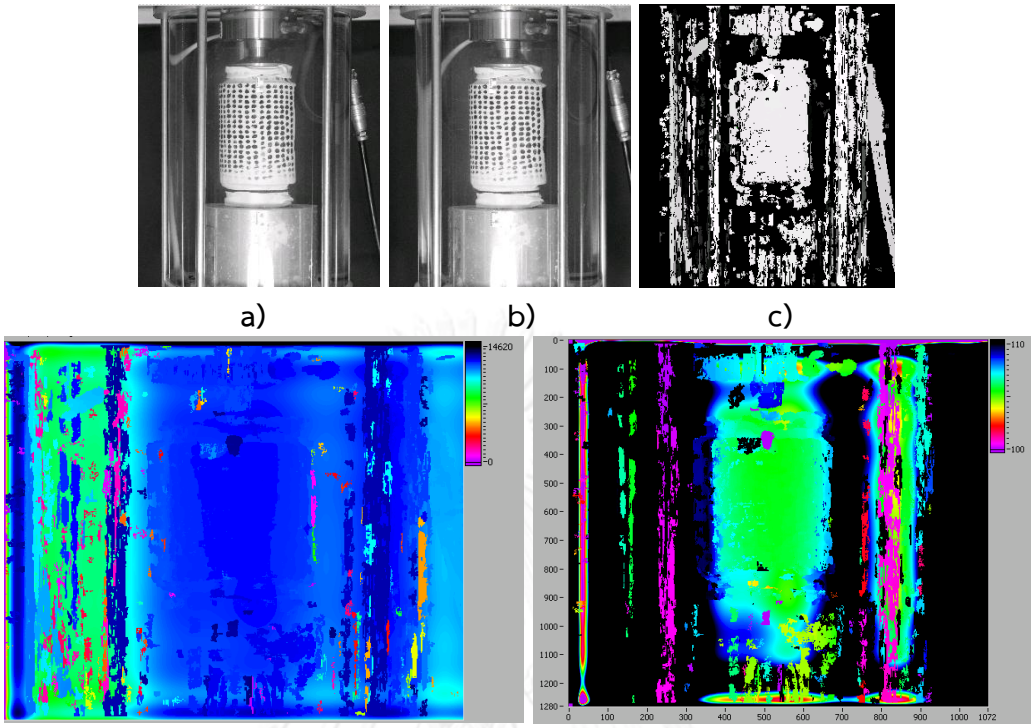

a) b) c)

d) e)

Figure 5.2.46 Binocular stereo vision data 9 a) left image b) right image c) disparity image d) disparity map e) depth map

Table 5.2.9 Results of Trail 6 when the change of volume was obtained

Steps	Patch Size	Change in Volume from Image Processing (cc)	Change in Volume from Burette (cc)	%error
0to1	44	14.354	15.53	-7.88
1to3	56	12.01	11.97	0.30
3to4	29	40.89	40.88	0.02
4to5	60	30.48	32.80	-7.32

Table 5.2.10 Results of Trial 6 when the reference image was the image after the test begins

Steps	Patch Size	Volume from Image Processing (cc)	Volume from Burette (cc)	%error
1to2	31	6.32	6.22	1.65
1to4	53	43.22	44.44	-2.78
1to5	54	11.75	11.64	0.88
1to6	55	9.79	9.94	-1.51
1to7	55	10.99	10.12	8.23
1to8	49	10.95	10.12	7.86

Validation for Depth Reading under Tilting Planes

A. Profile at the center

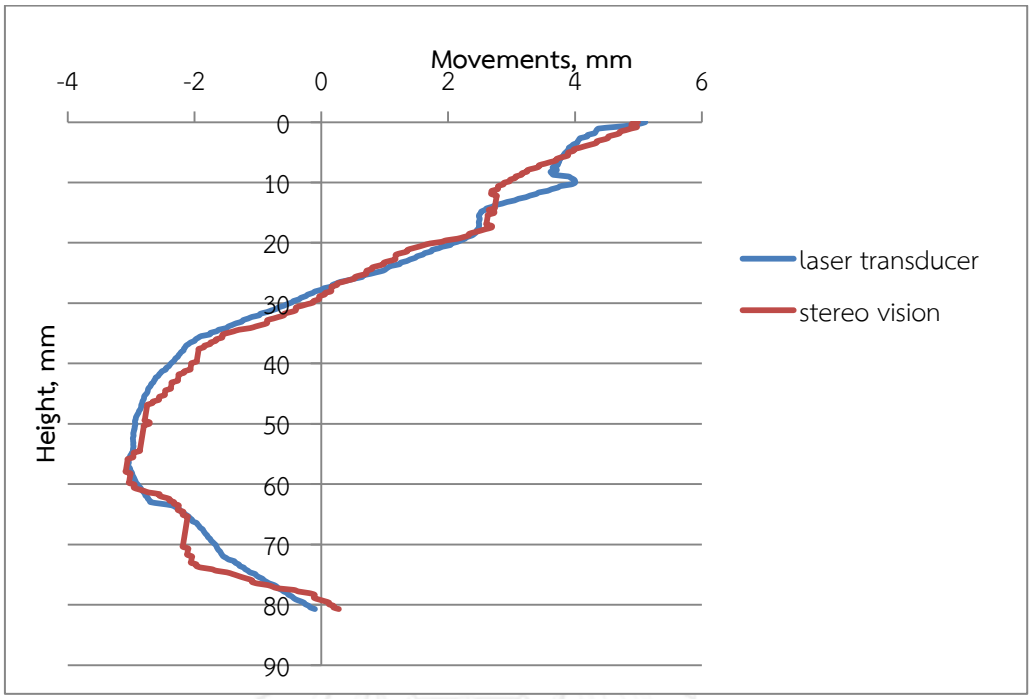

Figure 5.2.47 Profile at the center: Trial 1

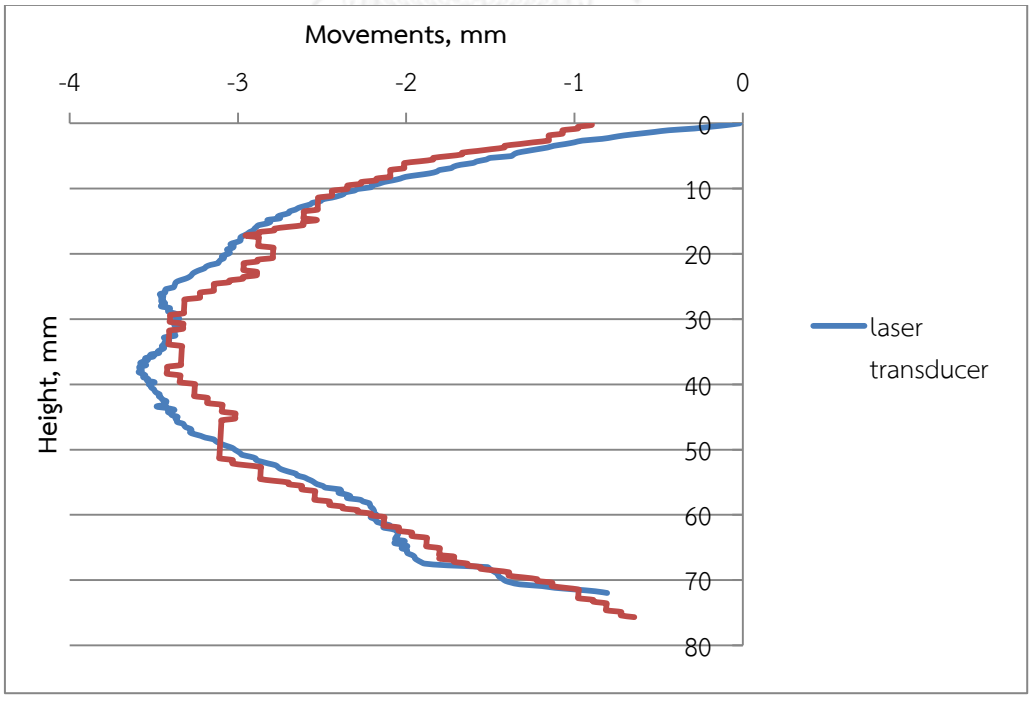

Figure 5.2.48 Profile at the center: Trial 2

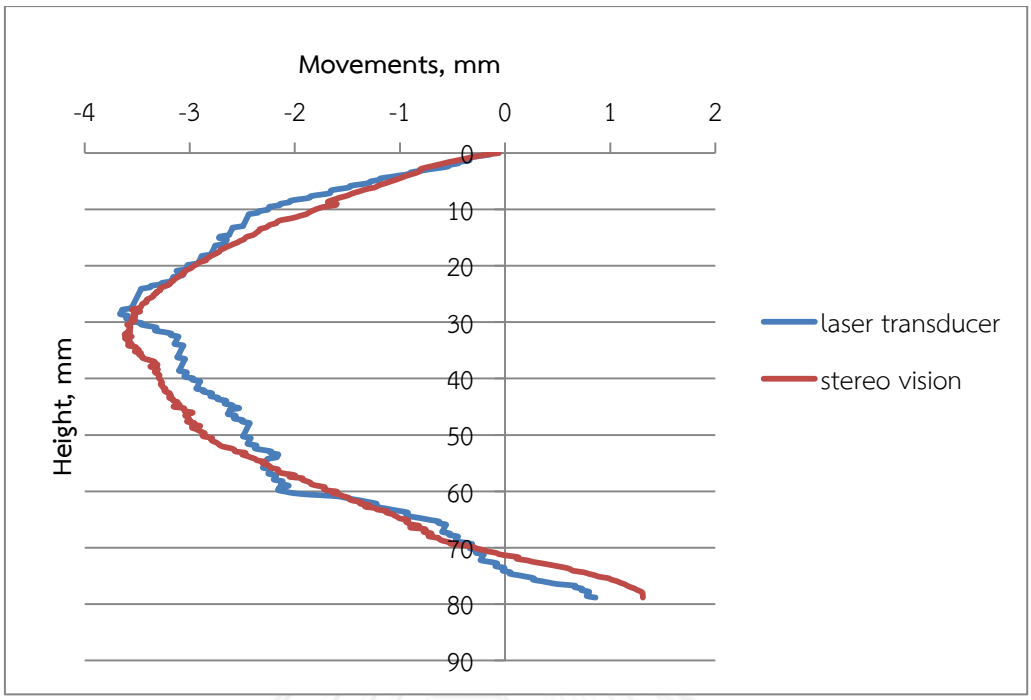

Figure 5.2.49 Profile at the center: Trial 3

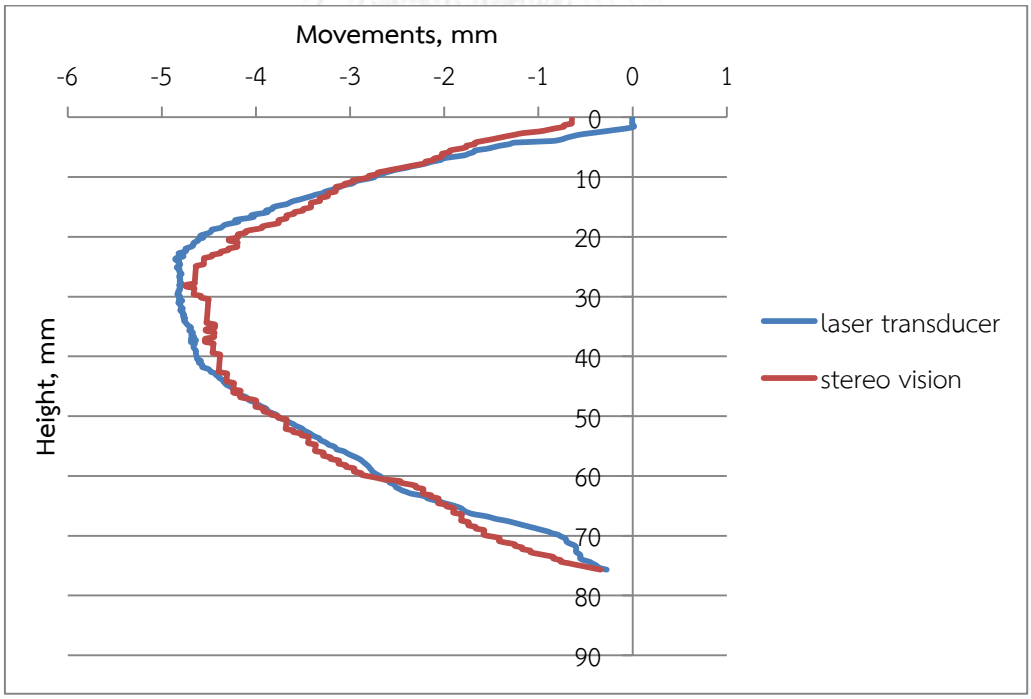

Figure 5.2.50 Profile at the center: Trial 4

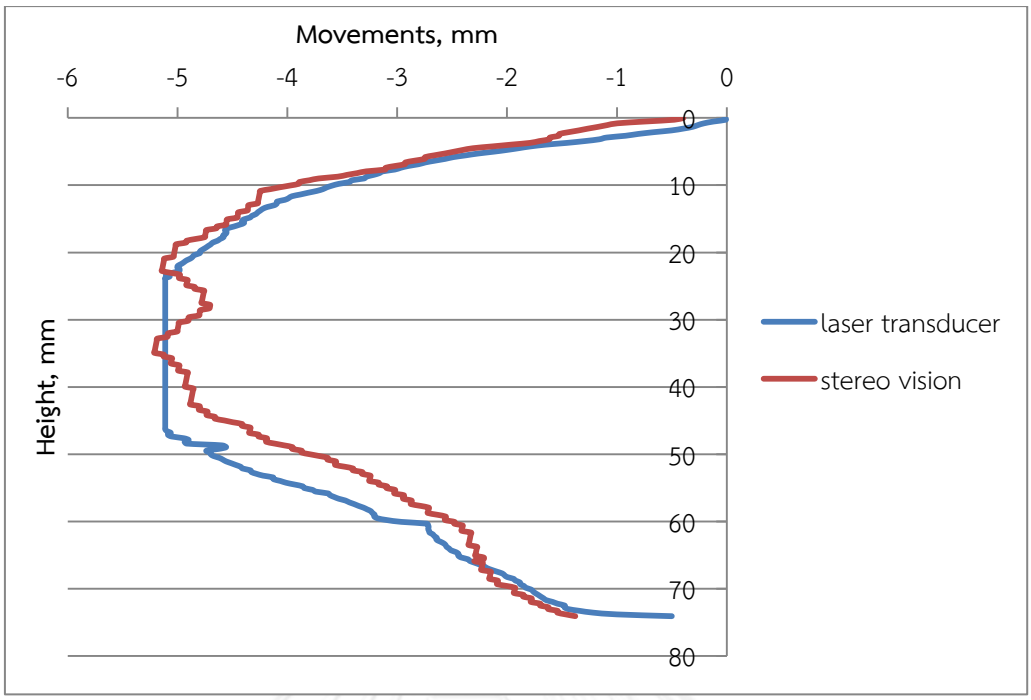

Figure 5.2.51 Profile at the center: Trial 5

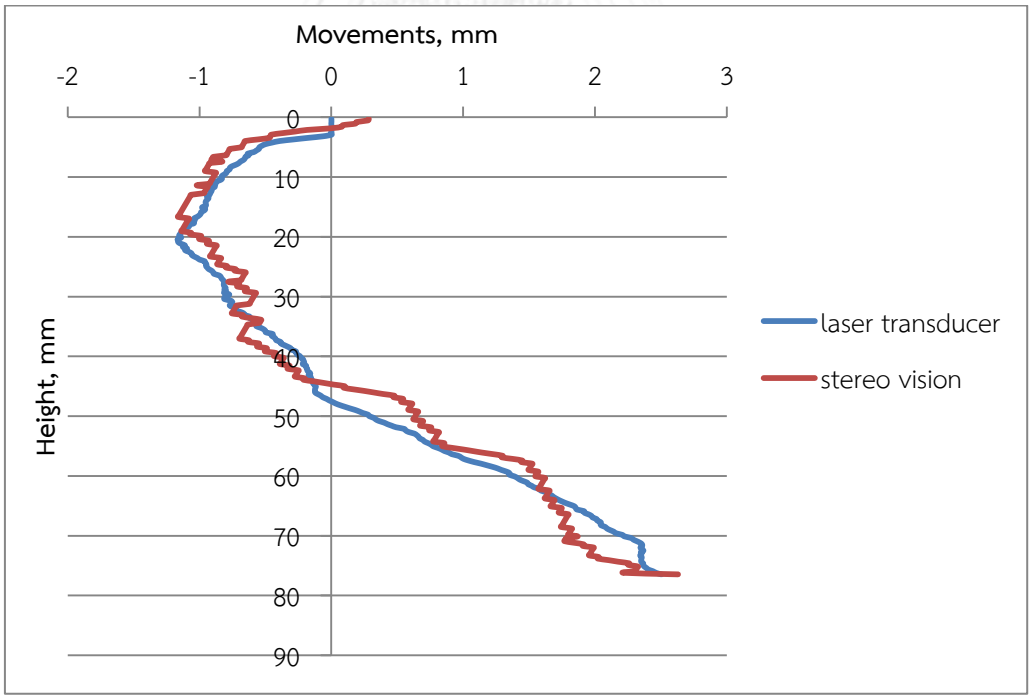

Figure 5.2.52 Profile at the center: Trial 6

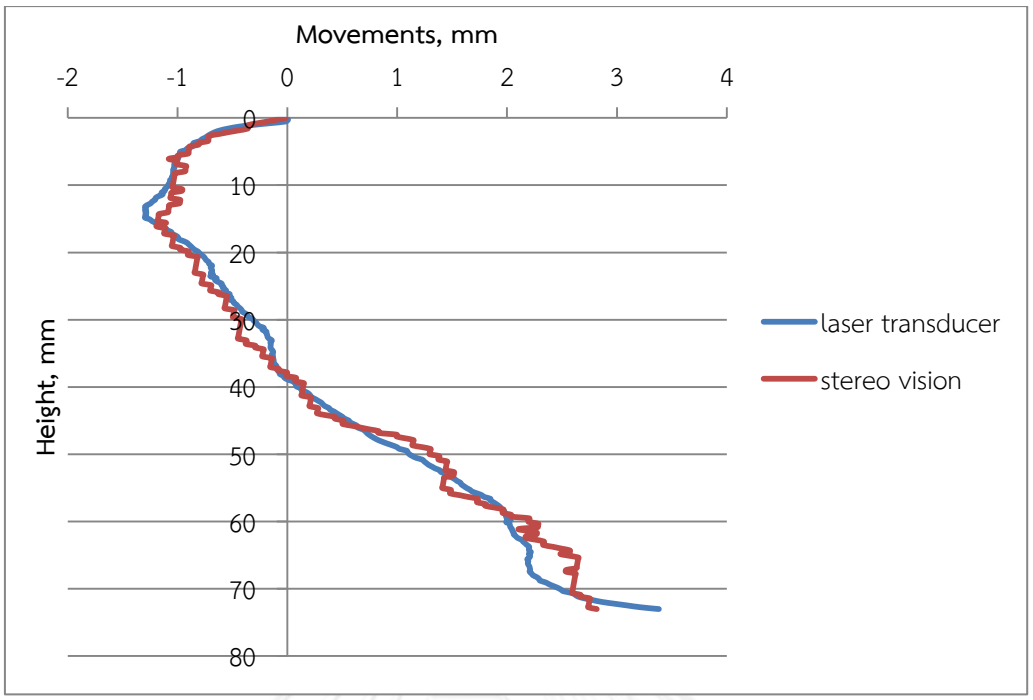

Figure 5.2.53 Profile at the center: Trial 7

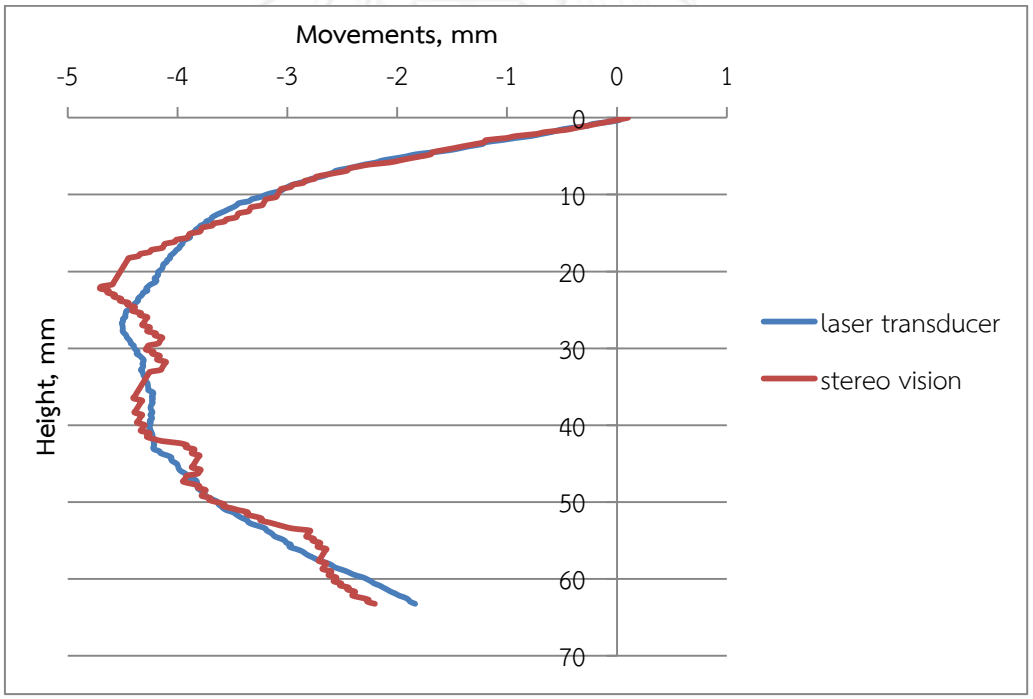

Figure 5.2.54 Profile at the center: Trial 8

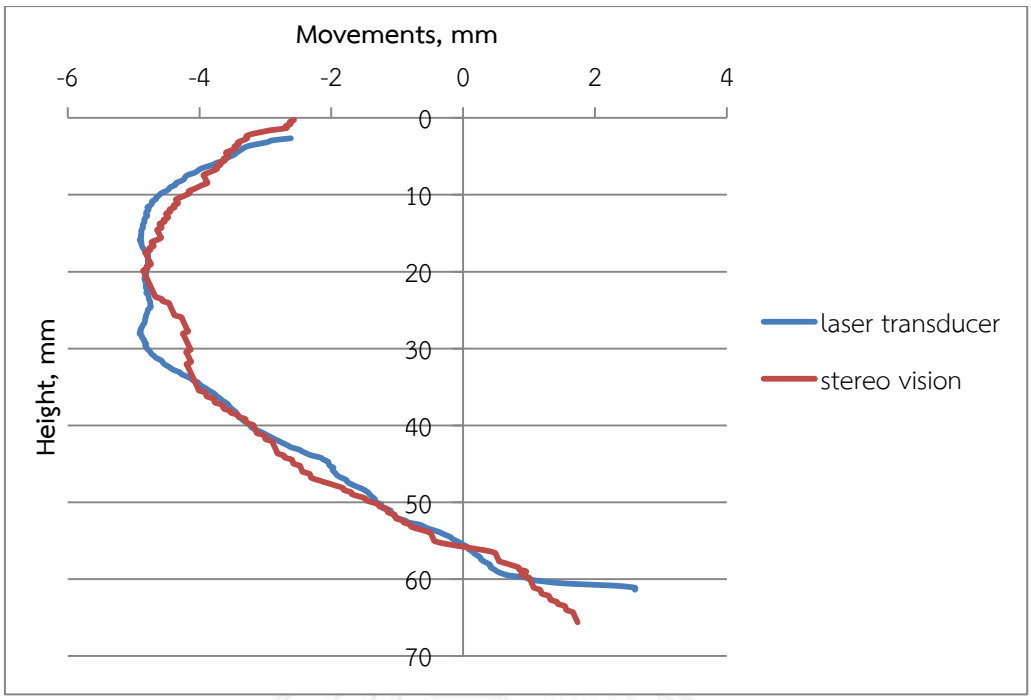

Figure 5.2.55 Profile at the center: Trial 9

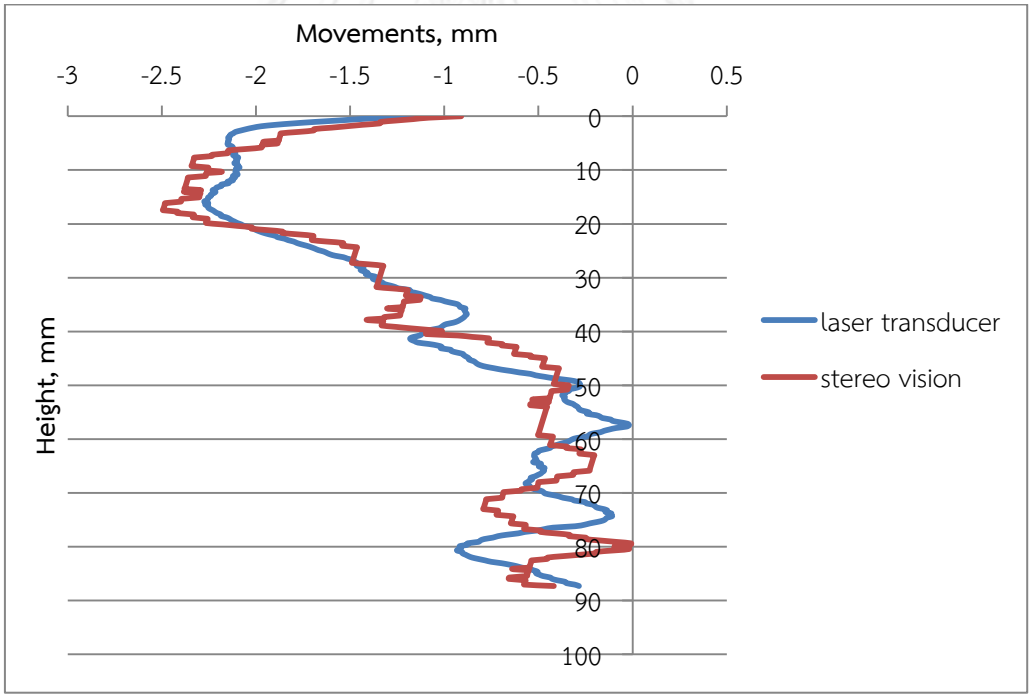

Figure 5.2.56 Profile at the center: Trial 10

B. Profile at 40 ° from the center

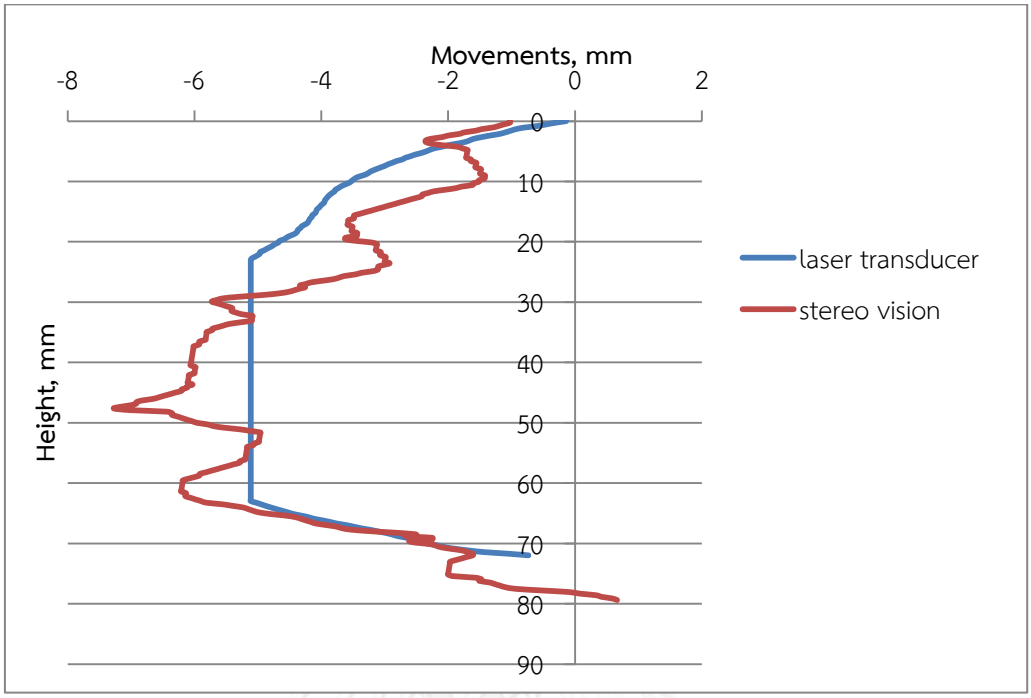

a)

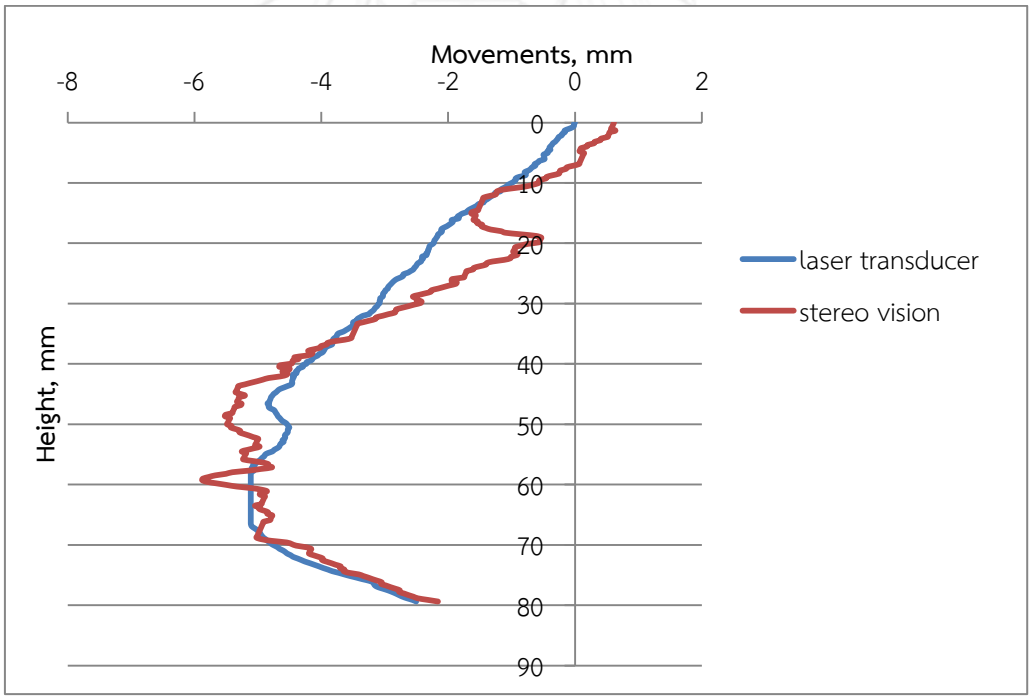

b)

Figure 5.2.57 Profile at 40° from the center: Trial 1 a) Left b) Right

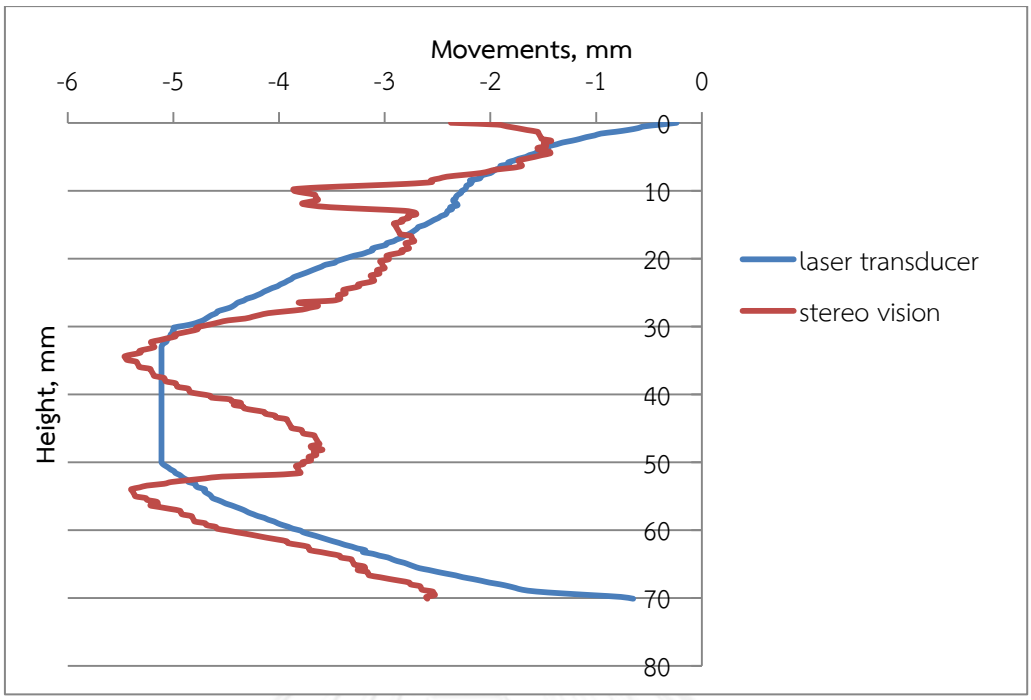

a)

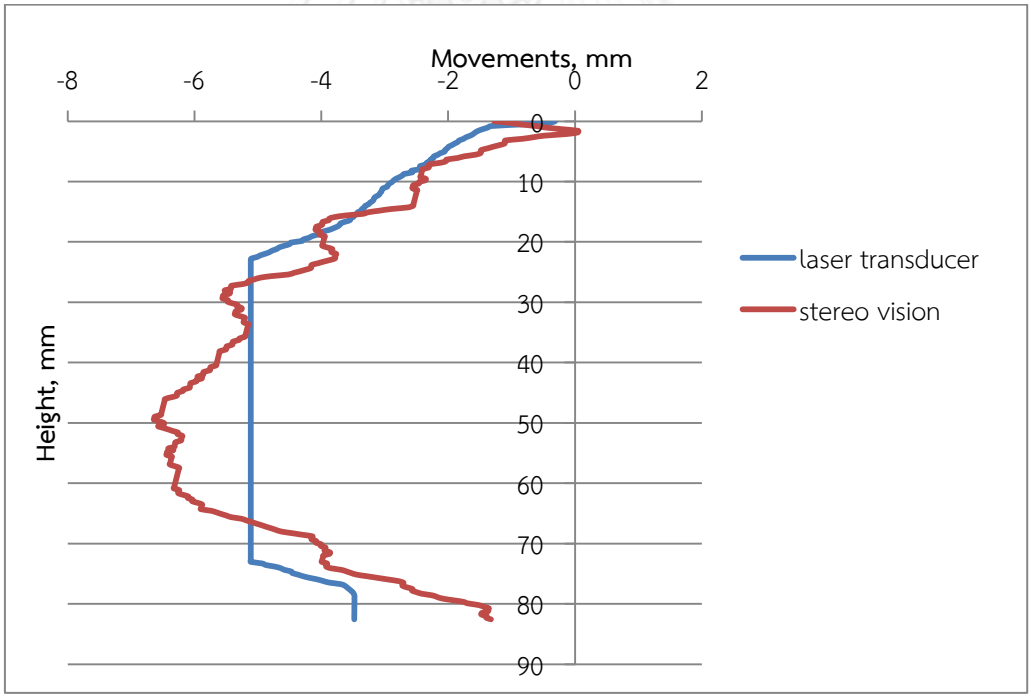

b)

Figure 5.2.58 Profile at 40° from the center: Trial 2 a) Left b) Right

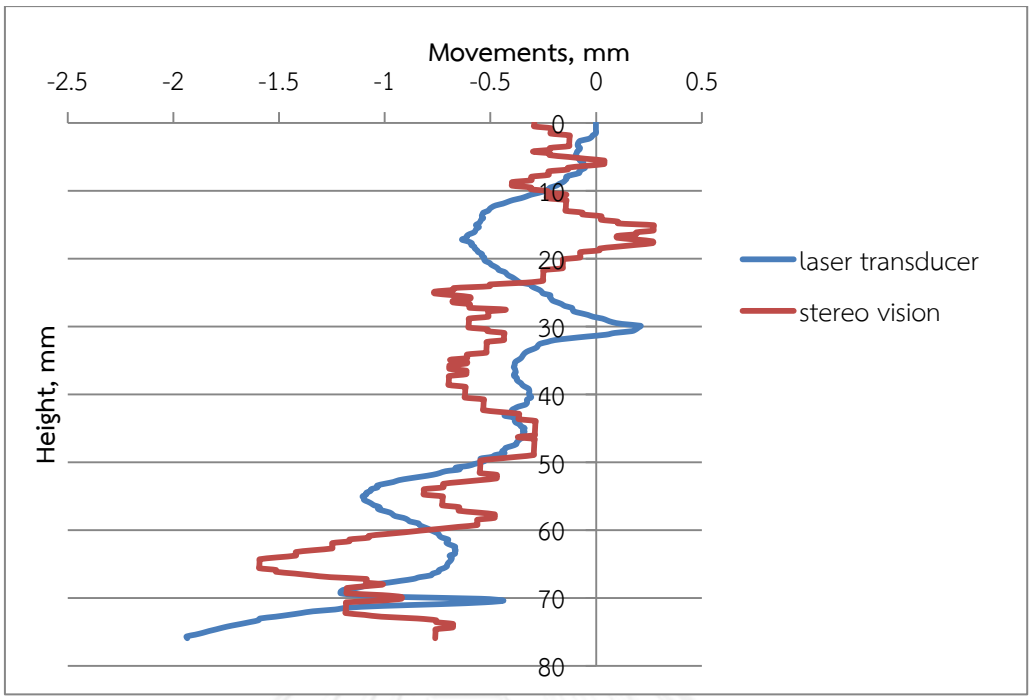

a)

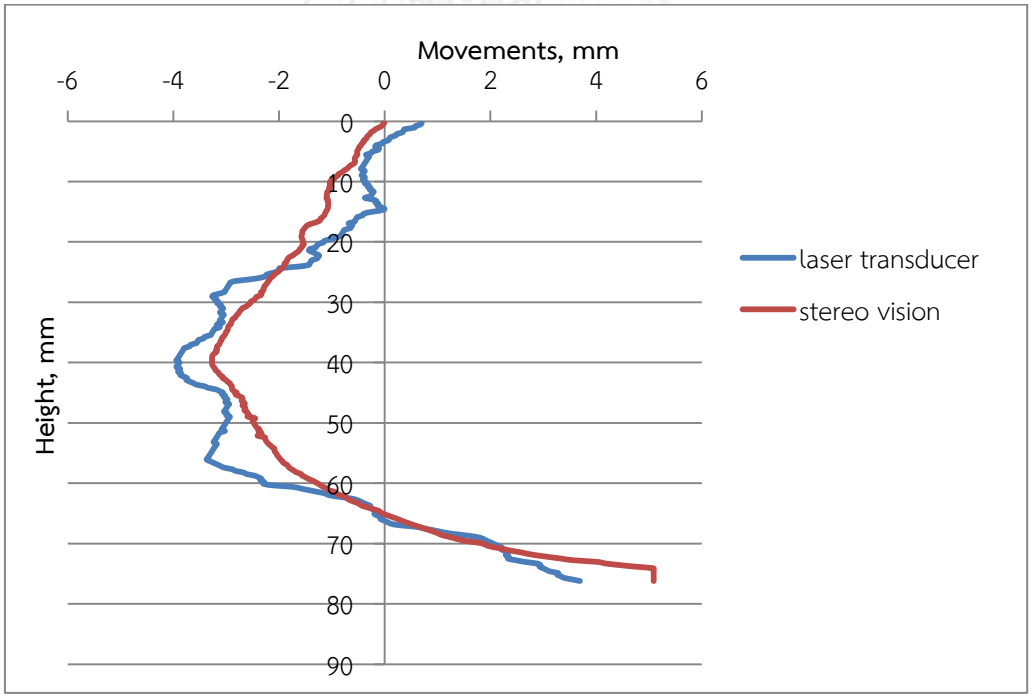

b)

Figure 5.2.59 Profile at 40° from the center: Trial 3 a) Left b) Right

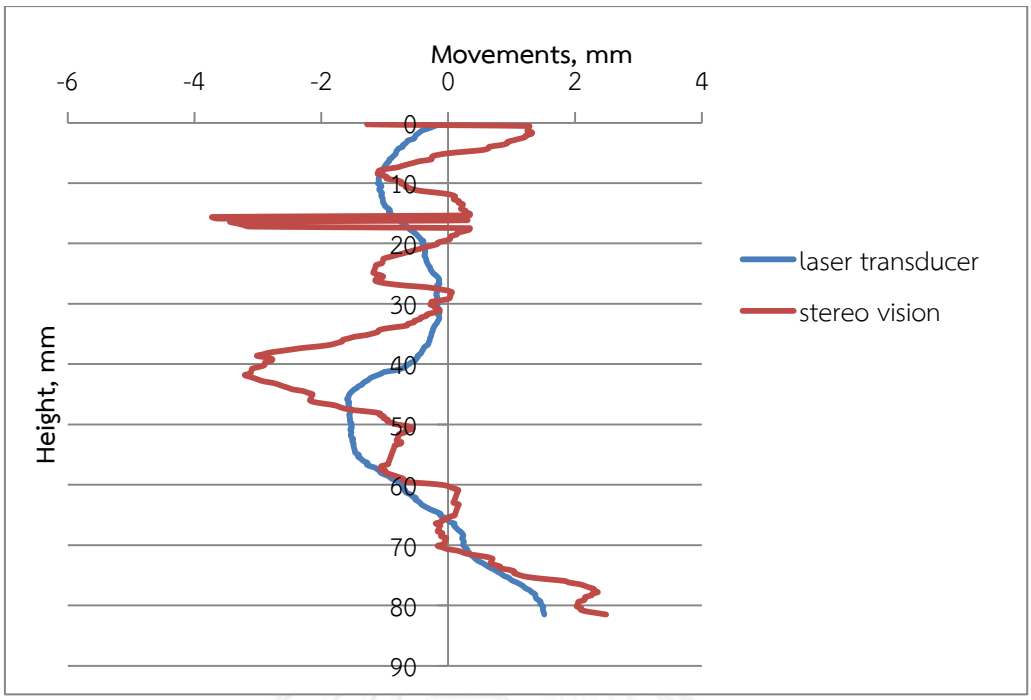

a)

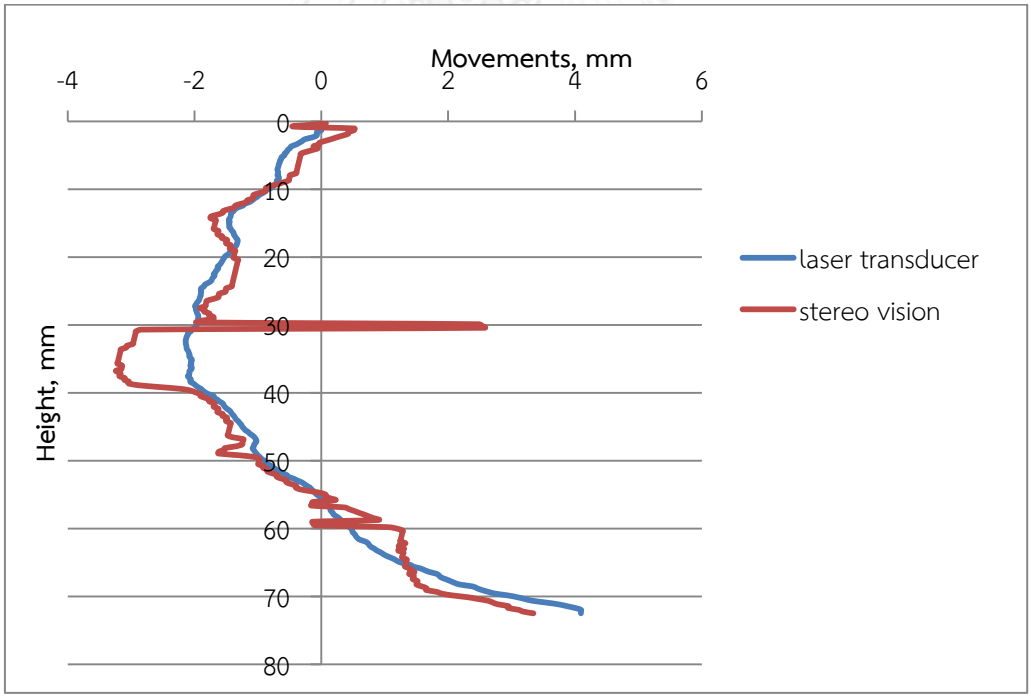

b)

Figure 5.2.60 Profile at 40° from the center: Trial 4 a) Left b) Right

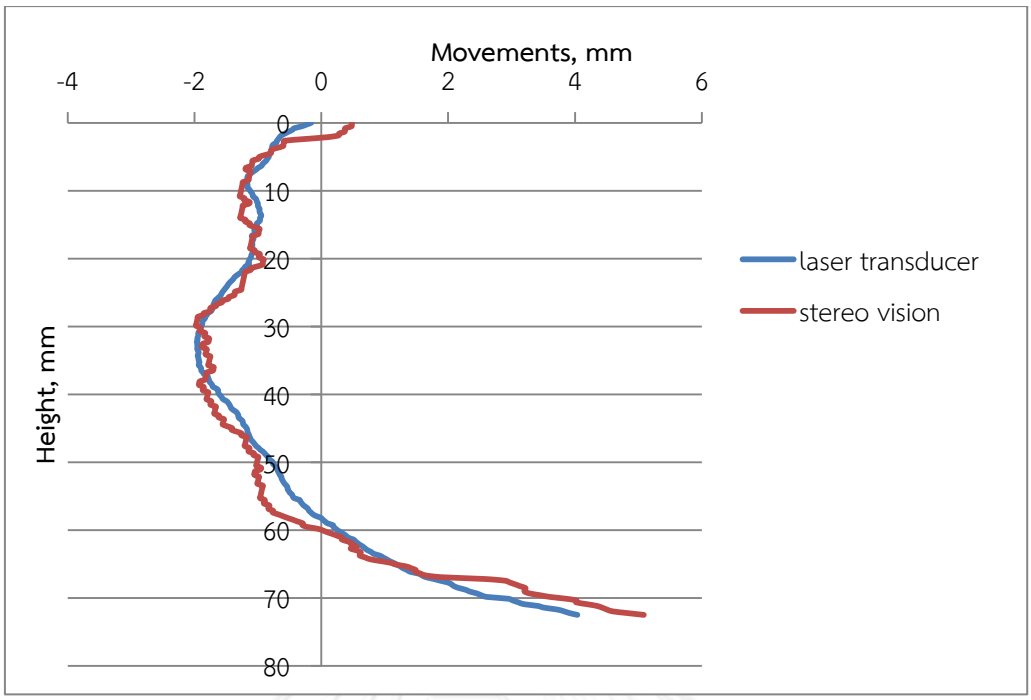

a)

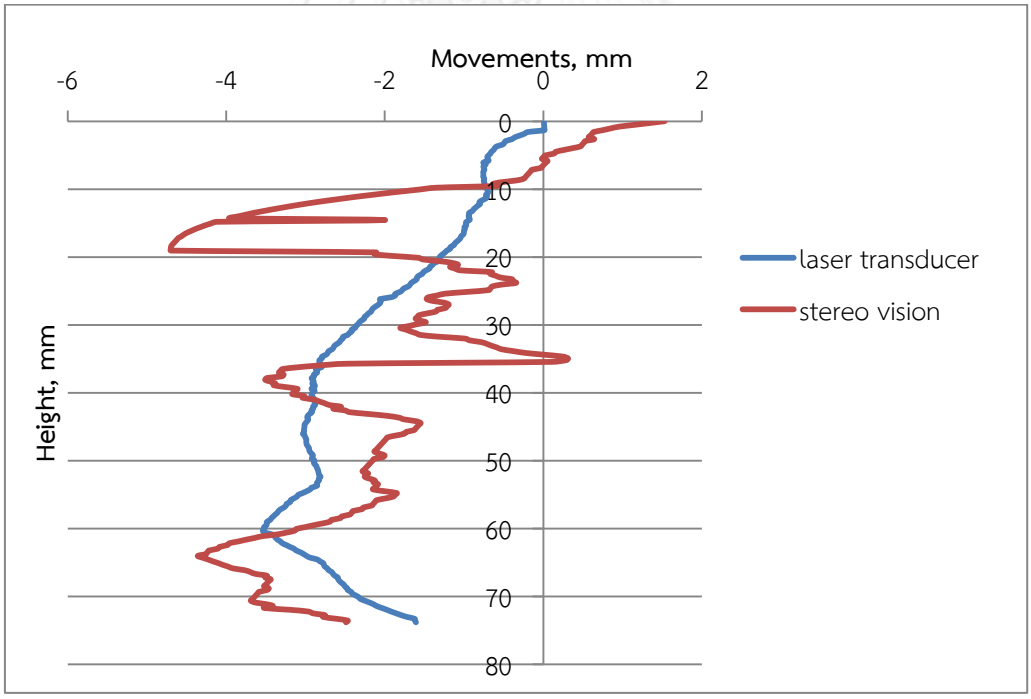

b)

Figure 5.2.61 Profile at 40° from the center: Trial 5 a) Left b) Right

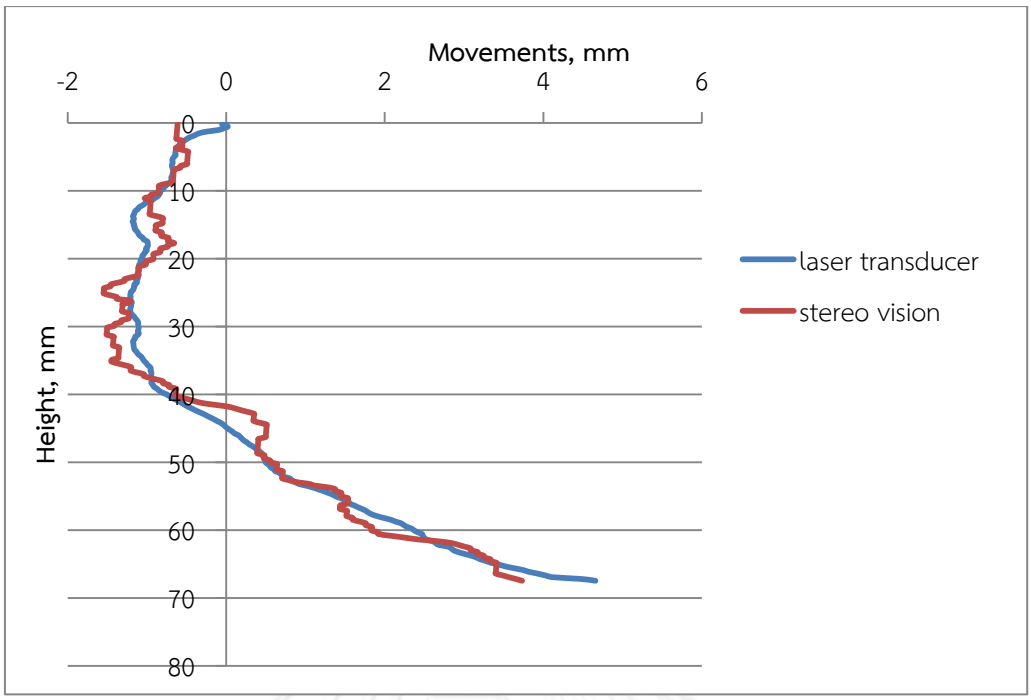

a)

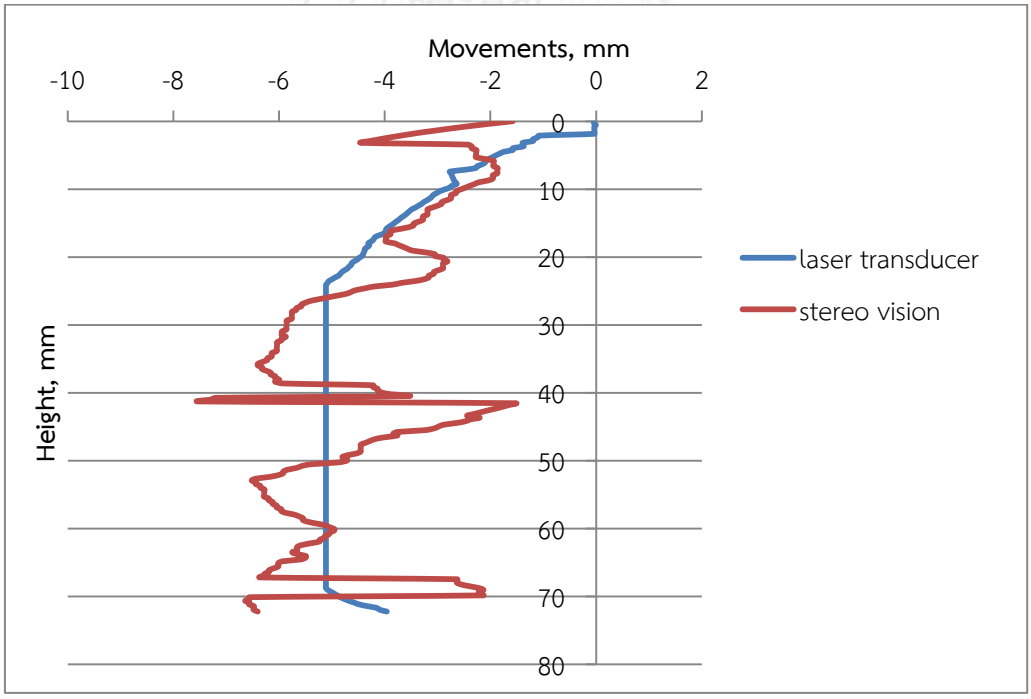

b)

Figure 5.2.62 Profile at 40° from the center: Trial 6 a) Left b) Right

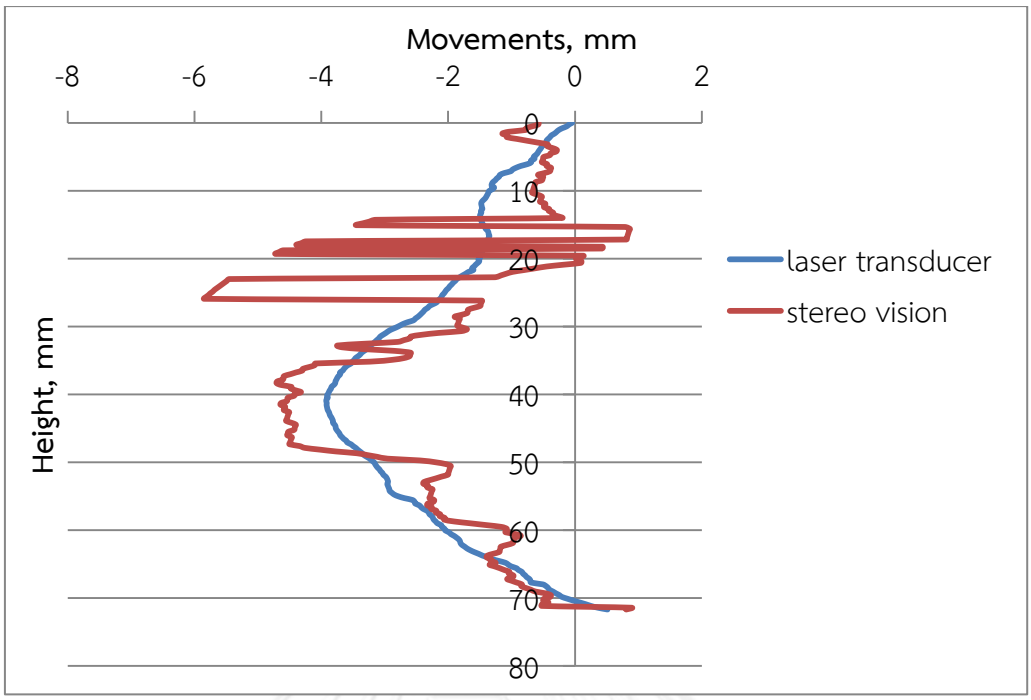

a)

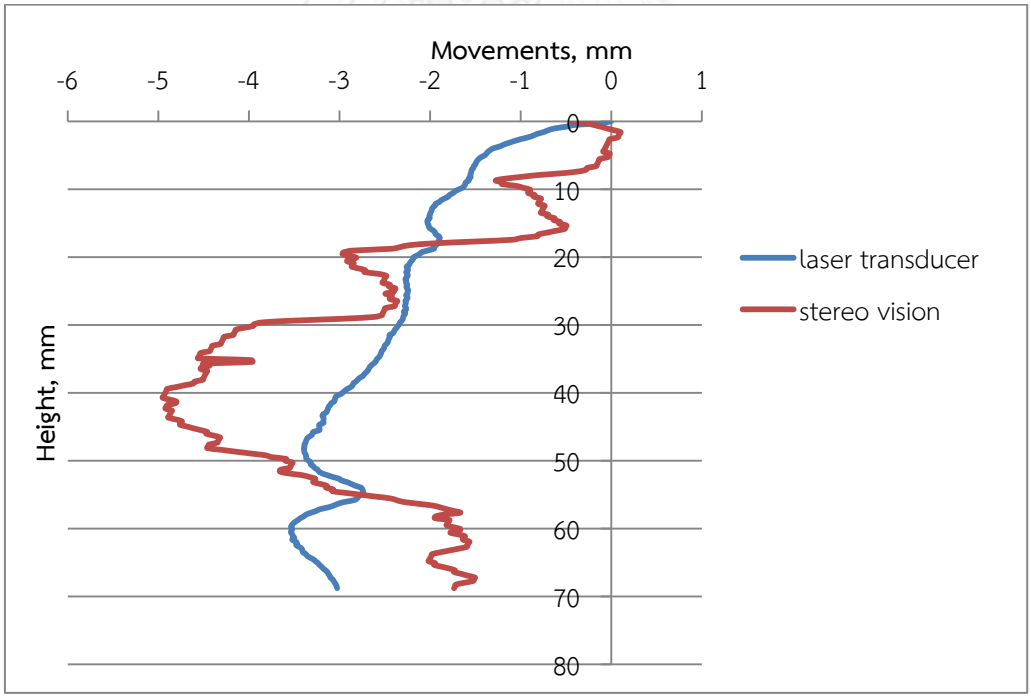

b)

Figure 5.2.63 Profile at 40° from the center: Trial 7 a) Left b) Right

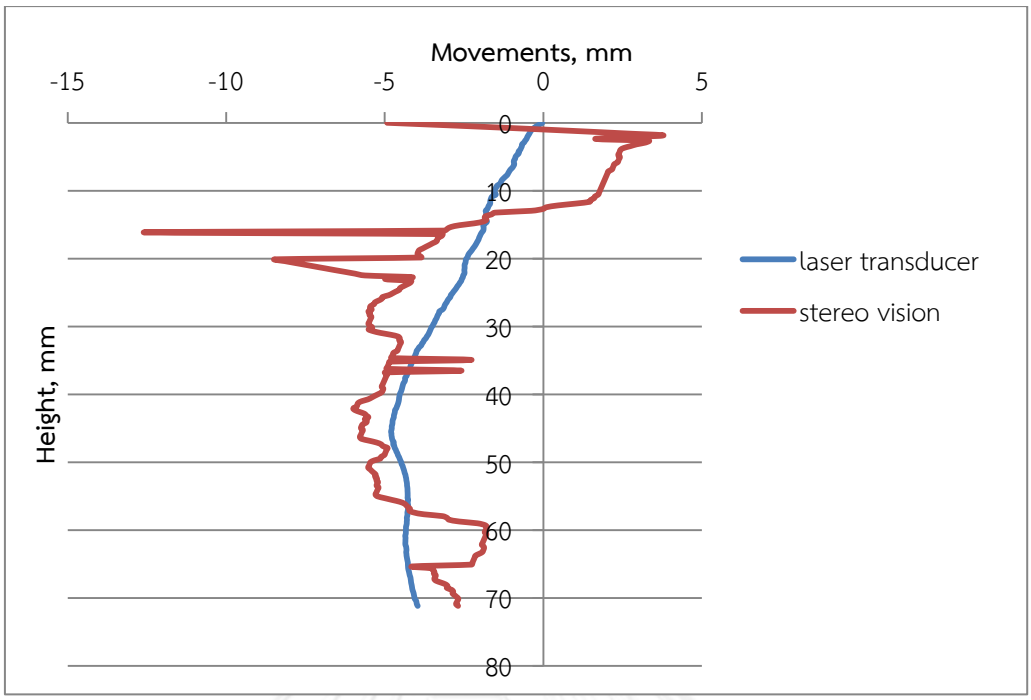

a)

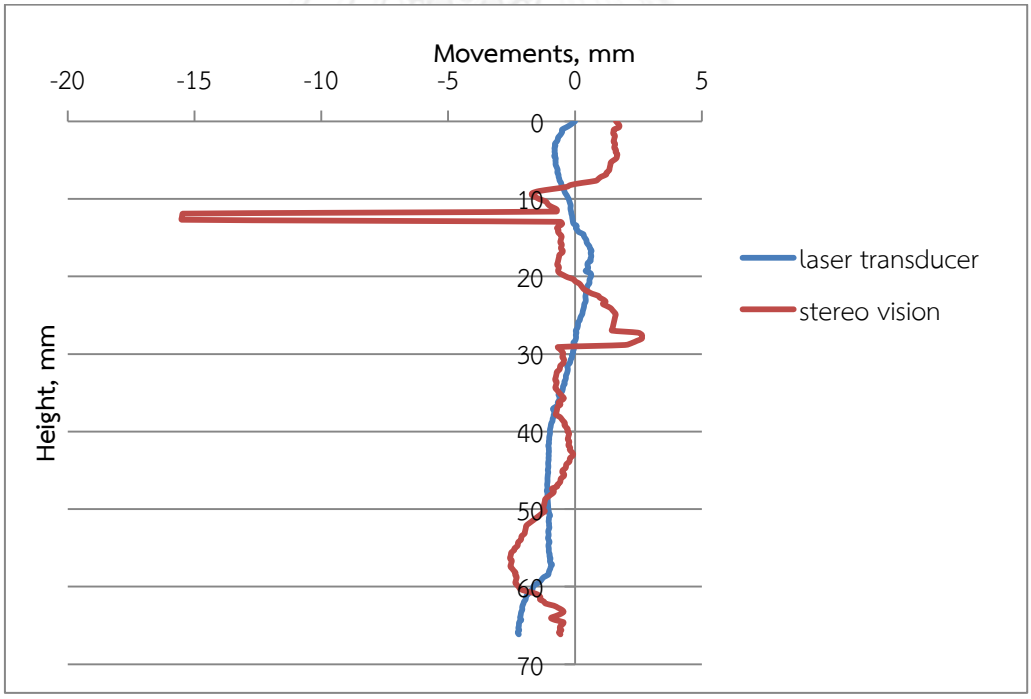

b)

Figure 5.2.64 Profile at 40° from the center: Trial 8 a) Left b) Right

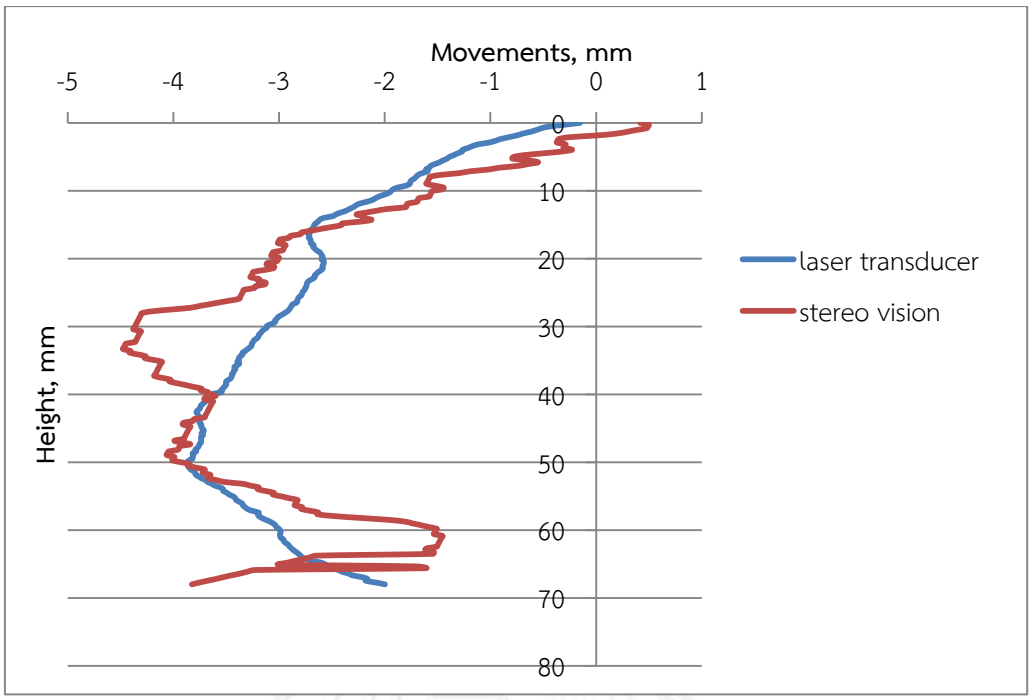

a)

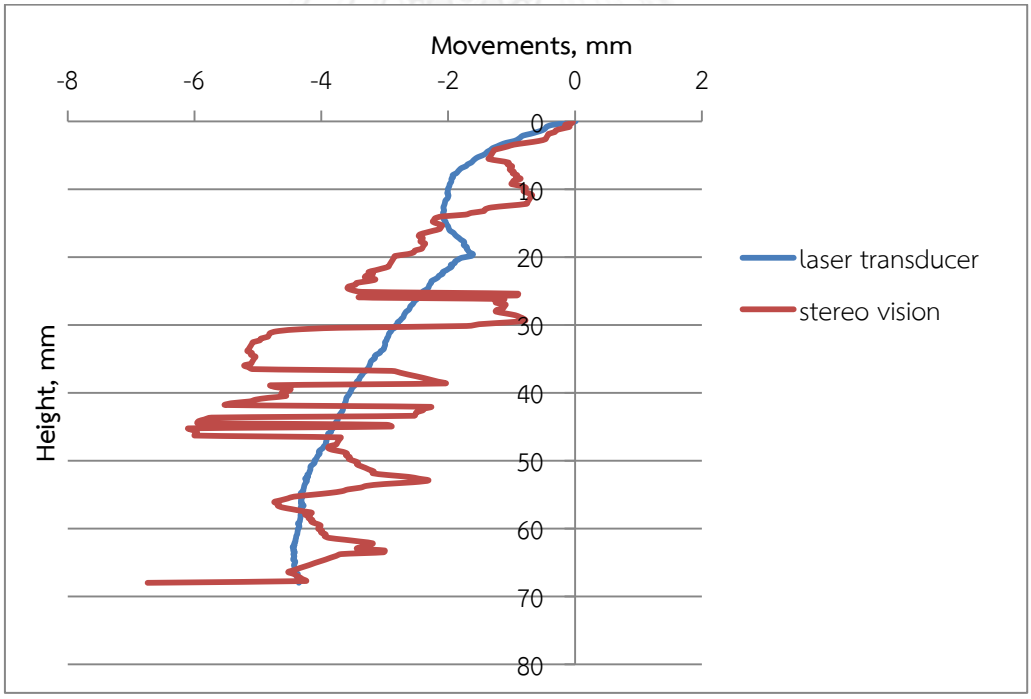

b)

Figure 5.2.65 Profile at 40° from the center: Trial 9 a) Left b) Right

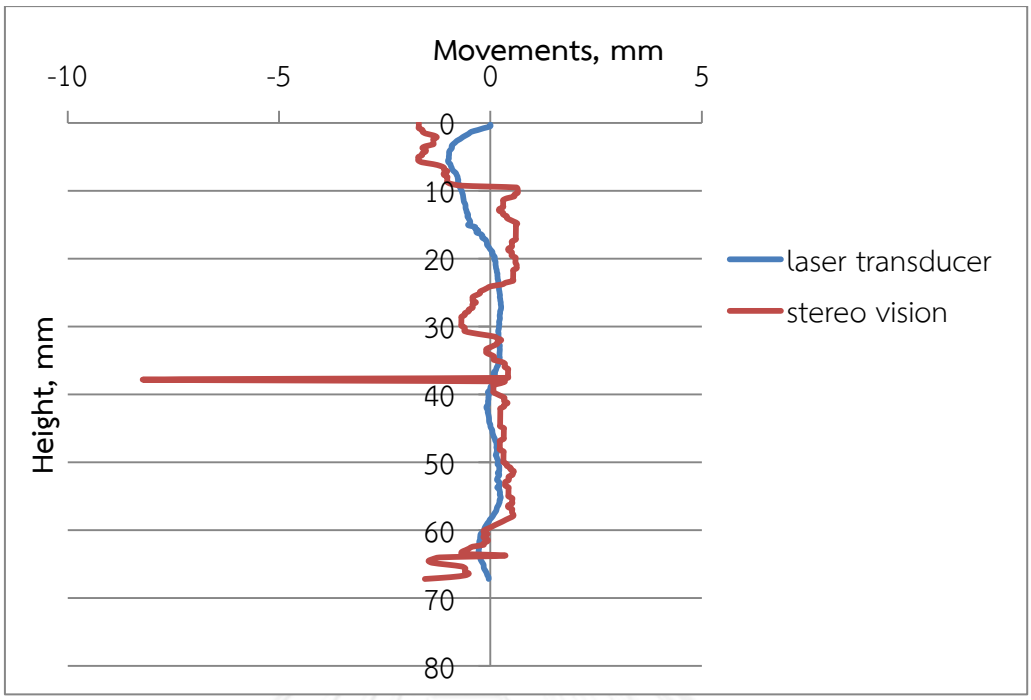

a)

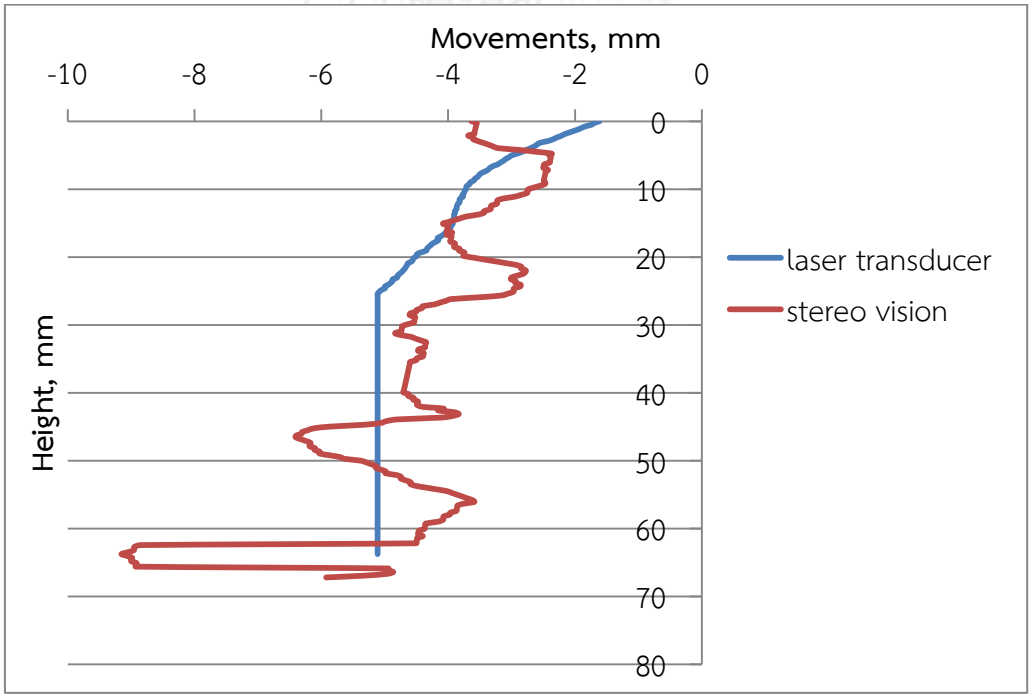

b)

Figure 5.2.66 Profile at 40° from the center: Trial 10 a) Left b) Right

C. Profile at the boundary

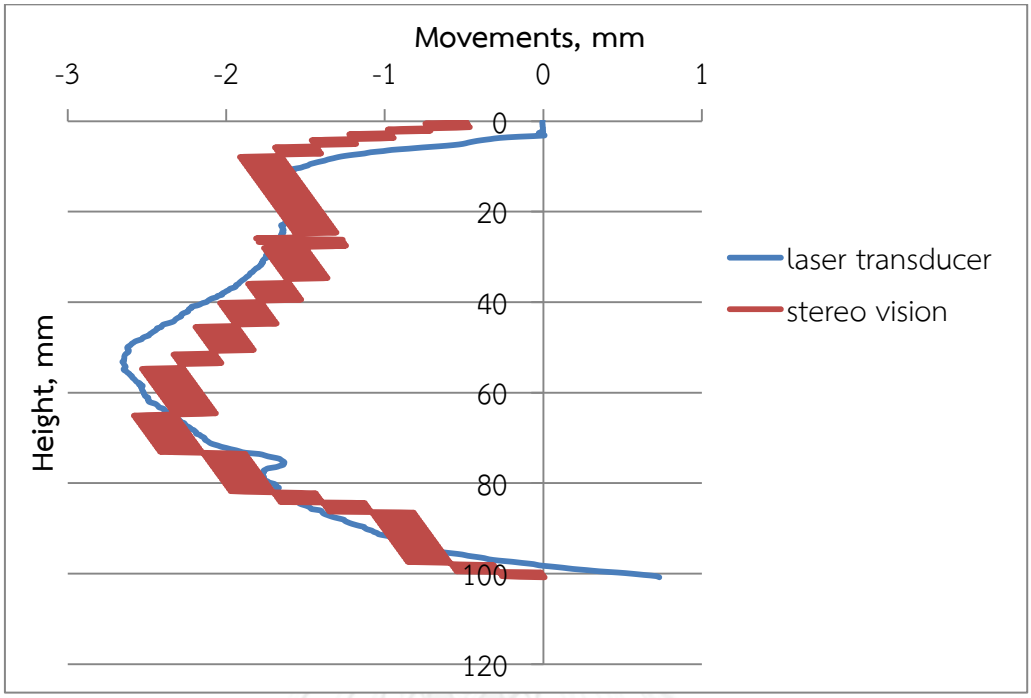

a)

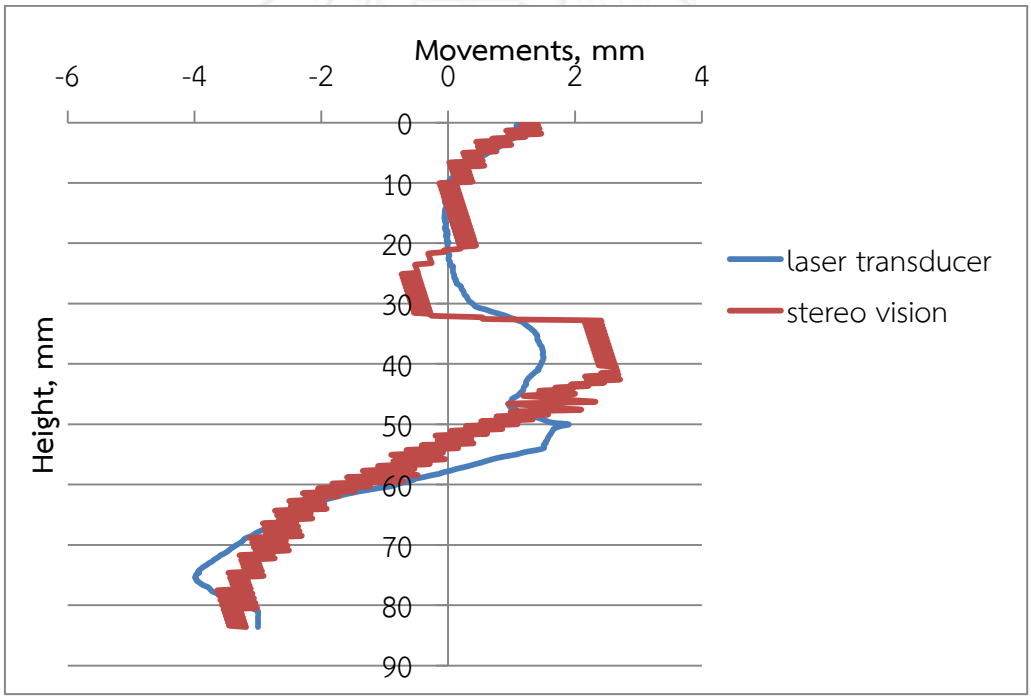

b)

Figure 5.2.67 Profile at boundary: Trial 1 a) Left b) Right

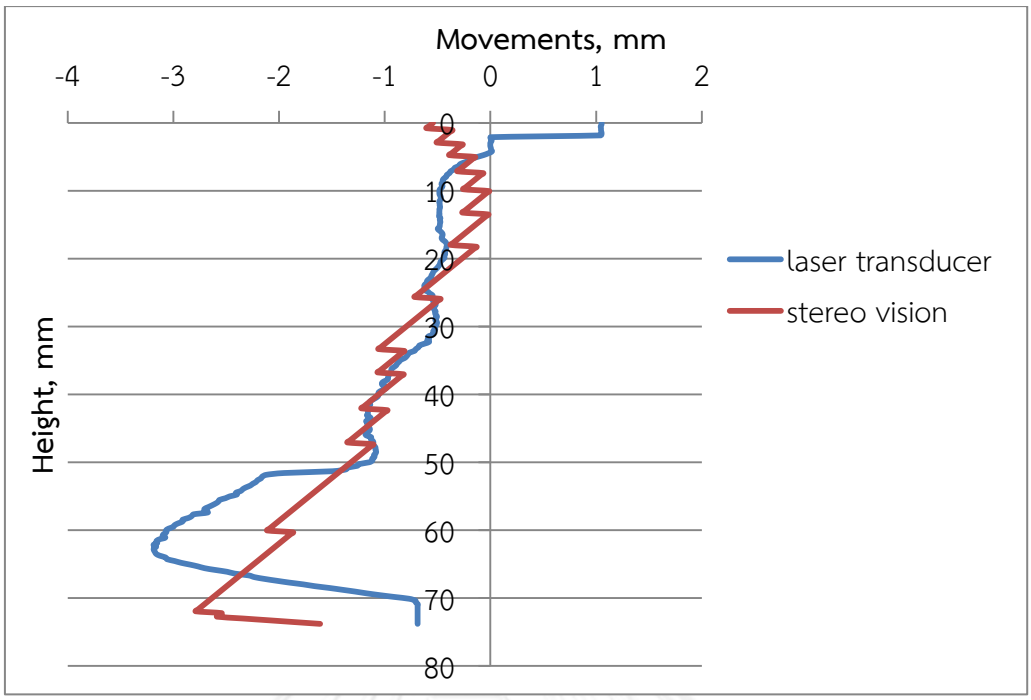

a)

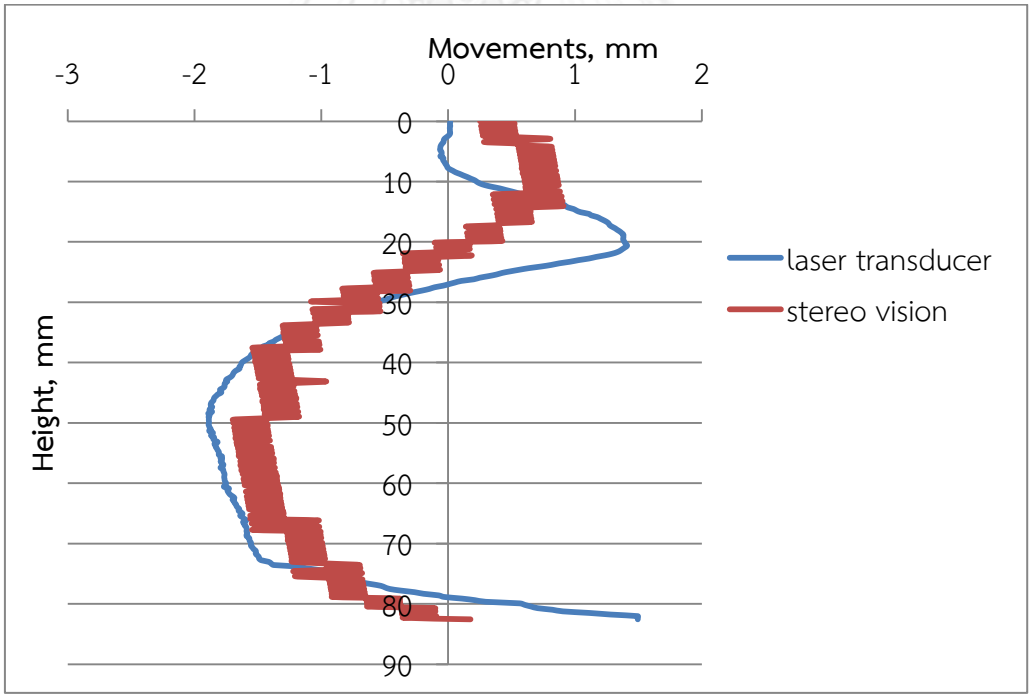

b)

Figure 5.2.68 Profile at boundary: Trial 2 a) Left b) Right

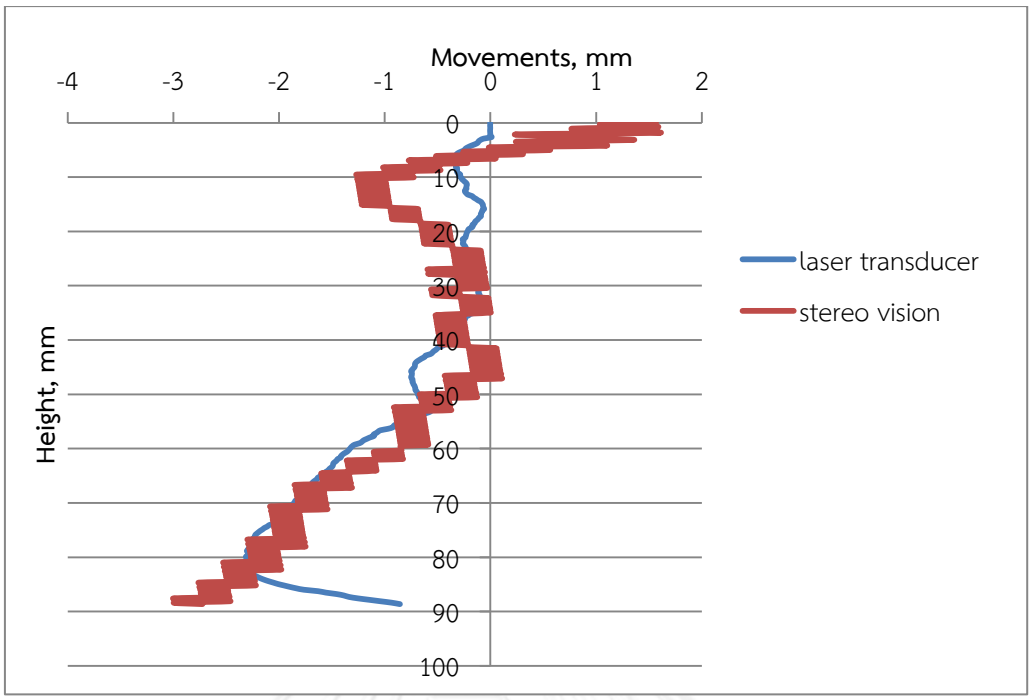

a)

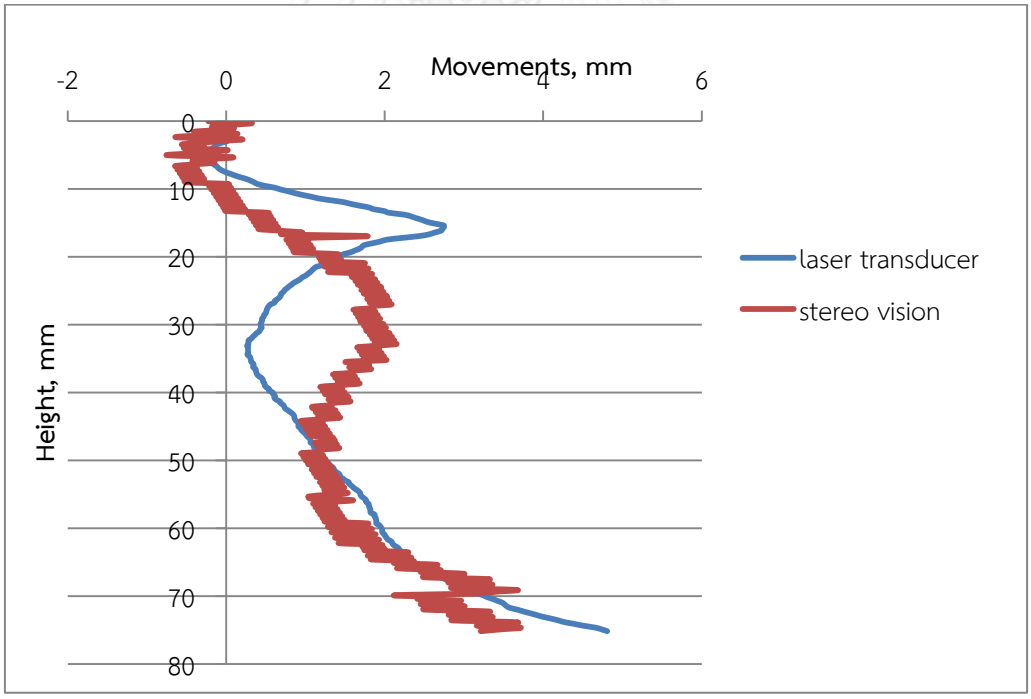

b)

Figure 5.2.69 Profile at boundary: Trial 3 a) Left b) Right

VITA

Erica Elice Saloma Uy was born on June 4, 1989 in Manila, Philippines. She attended De La Salle University where she took up Civil Engineering for her bachelor's degree. She is a licensed Civil Engineer in the Philippines since 2012.